NASA Contractor Report 4026

Implicit Time-Marching Solution of the Navier-Stokes Equations for Thrust Reversing and Thrust Vectoring Nozzle Flows

Scott T. Imlay

CONTRACT NAS1-17170
NOVEMBER 1986

NASA

NASA Contractor Report 4026

Implicit Time-Marching Solution of the Navier-Stokes Equations for Thrust Reversing and Thrust Vectoring Nozzle Flows

Scott T. Imlay
University of Washington
Seattle, Washington

Prepared for
Langley Research Center
under Contract NAS1-17170

National Aeronautics
and Space Administration

**Scientific and Technical
Information Branch**

1986

TABLE OF CONTENTS

		Page
List of Figures		v
List of Tables		x
Chapter 1.	Introduction	
I.	Two-Dimensional Thrust Reversing and Vectoring Nozzles	1
II.	Nature of Flow Field	2
III.	Related Research	4
IV.	Contributions of this Research	7
V.	Outline of this Research	9
Chapter 2.	Mathematical Model	
I.	Navier-Stokes Equation	14
II.	Modified Form for Moving Mesh	18
III.	Turbulence Model	19
Chapter 3.	Solution Procedure	
I.	Preliminary Comments	26
II.	Descretization of the Flow Field	27
III.	Approximation of the Time Derivative	30
IV.	Explicit Contribution	31
V.	Implicit Contribution	40
VI.	Smoothing Terms	54
VII.	Boundary Conditions	56
VIII.	System of Linear Algebraic Equations	71
IX.	Accuracy and Stability Analysis for Model Equation	78

Chapter 4. Results and Conclusions

I. Preliminary Comments 101

II. Fully Deployed Thrust Reversing Nozzle 102

III. Partially Deployed Thrust Reversing Nozzle 111

IV. Partially Deployed Thrust Reversing Nozzle with Vectoring 113

V. Transient Change in Thrust Vectoring Angle 115

VI. Transient Change in Thrust Reverser Deployment 116

VII. Conclusions 117

References 169

Appendix A. Diagonalization of the Jacobians for the Inviscid Fluxes 172

Appendix B. Block Pentadiagonal Solver 175

Appendix C. Ideal Mass Flow and Thrust 179

LIST OF FIGURES

		Page
Figure 1.1	Typical Thrust Reversing and Thrust Vectoring Nozzle Flow Field	13
Figure 2.1	Domains of Influence for Each Wall Turbulence Model	24
Figure 2.2	Domains of Influence for the Jet and Wall Turbulence Models in the Exterior Flow	25
Figure 3.1	Zonal Arrangement for Thrust Reversing and Thrust Vectoring Nozzle Program	85
Figure 3.2	A Region in the Interior Mesh	86
Figure 3.3	A Region in the Exterior Zone	87
Figure 3.4	Finite Volume Cell	88
Figure 3.5	Propagation of Information Along Locally One-Dimensional Time Dependent Characteristics	89
Figure 3.6	Characteristics Resulting from Steger and Warming Flux Splitting	90
Figure 3.7	Extrapolations to the i+1/2 Surface for First- and Second-Order Flux Splitting	91
Figure 3.8a	Arrangement of Linear System	92
Figure 3.8b	Definitions for Figure 3.8a	93
Figure 3.9	Approximate Factorization of Global Coefficient Matrix	94
Figure 3.10	Error Due to Approximate Factorization	95
Figure 3.11	Mesh for Fully Deployed Nozzle	96
Figure 3.12	Pressure Contours During Initial Transients	97
Figure 3.13	Velocity Vectors During Initial Transients	98

Figure 3.14	Normalized Time Difference of Density from Approximate Solutions of Linear System	99
Figure 3.15	Normalized Time Difference of Energy from Approximate Solutions of Linear System	100
Figure 4.1	Details of 2-D Convergent-Divergent Thrust-Reversing Nozzle	119
Figure 4.2	Mesh for Fully Deployed Thrust Reversing Nozzle	120
Figure 4.3	Mass Flow Convergence History for the Fully Deployed Thrust Reversing Nozzle	121
Figure 4.4	Mesh for Fully Deployed Thrust Reversing Nozzle	122
Figure 4.5	Evaluation of Grid Refinement Along Flap Y^+ Distribution for Cells Nearest Wall	123
Figure 4.6	Pressure Contours for Fully Deployed Thrust Reversing Nozzle	124
Figure 4.7	Pressure Contours for Fully Deployed Thrust Reversing Nozzle	125
Figure 4.8	Pressure Contours for Fully Deployed Thrust Reversing Nozzle	126
Figure 4.9	Mach Number Contours for Fully Deployed Thrust Reversing Nozzle	127
Figure 4.10	Mach Number Contours for Fully Deployed Thrust Reversing Nozzle	128
Figure 4.11	Mach Number Contours for Fully Deployed Thrust Reversing Nozzle	129
Figure 4.12a	Velocity Vectors for Fully Deployed Thrust Reversing Nozzle	130
Figure 4.12b	Details of Separation	131
Figure 4.13a	Velocity Vectors for Fully Deployed	

	Thrust Reversing Nozzle	132
Figure 4.13b	Details of Separation	133
Figure 4.14a	Velocity Vectors for Fully Deployed Thrust Reversing Nozzle	134
Figure 4.14b	Details of Separation	135
Figure 4.15	Variation of Discharge Coefficient with Nozzle Pressure Ratio for Fully Deployed Thrust Reversing Nozzle	136
Figure 4.16	Variation of Normalized Thrust with Nozzle Pressure Ratio for a Fully Deployed Thrust Reversing Nozzle	137
Figure 4.17	Sidewall Pressure Distribution at ZP = 0.203 cm - NPR = 3.0	138
Figure 4.18	Sidewall Pressure Distribution at ZP = 0.838 cm - NPR = 3.0	139
Figure 4.19	Sidewall Pressure Distribution at ZP = 1.473 cm - NPR = 3.0	140
Figure 4.20	Pressures Along Flap for NPR = 3.0	141
Figure 4.21	Mesh for 50% Deployed Thrust Reversing Nozzle	142
Figure 4.22	Pressure Contours for 50% Deployed Nozzle	143
Figure 4.23	Mach Number Contours for Symmetric 50% Deployed Nozzle	144
Figure 4.24	Velocity Vectors for Symmetric 50% Deployed Nozzle	145
Figure 4.25	Mesh for 50% Deployed Thrust Reversing Nozzle with 15 Degrees Downward Thrust Vectoring	146
Figure 4.26	Pressure Contours for 50% Deployed Nozzle	147
Figure 4.27	Mach Number Contours for 50% Deployed Thrust Reversing Nozzle with 15 Degrees	

	Vectoring	148
Figure 4.28	Velocity Vectors for 50% Deployed Thrust Reverser with 15 Degrees Vectoring	149
Figure 4.29	Mesh for Steady State Flow Field Calculation Prior to Thrust Vectoring Angle Change	150
Figure 4.30	Steady State Velocity Vectors Prior to Thrust Vectoring Angle Change	151
Figure 4.31	Steady State P/P_t Contours Prior to Thrust Vectoring Angle Change	152
Figure 4.32	Mesh for Transient Flow Field Calculation During Thrust Vectoring Angle Change	153
Figure 4.33	Transient Flow Field Velocity Vectors During Thrust Vectoring Angle Change	154
Figure 4.34	Transient Flow Field P/P_t Contours During Thrust Vectoring Angle Change	155
Figure 4.35	Mesh for Transient Flow Field Calculation After Thrust Vectoring Angle Change	156
Figure 4.36	Transient Flow Field Velocity Vectors After Thrust Vectoring Angle Change	157
Figure 4.37	Transient Flow Field P/P_t Contours After Thrust Vectoring Angle Change	158
Figure 4.38	Mesh for Steady State Flow Field Calculation Prior to Transition from Partial to Full Thrust Reverser Deployment	159
Figure 4.39	Steady State Flow Field Velocity Vectors Prior to Transition from Partial to Full Thrust Reverser Deployment	160

Figure 4.40	Steady State P/P_t Contours Prior to Transition from Partial to Full Thrust Reverser Deployment	161
Figure 4.41	Mesh for Transient Flow Field Calculation During Transition from Partial to Full Thrust Reverser Deployment	162
Figure 4.42a	Transient Flow Field Velocity Vectors During Transition from Partial to Full Thrust Reverser Deployment	163
Figure 4.42b	Detail of Transient Flow Field Velocity Vectors Near Entrance to Rear Port	164
Figure 4.43	Transient Flow Field P/P_t Contours During Transition from Partial to Full Thrust Reverser Deployment	165
Figure 4.44	Mesh for Transient Flow Field Calculation After Transition from Partial to Full Thrust Reverser Deployment	166
Figure 4.45	Transient Flow Field Velocity Vectors After Transition from Partial to Full Thrust Reverser Deployment	167
Figure 4.46	Transient Flow Field P/P_t Contours During Transition from Partial to Full Thrust Reverser Deployment	168
Figure B.1	Block Pentadiagonal System	177
Figure B.2	LU Decomposition of Block Pentadiagonal Matrix	178

LIST OF TABLES

Page

Table. 3.1 Cycle of Indicies 33

CHAPTER 1

INTRODUCTION

I. Two-Dimensional Thrust Reversing and Vectoring Nozzles

Two-dimensional nozzles have many advantages for fighter aircraft over conventional axisymmetric nozzles. Two-dimensional nozzles can be more easily faired to the airframe and their use, on twin engine aircraft, eliminates the high aft end drag from the "gutter" region between axisymmetric nozzles. In addition, two-dimensional nozzles can be adapted to thrust reversing and/or thrust vectoring with less weight penalty than conventional axisymmetric nozzles.

Thrust reversing and thrust vectoring capabilities are likely to be required of future fighter aircraft. The use of thrust reversal on landing reduces landing roll and the use of thrust vectoring for propulsive lift can reduce both takeoff and landing rolls. This short takeoff and landing capability is important for operation from bomb damaged runways.

Thrust vectoring and reversing may also be used during

flight to increase the aircraft's maneuverability. Thrust reversing can modulate the thrust with no spool-up delays, and thrust vectoring on aircraft with aft mounted nozzles is an effective alternative pitch control. This latter capability is important because experimental studies have shown considerable loss of elevator effectiveness on some configurations when in-flight thrust reversing is used.

The design of two-dimensional thrust reversing and thrust vectoring nozzles requires considerable understanding of nozzle internal flow fields. For example, if there were large variations in nozzle discharge coefficients during thrust reverser deployment it could adversly affect the engine performance by causing a mismatch between the choked turbine entry area and the effective area of the choked main nozzle. Currently, most thrust reversing nozzles are designed experimentally. This dissertation describes computational procedures developed for the analysis of thrust reversing and thrust vectoring nozzles.

II. Nature of Flow Field

There are many types of two-dimensional nozzles under investigation. The most common of these are convergent divergent (CD) nozzles, wedge nozzles, and single expansion ramp nozzles (SERN). This investigation deals with thrust reversing and thrust vectoring of two-dimensional convergent

divergent nozzles (2DCD).

A typical 2DCD nozzle with thrust reversing and thrust vectoring is depicted in Figure 1.1. The gas enters the nozzle subsonically and accelerates to transonic speeds as it enters one of the three exit ports. The gas then leaves the nozzle in a supersonic jet which interacts with the ambient flow. Furthermore, there is often a separation bubble located on the forward wall of the reverser ports near the sharp corners.

Within two-dimensional nozzles the flow is confined by the nozzle sidewalls. There are three-dimensional affects, due primarily to the boundary layers on the nozzle sidewalls, but these can generally be neglected when the nozzle is of high aspect ratio. Once the flow exits the nozzle, however, it is no longer confined in the lateral direction and the resulting expansion can significantly affect the flow within the jet. These three-dimensional effects are small near the nozzle exit but will become more significant as the distance from the exit increases.

The principal concern of this investigation is the flow within the nozzle. However, for many nozzle geometries the flow at the exit plane is subsonic and the nozzle internal flow is dependent on the external flow. In these cases the external flow field must be calculated. For all cases the flow is assumed to be two-dimensional. This is a good

assumption for the internal flow and external flow near the nozzle exit. This assumption, however, will cause inaccuracies in the external flow far from the nozzle. Since the results near the nozzle exit are fairly accurate the two-dimensional assumption is believed to be acceptable for modelling the effect of external flow on the internal flow.

Since the flow is transonic and contains boundary layer separation the effects of both compressibility and viscosity must be included in the mathematical model. For this reason the two-dimensional compressible Navier-Stokes equations are solved. These equations are given in Chapter 2, Section I.

III. Related Research

There have been many experimental studies of 2DCD nozzles with thrust reversing and thrust vectoring. Most are concerned with gross performance parameters such as discharge coefficient and thrust. Two examples are the work of Re and Leavitt (Reference 1) and Carson, Capone, and Mason (Reference 2). Re and Leavitt studied the static internal performance of fully deployed thrust reversing nozzles, as well as non-reversing nozzles. Carson, Capone, and Mason studied the aeropropulsive characteristics of partially and fully deployed thrust reversing nozzles

including one partially deployed nozzle with thrust vectoring.

More information concerning the flow field within a thrust reversing nozzle is obtained from the measurements of Putnam and Strong (Reference 3). They measured static pressures along the sidewall, the blocker, and the flap (including the forward wall of the reverser port) of a fully deployed thrust reversing nozzle. The measurements were made with an external ambient Mach number of zero for a range of nozzle pressure ratios, from two to eight.

Several computer programs have been written to solve the Navier-Stokes equations for flow within conventional nozzle configurations. Cline (Reference 4) developed a computer program, VNAP, which solved the two-dimensional or axisymmetric Navier-Stokes equations using the 1969 MacCormack explicit finite difference method. This program divides the mesh into two zones so that the mixing of two streams can be calculated. Unfortunately, one set of mesh lines must always remain vertical, thus limiting the amount of geometric turning which may be calculated. VNAP is not applicable to thrust reversing nozzles since such nozzles invariably have large turning angles.

Peery and Forester (Reference 16) developed a finite volume computer program which also used the 1969 MacCormack explicit method. This program utilizes three zones and a

generalized nonorthogonal mesh to calculate the mixing of three streams. While this code could, in principle, be applied to thrust reverser flow fields, no attempt has been made to do so.

Both of the above computer programs solve the Navier-Stokes equations using an explicit time marching method. Explicit methods are limited by stability to very small time steps which are proportional to the smallest mesh spacing used. For viscous flow problems the mesh must be refined near the wall to resolve the boundary layer profile. As a result, explicit methods become very inefficient for viscous problems because tens of thousands of time steps are required to obtain steady state solutions. Recently, implicit methods have been developed which overcome this time step limitation.

Goldberg, Gorski, and Chakravarthy (Reference 5) have developed a computer program for axisymmetric afterbody flows. This program utilizes a new implicit method which is similar to the method presented in this dissertation. The program uses an implicit upwind method, with line Gauss Seidel relaxation, to solve the Navier-Stokes equations on a single zone mesh. Since this program does not have multiple zone capability it would have limited application to thrust reversing nozzles.

No previous investigators have attempted to solve the

Navier-Stokes equations for flow with a thrust reversing nozzle.

IV. Contributions of this Research

A typical thrust reverser flow is very demanding of a numerical method. Thrust reverser flows, by nature, involve very large turning angles (greater than 90 degrees) and rapid expansions. Also, since the thrust reverser is a secondary configuration, thrust reversers often contain sharp corners where two sections of the baseline forward thrust nozzle wall join. Near these sharp corners the rapid expansion (with pressure ratios up to five) and large turning angles lead to numerical difficulties comparable to (or worse than) those encountered while capturing strong shock waves. The contributions of this research are identifying and overcoming these difficulties.

For reasons given in the previous section, it was decided at the start of this investigation that an implicit method was required if the resulting program was to be efficient. In theory implicit methods have no time step restrictions. However, implicit methods require the approximate solution of a very large system of linear algebraic equations. Conventional implicit methods approximately factor the coefficient matrix for this system into the product of two or more simpler matrices whose

systems may be efficiently solved using direct methods. This approximate factorization leads to an error which is small for most flows but significant for thrust reverser flows. Our attempts to use various approximate factorizations all led to unacceptable time step restrictions. The first contribution of this research is identifying the approximate factorization as the cause of this time step restriction. This problem was overcome by solving the system iteratively using line Gauss-Seidel relaxation.

The next contribution concerns adapting the solution procedure to the complex solution domain found in thrust reversing nozzles. Efficient implementation of the line Gauss-Seidel relaxation requires computationally simple meshes (meshes that may be mapped into a rectangular domain). Unfortunately, a single simple mesh cannot easily be generated for thrust reverser flow fields like that in Figure 1.1. The solution is to break the flow field into as many as four zones, each of which is descretized by a simple mesh. With a zonal approach such as this, care must be taken to insure that the solution procedure is consistent across zonal boundaries. This author believes that this is the first time a zonal procedure has been utilized with a Gauss-Seidel implicit method.

V. Outline of this Research

The goal of this research effort was to develop a computer program to calculate the viscous compressible flow through a two-dimensional convergent-divergent thrust reversing and thrust vectoring nozzle like that shown in Figure 1.1. This requires the solution of the compressible Navier-Stokes equations which are presented in integral form in Chapter 2, Section I. These equations are modified for time varying meshes in Section II so that the transient flows due to the nozzle reconfiguration may be studied. Section III presents the algebraic eddy viscosity model used to model turbulent flows.

The solution of the Navier-Stokes equations requires considerable computer time and an inefficient solution procedure may result in such long run times that its use is impractical. For this reason an implicit method was chosen over explicit methods. Chapter 3 presents the solution procedure used.

Implicit methods generally require that the mesh be such that it can be mapped into a rectangular domain. Unfortunately, it is very difficult to generate one such mesh for the entire flow field in a thrust reversing nozzle (Figure 1.1). The alternative is to divide the flow field into zones for which simple meshes can be generated. The solution procedure is applied to each mesh individually and

the zonal solutions are coupled at the zonal interfaces. The overall mesh topology and the mesh generation procedure for each zone are described in Section II of Chapter 3.

Section III through V of Chapter 3 present the implicit finite volume method used in the interior of the flow field. Sections VI and VII discuss the treatment of the boundary conditions. Section VIII of Chapter 3 discusses the solution of the large system of linear algebraic equations resulting from the implicit finite volume method. This is one area where this work differs significantly from most previous research. Most previous investigations used approximate factorization to solve this large system of algebraic equations. In Section VIII of Chapter 3, it is shown that the standard approximate factorization method performs poorly for the thrust reversing nozzle flows. As a result, the linear system of equations is solved using a line Gauss-Seidel relaxation method which is shown to perform dramatically better than the standard approximate factorization.

In Section IX of Chapter 3, the accuracy and stability of the method is analyzed for the model equation. When explicit, it is shown to be second-order accurate. When fully implicit it is shown to be first-order accurate in time, second-order accurate in space, and unconditionally stable.

In Chapter 4 , the results are presented for five nozzle test cases. In Section I the results for a fully deployed nozzle are presented and compared with the experimental results of Re and Leavitt (Reference 1) and Putnam and Strong (Reference 3). The calculated discharge coefficient compares very well with the experimental results with the largest error being four percent. The calculated pressure field also compares well with the experimental results, except near the forward wall of the reverser port where the pressure is overestimated. This discrepancy causes the amount of reverse thrust to be underestimated by nearly 15 percent of the ideal thrust when the calculation is second order accurate. Numerical dissipation, the turbulence model, and three dimensional effects are all believed to contribute to this discrepancy.

In Sections II and III of Chapter 4, results are presented for a 50 percent deployed nozzle with both 0° and 15° of vectoring. Results are compared with the experimental data of Carson, Capone and Mason (Reference 2). In both cases a coarse mesh was used and the resulting numerical dissipation led to an underestimation of the discharge coefficient. Both calculations were initially first-order accurate which resulted in errors of 21 percent in the discharge coefficient. The unvectored case was then run second-order accurate and the error was reduced to seven

percent. In both cases, the normalized thrust compares surprisingly well with experimental data.

Section IV presents the results for a transient change in thrust vectoring angle and Section V the results for a transient change in thrust reverser deployment. No experimental data is available for these cases, but the results look qualitatively correct.

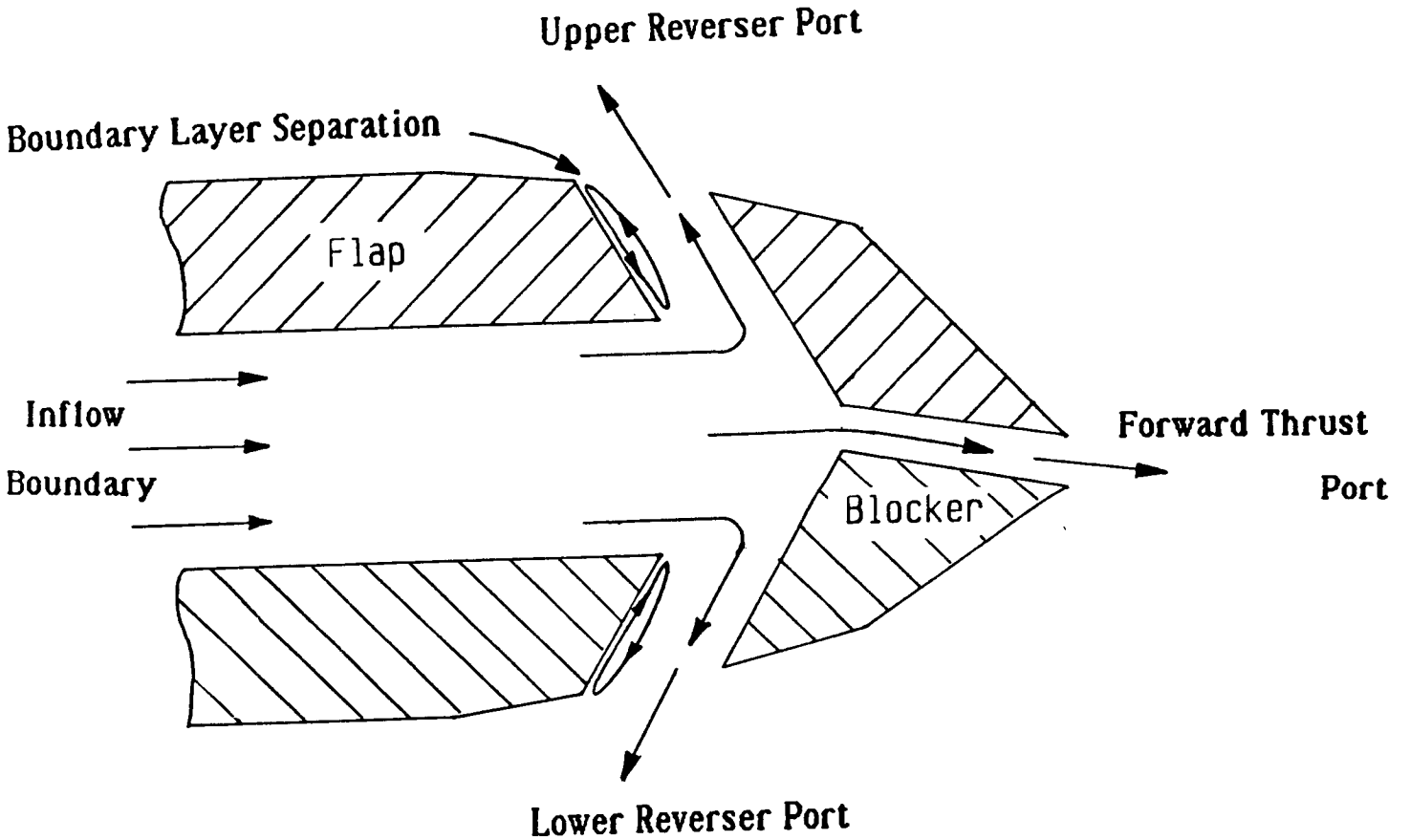

Figure 1.1 Typical Thrust Reversing and Thrust Vectoring Nozzle Flowfield.

CHAPTER 2

Mathematical Model

I. Navier-Stokes Equation

The two-dimensional Navier-Stokes equations are a set of four coupled nonlinear partial differential equations that model the flow of viscous, compressible heat-conducting fluids. These equations are derived by application of the principles of conservation of mass, momentum, and energy. The equations can be written in integral form,

$$\frac{\partial}{\partial t} \int_V U \, dV + \int_S \bar{P} \cdot \bar{n} \, dS = \emptyset, \tag{2.1}$$

where V is an arbitrary volume, S is the surface surrounding V, and $\bar{n}$ is the unit vector outward normal to S. Also

$$\bar{P} = F \, \bar{i}x + G \, \bar{i}y \tag{2.2}$$

where

$$U = \begin{bmatrix} \rho \\ \rho u \\ \rho v \\ E \end{bmatrix} \tag{2.3 a}$$

$$F = \begin{bmatrix} \rho u \\ \rho u^2 + P + \tau_{xx} \\ \rho uv + \tau_{xy} \\ (E + P + \tau_{xx})u + \tau_{xy}v + q_x \end{bmatrix}, \text{ and} \qquad (2.3\ b)$$

$$G = \begin{bmatrix} \rho v \\ \rho vu + \tau_{yx} \\ \rho v^2 + P + \tau_{yy} \\ \tau_{yx}u + (E + P + \tau_{yy})v + q_y \end{bmatrix} \qquad (2.3\ c)$$

The variables ρ, u, v, P, and E are defined below.

ρ - density

u - component of velocity in x-coordinate direction

v - component of velocity in y-coordinate direction

P - pressure

E - volume specific total energy

The volume specific total energy, E, is related to the mass specific internal energy e, the density ρ, and the velocity by the following equation.

$$E = \rho[e + \emptyset.5(u^2 + v^2)] \qquad (2.4)$$

The pressure is related to the density and specific internal energy by the equations of state,

$$P = P(\rho, e), \qquad (2.5)$$

which is taken to be the ideal gas law.

$$P = \rho(\gamma - 1)e \qquad (2.6)$$

The gas is also assumed to be calorically perfect so that specific internal energy is proportional to the temperature,

T, with the constant of proportionality being the specific heat at constant volume.

$$e = c_v T \tag{2.7}$$

The specific heat at constant volume, c_v, is assumed to be a constant equal to 4290.0 $ft^2/s^2{}^oR$, and the ratio of specific heats, γ, is assumed to be a constant equal to 1.4.

To facilitate the development of the solution procedure, the contributions to the fluxes from the inviscid terms , F_I, and the diffusion terms, F_D, are considered separately.

$$F = F_I + F_D$$

$$G = G_I + G_D$$

where

$$F_I = \begin{bmatrix} \rho u \\ \rho u^2 + P \\ \rho uv \\ (E+P)u \end{bmatrix} \qquad (2.8\ a)$$

$$G_I = \begin{bmatrix} \rho v \\ \rho vu \\ \rho v^2 + P \\ (E+P)v \end{bmatrix} \qquad (2.8\ b)$$

$$F_D = \begin{bmatrix} 0 \\ \tau_{xx} \\ \tau_{xy} \\ \tau_{xx}u + \tau_{xy}v + q_x \end{bmatrix} \qquad (2.9\ a)$$

$$G_D = \begin{bmatrix} 0 \\ \tau_{yx} \\ \tau_{yy} \\ \tau_{yx}u + \tau_{yy}V + q_y \end{bmatrix} \qquad (2.9\ b)$$

The variables τ_{xx}, τ_{xy}, τ_{yx}, and τ_{yy} are viscous stress

terms which are defined in terms of the derivatives of the velocity components.

$$\tau_{xx} = -2\mu\frac{\partial u}{\partial x} - \lambda\nabla\cdot\bar{V} \qquad (2.10\ a)$$

$$\tau_{yy} = -2\mu\frac{\partial v}{\partial y} - \lambda\nabla\cdot\bar{V} \qquad (2.10\ b)$$

$$\tau_{xy} = \tau_{yx} = -\mu\left(\frac{\partial u}{\partial y} + \frac{\partial v}{\partial x}\right) \qquad (2.10\ c)$$

$$\nabla\cdot\bar{V} = \frac{\partial u}{\partial x} + \frac{\partial v}{\partial y} \qquad (2.10\ d)$$

The variables q_x and q_y are heat flux terms which are given in terms of derivatives of temperature.

$$q_x = -k\frac{\partial T}{\partial x} \qquad (2.11\ a)$$

$$q_y = -k\frac{\partial T}{\partial y} \qquad (2.11\ b)$$

The viscosity coefficients, λ and μ, are related through the bulk viscosity, κ.

$$\kappa = \frac{2}{3}\mu + \lambda \qquad (2.12)$$

The bulk viscosity is negligible except in the study of the structure of shock waves so

$$\lambda = -\frac{2}{3}\mu \qquad (2.13)$$

The coefficient of viscosity, μ, is related to the temperature by Sutherland's empirical formula for air,

$$\frac{\mu}{\mu_\bullet} = \left(\frac{T}{T_\bullet}\right)^{3/2}\left(\frac{T_\bullet + 198.6}{T + 198.6}\right), \qquad (2.14)$$

where the temperature is expressed in degrees Rankine and μ_o is the reference viscosity at the reference temperature, T_o. The coefficient of thermal conductivity, k, is obtained from the expression for the Prandtl number,

$$Pr = \frac{Cp\,\mu}{k} \qquad (2.15)$$

where Pr is assumed to be a constant equal to 0.72 for

laminar flow.

II. Modified Form for Moving Mesh

For problems with moving meshes it is convenient to use a modified form of these equations. By the Reynolds Transport Theorem the first term in equation 2.1 is expanded as follows.

$$\frac{\partial}{\partial t}\int_V U\, dV = \int_V \frac{\partial u}{\partial t} dV + \int_S U\, \bar{V}_{surface} \cdot \bar{n} ds \tag{2.16}$$

Substituting this into the integral form of the Navier-Stokes equations (equation 2.1) gives

$$\int_V \frac{\partial U}{\partial t}\, dV + \int_S (\bar{P} + U\, \bar{V}_{surface}) \cdot \bar{n}\, ds = \emptyset \tag{2.17}$$

where $\bar{V}_{surface}$ is the velocity of the surface in the direction of the unit outer normal, $\bar{n}$. Defining a moving mesh flux function,

$$\bar{P}_M = \bar{P} + U\, \bar{V}_{surface} \tag{2.18}$$

gives

$$\int_V \frac{\partial U}{\partial t}\, dV + \int_S \bar{P}_M \cdot \bar{n}\, ds = \emptyset \tag{2.19}$$

III. Turbulence Model

For turbulent flow calculations the mass-weighted Reynold's averaged Navier-Stokes equations are used (Reference 6). These are the standard equations obtained by writing the variables in the Navier-Stokes as the sum of a time averaged quantity and a fluctuating quantity. The resulting equations are then averaged and the Boussinesq approximation is applied to the resulting Reynolds stresses. The result is a set of equations identical in form to the equations in section I except that the viscosity and heat conduction coefficients become the sum of their laminar values with new turbulent coefficients.

$$\mu = \mu_l + \mu_t$$

$$k = k_l + k_t$$

Here μ_t is called the eddy viscosity and k_t is called the turbulent conductivity.

For wall boundary layers, the eddy viscosity is obtained from an algebraic two-layer eddy viscosity model developed by Baldwin and Lomax (Reference 7). In the model, the eddy viscosity, μ_t, is given by

$$\mu_t = \begin{cases} (\mu_t)\ \text{inner} & y' \leq y'_{\text{crossover}} \\ (\mu_t)\ \text{outer} & y' > y'_{\text{crossover}} \end{cases} \qquad (2.20)$$

where y' is the normal distance from the wall and

$y'_{crossover}$ is the smallest value of y' for which $(\mu_t)_{inner} = (\mu_t)_{outer}$.

For the inner layer the Prandtl-Van Driest formulation is used.

$$(\mu_t)_{inner} = \rho l^2 |\omega| \tag{2.21}$$

In this equation ρ is the density, l is a length scale, and ω is the vorticity.

$$\omega = \frac{\partial u}{\partial y} - \frac{\partial v}{\partial x} \tag{2.22}$$

The length scale is give by

$$l = k\, y' [1 - \exp(-y^+/A^+)] \tag{2.23}$$

where y^+ is given in terms of density, shear stress, and viscosity at the wall.

$$y^+ = \frac{\sqrt{\rho_w \tau_w}\; y'}{\mu_w} \tag{2.24}$$

In the outer region the eddy viscosity is calculated with the following formula.

$$(\mu_t)_{outer} = K\, C_{CP}\, \rho\, F_{WAKE}\, F_{KLEB}(y') \tag{2.25}$$

Here K is the Clauser constant and F_{WAKE} is obtained from

$$F_{WAKE} = \text{MIN}\{y_{MAX}\, F_{MAX},\ C_{WK}\, y_{MAX}\, U^2_{DIFF}/F_{MAX}\}. \tag{2.26}$$

The terms Y_{MAX} and F_{MAX} are obtained from

$$F(y') = y'\, |\omega|\, [1 - \exp(-y^+/A^+)]\ . \tag{2.27}$$

where F_{MAX} is the maximum value of F(y') in the boundary layer profile and y_{MAX} is the value of y' at which F_{MAX} occurs. The term U^2_{DIFF} is simply the square of the maximum total velocity, U^2_{MAX}, for boundary layer flows. Finally, the function $F_{KLEB}(y')$ is the Klebanoff intermittency

factor.

$$F_{KLEB}(y') = [1 + 5.5 \left(\frac{C_{KLEB}\, y'}{y_{MAX}} \right)^6]^{-1} \qquad (2.28)$$

The constants used in the above formulas are those recommended by Baldwin and Lomax (Reference 7).

$A^+ = 26$

$C_{CP} = 1.6$

$C_{KLEB} = 0.3$

$k = 0.4$

$K = 0.0168$

The above turbulence model is implemented for each of the interior walls of the nozzle as well as the exterior nozzle surfaces. For application to an interior wall the testing for U_{MAX} and F_{MAX} occurs along a column of cells as shown in Figure 2.1. This testing occurs from the wall to the point half way to the opposite wall (half way in terms of number of cells). The spacial derivatives of u and v in the expression for the vorticity are calculated using a numerical transformation described completely in the discussion of the diffusion terms in Chapter 3, Section IV.

The Baldwin Lomax model is also used for the jets emanating from each nozzle exit port. For the jets the outer formulation is used with

$$F_{WAKE} = C_{WK} U^2_{MAX} / |\omega|_{MAX} \qquad (2.29\ a)$$

and

$$F_{KLEB} = 1 \ . \qquad (2.29\ b)$$

Equations 2.29 are utilized with equation 2.25 to obtain the eddy viscosities for the jet at each station downstream of the nozzle exit.

In the external flow the results from the jet turbulence model must somehow be blended with the results from the wall turbulence model. This is done by giving each model a domain which it influences as shown in Figure 2.2. At the nozzle exit the jet model is used for only those cells adjacent to interior cells. For the rest of the cells in this column the eddy viscosities are obtained from the wall turbulence model. At each successive column of cells outward from the nozzle the domain for the jet model widens by two cells (one on either side of the jet). After six columns the spreading of the jet model increases by four cells per column. The wall turbulence model dominates near the nozzle (except at the nozzle exits) and the jet model dominates far from the nozzle.

Once the eddy viscosity is known turbulent conductivity is obtained from

$$k_t = \mu_t \, C_p / Pr_t \qquad (2.30)$$

where Pr_t is the turbulent Prandtl number. As recommended by Baldwin and Lomax (Reference 7) the turbulent Prandtl number is taken as Ø.9.

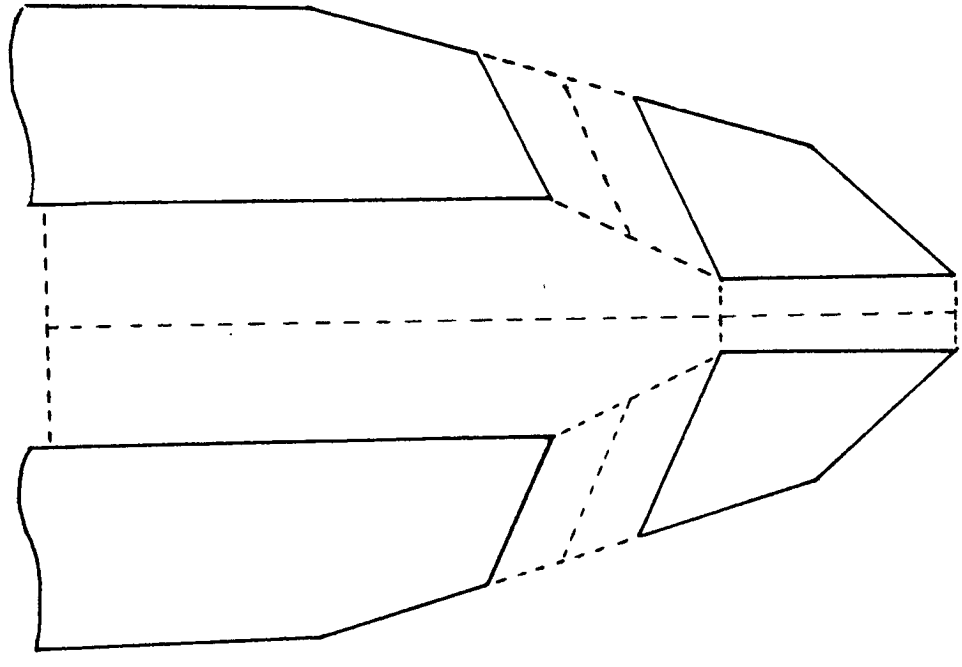

Figure 2.1 Domains of Influence for Each Wall Turbulence Model.

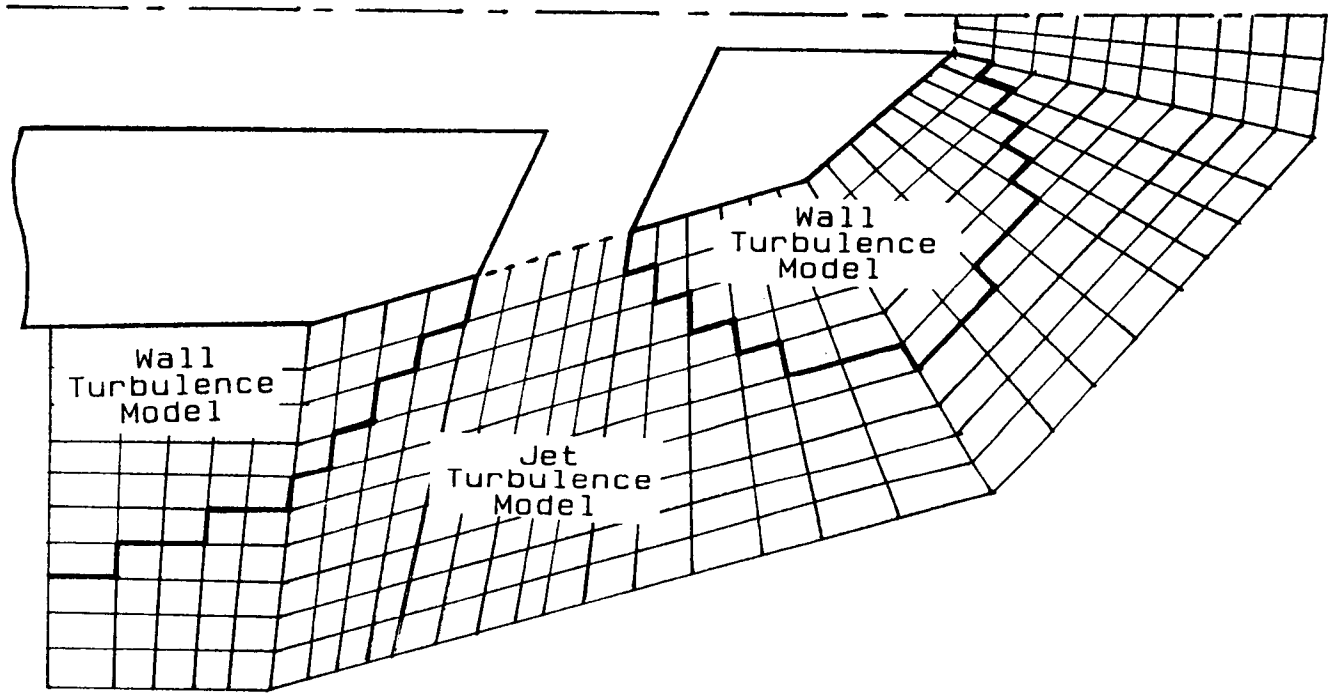

Figure 2.2 Domains of Influence for the Jet and Wall Turbulence Models in the Exterior Flow.

CHAPTER 3

SOLUTION PROCEDURE

I. Preliminary Comments

This chapter describes the numerical procedure developed for solving the Navier-Stokes equations for thrust reversing and thrust vectoring nozzle flows. Thrust reversing nozzle flows provide difficulties not encountered with more conventional nozzles. Typically thrust reversing nozzles have sharp corners resulting from the separating of the smoothly faired walls present in the cruise configuration. Near sharp corners the mesh must be refined in two nearly perpendicular directions. This leads to unacceptable time step restrictions for conventional implicit finite difference methods. The numerical procedures presented in this chapter were developed to overcome these difficulties.

Section II describes the mesh topology and mesh generation procedure. The mesh is broken into as many as four zones to facilitate the application of boundary conditions and make efficient use of computer memory.

Section III evaluates the time derivative using a predictor-corrector method and presents the basic finite volume equations. These equations require the evaluation of the fluxes through each of the four faces surrounding an arbitrary quadrilateral finite volume. Sections IV through VI consider the approximate evaluation of these fluxes.

Section VII presents the application of the boundary conditions. Section VIII discusses the solution of the large system of linear algebraic equations that result from the implicit difference method. It is shown that the popular approximate factorization method yields unacceptable results for thrust reverser flows and a line relaxation procedure is adopted. Finally, Section IX provides an accuracy and stability analysis for the solution procedure applied to a linear scaler wave equation.

II. Discretization of the Flow Field

The flow field under consideration is discretized into a large number of finite volume cells. In two dimensions these finite volumes are arbitrary quadrilaterals which are described completely by the x,y-coordinates of their four corner points. Within the computer program, the mean value of the conservative variables, U, within a cell and the corner point coordinates are stored in terms of indices i and j. Cell i,j, containing $U_{i,j}$, is defined by the x,y-

coordinates with indices i,j, i+1,j, i,j+1, and i+1,j+1.

On a larger scale, the mesh for the thrust reversing and thrust vectoring nozzle program is divided into as many as four zones--one zone for each of three possible internal flow ports and a zone for the exterior flow as shown in Figure 3.1. The mesh is generated such that mesh lines are continuous across the zonal interfaces. A single set of i and j indices are used to specify cell locations within all the internal zones as shown in Figure 3.1 b stacked on top of one another. Each must have the same number of columns, given by the i index. The mesh cell locations in the external flow zone are specified by a separate set of indices, ie and je. The outer zone mesh lines must be continuous with the internal zone, but the external zone is not required to have the same number of columns as the internal zones.

The mesh for each interior zone is generated from cell coordinate data input along the lower and upper boundaries of the zone and, optionally, also along an arbitrary dividing line extending from the inflow boundary to the outflow boundary. If the zone has a dividing line, the line divides the zone into two regions for mesh generation purposes. Otherwise the zone is a single region. An example region is shown in Figure 3.2. The mesh is generated for this region using a simple algebraic process:

1) all corner points for a given i-index within a region lie along a line segment connecting the points input for that i-index on the upper and lower boundaries, and

2) the position of an i,j corner point along the line segment is given by the relation

$$\frac{l}{L} = \frac{l_I}{L_I} \tag{3.1}$$

where l, L, l_I, and L_I are defined in Figure 3.2.

The mesh for the external zone is generated somewhat differently. The external zone can also be broken into two regions as with an internal zone. However, the dividing line for the exterior mesh becomes an ie=constant mesh line, whereas the dividing line for the interior zone becomes a j=constant mesh line. Also, for the interior zones, corner point coordinates are given along only three of the boundaries of a region where, for the exterior zone, corner point coordinates are given for all four boundaries of a region. In this case the mesh is generated for each region using a modified algebraic process:

1) all corner points for a given je index within a region lie along a line segment connecting the points input for that je index along the inner and outer boundaries of the region, and

2) the position of an ie,je corner point along the line segment is given by the relation

$$\frac{l}{L} = (1 - \frac{a}{A}) \frac{l_L}{L_L} + (\frac{a}{A}) \frac{l_u}{L_u} \qquad (3.2)$$

where a is the arclength along the inner boundary of the region to point je, A is the total arclength of the inner boundary of the region, and l, L, l_L, L_L, l_u, and L_u are all defined in Figure 3.3.

III. Approximation of the Time Derivative

The Navier-Stokes equations, when applied to a finite volume cell, become

$$(\frac{dU_{i,j}}{dt}) \text{ Vol}_{i,j} + D_i (\bar{P}\cdot\bar{S}) + D_j (\bar{P}\cdot\bar{S}) = \emptyset \qquad (3.3)$$

where

$$D_i (\bar{P}\cdot\bar{S}) = \bar{P}\cdot\bar{S}_{i+1/2,j} - \bar{P}\cdot\bar{S}_{i-1/2,j} \qquad (3.4\ a)$$

$$D_j (\bar{P}\cdot\bar{S}) = \bar{P}\cdot\bar{S}_{i,j+1/2} - \bar{P}\cdot\bar{S}_{i,j-1/2} \qquad (3.4\ b)$$

and the surface vectors are always oriented in the positive i or j directions as shown in Figure 3.4. If the mesh is moving the equation is the same except that $\bar{P}$ is replaced by $\bar{P}_M$ as defined in Chapter 2, Section II.

The time derivative is approximated with MacCormack's predictor-corrector method (Reference 8).

Predictor

$$\overline{U^{n+1}_{i,j}} = U^n_{i,j} - (\frac{\Delta t}{\text{Vol}_{i,j}}) [D_i (\bar{P}\cdot\bar{S})^p + D_j (\bar{P}\cdot\bar{S})^p] \qquad (3.5\ a)$$

Corrector

$$U^{n+1}_{i,j} = \emptyset.5 \left\{ U^{n}_{i,j} + \overline{U^{n+1}_{i,j}} - \left(\frac{\Delta t}{Vol_{i,j}}\right) \left[D_i \left(\bar{P}\cdot\bar{S}\right)^{c} + D_j \left(\bar{P}\cdot\bar{S}\right)^{c} \right] \right\} \qquad (3.5\ b)$$

Note the superscripts p and c on the flux terms. These indicate that the fluxes may be evaluated differently on the predictor and corrector steps. In fact, the way in which the fluxes are evaluated in terms of the $U_{i,j}$ determines the type of method that is used.

IV. Explicit Contribution

Equations 3.5 do not specify how the fluxes are to be evaluated. If the values of the conservative variables were known at the surface of each cell (e.g. at i+1/2), the flux could be obtained simply from equations (2.2) and (2.3). Unfortunately, only the mean value of the solution within each cell is known. The flux through a surface must therefore be approximated from the mean values of the solution within neighboring cells. In general the flux is evaluated using both the solution at the current time level, nc, and the solution being sought at the new time level, nn. This section considers the explicit contribution - the contribution from the current time level.

The inviscid terms and diffusion terms contribute substantially different characteristics to the Navier-Stokes

equations. In the limit as the Reynolds number goes to infinity the inviscid terms dominate and the equations are hyperbolic in time. In this case information concerning a disturbance in the flow field is propagated at a finite rate in a manner described by the theory of characteristics. It is therefore appropriate to incorporate the theory of characteristics into the approximation of the inviscid flux through a surface. In the limit as the Reynolds number goes to zero the diffusion terms dominate and the equations are parabolic in time. The approximation of the surface flux due to the diffusion terms should reflect the parabolic nature of these terms. This section will consider the treatment of the inviscid terms first followed by the treatment of the diffusion terms.

Inviscid Surface Fluxes

The inviscid flux is evaluated using a second-order flux vector splitting which is based, ultimately, on the 1969 MacCormack method. Three approximations to the surface flux are presented here; the 1969 MacCormack method, its extension to first-order flux vector splitting, and its extension to second-order flux vector splitting.

1969 MacCormack Method

In the 1969 MacCormack explicit method (Reference 9) the fluxes are evaluated at the latest known time level using, alternately, the value of $\bar{P}$ on either side of the

surface. For the i+1/2 and j+1/2 surfaces (Figure 3.4)

$$(\bar{P}\cdot\bar{S})_{i+1/2} = \bar{P}^{nc}_{ii,j}\cdot\bar{S}_{i+1/2} \qquad (3.6\ a)$$

$$(\bar{P}\cdot\bar{S})_{j+1/2} = \bar{P}^{nc}_{i,jj}\cdot\bar{S}_{j+1/2} \qquad (3.6\ b)$$

where nc is the current time level, ii is an index which is either i or i+1, and jj is an index which is either j or j+1. These indices run through a cycle every four steps as shown in table 3.1.

For a subsonic flow, where information can travel in either direction, the 1969 MacCormack method violates the physical domain of dependence on the predictor and corrector steps individually, but satisfies the physical domain of dependence collectively.

n		ii	jj	np	nn
1	Predictor	i+1	j+1	n	n+1
	Corrector	i	j	n+1	n+1
2	Predictor	i	j+1	n	n+1
	Corrector	i+1	j	n+1	n+1
3	Predictor	i+1	j	n	n+1
	Corrector	i	j+1	n+1	n+1
4	Predictor	i	j	n	n+1
	Corrector	i+1	j+1	n+1	n+1

Table 3.1 Cycle of Indicies

First-Order Flux Vector Splitting

In general the surface flux should be some nonlinear function of the solution on either side of the surface. To determine an appropriate approximate function it is instructive to look at the eigensystem of the Jacobian matrix. First of all, the flux vector is homogeneous of degree one in the elements of U.

$$(\bar{P}\cdot\bar{S}) = \left[\frac{\partial(\bar{P}\cdot\bar{S})}{\partial U}\right] = AU \tag{3.7}$$

The Jacobian can be diagonalized by a similarity transformation

$$A = T^{-1}R^{-1}S^{-1}\Lambda\ S\ R\ T\ |\bar{S}| \tag{3.8}$$

where S,R, and T are matrices given in appendix A, Λ is a diagonal matrix containing the eigenvalues of the Jacobian matrix

$$\Lambda = \begin{bmatrix} u' & & & \emptyset \\ & u' & & \\ & & u'+c & \\ \emptyset & & & u'-c \end{bmatrix} \tag{3.9}$$

and u' is the component of velocity in the $\bar{S}$ direction.

The eigenvalues of the Jacobian matrix are the speed at which information is propogated in the $\bar{S}$ direction and a negative sign indicates propagation of information in the direction opposite to $\bar{S}$. Figure 3.5 illustrates the propagation of information in the $\bar{S}$ direction for both

subsonic and supersonic flows. The arrows are the local time-dependent characteristics whose slope are given by the eigenvalues of A. Following Steger and Warming (Reference 10) the Jacobian matrix is taken as the sum of two matrices, one containing the positive eigenvalues and the other the negative eigenvalues.

$$A^+ = T^{-1} R^{-1} S^{-1} \Lambda^+ S R T \qquad (3.10\ a)$$

$$A^- = T^{-1} R^{-1} S^{-1} \Lambda^- S R T \qquad (3.10\ b)$$

$$\Lambda^+ = \text{diag}\ (\lambda_1^+, \lambda_1^+, \lambda_3^+, \lambda_4^+) \qquad (3.11\ a)$$

$$\Lambda^- = \text{diag}\ (\lambda_1^-, \lambda_1^-, \lambda_3^-, \lambda_4^-) \qquad (3.11\ b)$$

$$\lambda_k^+ = \frac{\lambda_k + |\lambda_k|}{2}\ ,\ \lambda_k^- = \frac{\lambda_k - |\lambda_k|}{2} \qquad (3.11\ c,d)$$

The flux is then evaluated approximately by multiplying the matrix of positive eigenvalues, A^+, by the solution to the left of the face, and the matrix of negative eigenvalues, A^-, by the solution to the right of the face.

$$(\bar{P}\cdot\bar{S})_{i+1/2} = A^+ U^{nc}_{i,j} + A^- U^{nc}_{i+1,j} \qquad (3.12)$$

The Jacobians, A^+ and A^-, are calculated using $U^{nc}_{ii,j}$ where nc and ii go through the cycle in table 3.1.

$$(\bar{P}\cdot\bar{S})^{FS}_{i+1/2} = (A^+)^{nc}_{ii,j}\ U^{n}_{i,j} + (A^-)^{nc}_{ii,j}\ U^{nc}_{i+1,j} \qquad (3.13\ a)$$

$$(\bar{P}\cdot\bar{S})^{FS}_{j+1/2} = (A^+)^{nc}_{i,jj}\ U^{nc}_{i,j} + (A^-)^{nc}_{i,jj}\ U^{nc}_{i,j+1} \qquad (3.13\ b)$$

Note that both the positive and negative Jacobians are calculated alternately using the values of the solution on either side of the surface (i and i+1 for the i+1/2 surface, or j and j+1 for the j+1/2 surface). This is in contrast to the flux vector splitting of Steger and Warming, (Reference 10), where $A^{+}_{i+1/2}$ is evaluated using $U_{i,j}$ and $A^{-}_{i+1/2}$ is evaluated using $U_{i+1,j}$. As shown in Figure 3.6, the Steger and Warming splitting results in five characteristics converging on a shock wave and only three characteristics converging on a sonic point. Thus the flux at a shock wave is overspecified and the flux at a sonic point is underspecified. Calculating both Jacobians using the same value of U eliminates this problem.

An additional advantage of this approach is that it allows a convenient extension of the 1969 MacCormack scheme to flux splitting. The 1969 MacCormack fluxes through the i+1/2 face, equations 3.6, may be rewritten as follows.

$$\text{ii=i: } (\bar{P}\cdot\bar{S})^{1969}_{i+1/2} = \bar{P}^{nc}_{i,j}\cdot\bar{S}_{i+1/2} = [(A^{+})^{nc}_{i,j}+(A^{-})^{nc}_{i,j}]U^{nc}_{i,j} \tag{3.14 a}$$

$$\text{ii=i+1: } (\bar{P}\cdot\bar{S})^{1969}_{i+1/2} = \bar{P}^{nc}_{i+1,j}\cdot\bar{S}_{i+1/2} = [(A^{+})^{nc}_{i+1,j} + (A^{-})^{nc}_{i+1,j}]U^{nc}_{i+1,j} \tag{3.14 b}$$

Comparing these equations to equations 3.13 reveal that the fluxes for first-order flux vector splitting may be written as the 1969 MacCormack fluxes plus a second-order

smoothing term.

$$ii=1 \quad (\bar{\bar{P}}\cdot\bar{\bar{S}})^{FS}_{i+1/2} = (\bar{\bar{P}}\cdot\bar{\bar{S}})^{1969}_{i+1/2} + (A^{-})^{n}_{i,j}[U^{n}_{i+1,j} - U^{n}_{i,j}] \qquad (13.15\ a)$$

$$ii=i+1 \quad (\bar{\bar{P}}\cdot\bar{\bar{S}})^{FS}_{i+1/2} = (\bar{\bar{P}}\cdot\bar{\bar{S}})^{1969}_{i+1/2} - (A^{+})^{n+1}_{i+1,j}[U^{n+1}_{i+1,j} - U^{n+1}_{i,j}] \qquad (13.15\ b)$$

Clearly, the first-order flux splitting is more dissipative than the 1969 MacCormack method. As a result the first-order flux splitting is considerably more robust than the 1969 MacCormack method, but less accurate. The first-order accurate method has other numerical advantages when used in an implicit method. These will be discussed later.

Second-Order Flux Vector Splitting

The accuracy of the flux split method can be improved to second-order by using better approximations for U at the surface. As shown in Figure 3.7, first-order flux vector splitting is equivalent to a zeroth-order extrapolation of the solution, U, from the neighboring cell centers to the surface. Second-order accuracy is obtained by using a linear extrapolation instead (for simplicity the Jacobians are evaluated as they were for the first-order flux splitting).

$$(\bar{\bar{P}}\cdot\bar{\bar{S}})^{FS2}_{i+1/2} = (A^{+})^{nc}_{ii,j}\ (U^{-})_{i+1/2} + (A^{-})^{nc}_{ii,j}\ (U^{+})_{i+1/2} \qquad (3.16\ a)$$

$$(\bar{P}\cdot\bar{S})^{FS2}_{j+1/2} = (A^+)^{nc}_{i,jj}\,(U^-)_{j+1/2} + (A^-)^{nc}_{i,jj}\,(U^+)_{j+1/2} \quad (3.16\ b)$$

where

$$(U^-)^{nc}_{i+1/2} = U^{nc}_{i,j} + \phi^-_{i+1/2}\,(U^{nc}_{i,j} - U^{nc}_{i-1,j}) \quad (3.17\ a)$$

$$(U^+)^{nc}_{i+1/2} = U^{nc}_{i+1,j} + \phi^+_{i+1/2}\,(U^{nc}_{i+1,j} - U^{nc}_{i+2,j}) \quad (3.17\ b)$$

As with the first-order flux vector splitting this is obtained as terms that are added onto the 1969 MacCormack method.

$$\begin{aligned} ii=i:\ (\bar{P}\ \bar{S})^{FS2}_{i+1/2} &= (\bar{P}\ \bar{S})^{1969}_{i+1/2} + (A^-)^{nc}_{i,j}[U^{nc}_{i+1,j} - U^{nc}_{i,j}] \\ &+ \phi^-_{i+1/2}(A^+)^{nc}_{i,j}[U^{nc}_{i,j} - U^{nc}_{i-1,j}] \\ &+ \phi^+_{i+1/2}(A^-)^{nc}_{i,j}[U^{nc}_{i+1,j} - U^{nc}_{i+2,j}] \end{aligned} \quad (3.18\ a)$$

$$\begin{aligned} ii=i+1:\ (\bar{P}\ \bar{S})^{FS2}_{i+1/2} &= (\bar{P}\ \bar{S})^{1969}_{i+1/2} \\ &- (A^+)^{nc}_{i+1,j}[U^{nc}_{i+1,j} - U^{nc}_{i,j}] \\ &+ \phi^-_{i+1/2}(A^+)^{nc}_{i+1,j}[U^{nc}_{i,j} - U^{nc}_{i-1,j}] \\ &+ \phi^+_{i+1/2}(A^-)^{nc}_{i+1,j}[U^{nc}_{i+1,j} - U^{nc}_{i+2,j}] \end{aligned} \quad (3.18\ b)$$

For a mesh with constant spacing $\phi^-_{i+1/2}$ and $\phi^+_{i+1/2}$ are both 0.5. For a mesh without constant spacing there is a choice. The extrapolation can be carried out in physical (x,y) space where the extrapolation would depend upon the stretching, or it may be carried out in computational (i,j) space where the values of $\phi^-_{i+1/2}$ and $\phi^+_{i+1/2}$ remain 0.5. The latter case is much simpler and is used here.

Use of the second-order method presented above will

result in oscillations near shock waves, rapid expansions, and mesh discontinuities. These oscillations lead to instabilities near the sharp corner of the thrust reversing nozzle when large time steps are taken. A commonly used method for eliminating these instabilities is flux limiting. With flux limiting the magnitude of the second-order contribution is reduced in regions of large gradients. The flux limiter used here reduces the coefficients $\phi^-_{i+1/2}$ and $\phi^+_{i+1/2}$ by a term proportional to the first and second differences of pressure

$$\phi^-_{I+1/2} = \max(0.0, 0.5 - CLIM^-) \qquad (3.19\ a)$$

$$\phi^+_{I+1/2} = \max(0.0, 0.5 - CLIM^+) \qquad (3.19\ b)$$

where

$$CLIM^- = \frac{|P_{i+1} - 2P_i + P_{i-1}|}{(P_{i+1} + 2P_i + P_{i-1})} + \frac{|P_{i+1} - P_i|}{(P_{i+1} + P_i)} \qquad (3.20\ a)$$

$$CLIM^+ = \frac{|P_{i+2} - 2P_{i+1} + P_i|}{(P_{i+2} + 2P_{i+1} + P_i)} + \frac{|P_{i+1} - P_i|}{(P_{i+1} + P_i)} \qquad (3.20\ b)$$

This form of flux limiting is equivalent to adding a fourth-order smoothing term to the second-order flux split method.

Diffusion Surface Fluxes

The viscous stress and heat conduction terms for a cell surface, equations 2.9, require the evaluation of spacial derivatives of velocity and temperature. These derivatives may be obtained from a generalized transformation.

$$\begin{bmatrix} \frac{\partial u}{\partial \xi} \\ \frac{\partial u}{\partial \eta} \end{bmatrix} = \begin{bmatrix} \frac{\partial x}{\partial \xi} & \frac{\partial y}{\partial \xi} \\ \frac{\partial x}{\partial \eta} & \frac{\partial y}{\partial \eta} \end{bmatrix} \begin{bmatrix} \frac{\partial u}{\partial x} \\ \frac{\partial u}{\partial y} \end{bmatrix} \tag{3.21}$$

$$\begin{bmatrix} \frac{\partial u}{\partial x} \\ \frac{\partial u}{\partial y} \end{bmatrix} = \begin{bmatrix} \frac{\partial x}{\partial \xi} & \frac{\partial y}{\partial \xi} \\ \frac{\partial x}{\partial \eta} & \frac{\partial y}{\partial \eta} \end{bmatrix}^{-1} \begin{bmatrix} \frac{\partial u}{\partial \xi} \\ \frac{\partial u}{\partial \eta} \end{bmatrix} = J_{\xi\eta}^{-1} \begin{bmatrix} \frac{\partial u}{\partial \xi} \\ \frac{\partial u}{\partial \eta} \end{bmatrix} \tag{3.22}$$

Here ξ and η are the coordinate directions for a non-orthogonal coordinate system with ξ running in the i-direction and η running in the j-direction. The components of $J_{\xi\eta}$ can easily be evaluated numerically. For the i+1/2 surface,

$$\frac{\partial x}{\partial \xi} = 0.25(x_{i+1,j+1} - x_{i-1,j+1} + x_{i+1,j} - x_{i-1,j}) \tag{3.23 a}$$

$$\frac{\partial x}{\partial \eta} = x_{i+1,j+1} - x_{i+1,j} \tag{3.23 b}$$

$$\frac{\partial y}{\partial \xi} = 0.25(y_{i+1,j+1} - y_{i-1,j+1} + y_{i+1,j} - y_{i-1,j}) \tag{3.23 c}$$

$$\frac{\partial y}{\partial \eta} = y_{i+1,j+1} - y_{i+1,j} \tag{3.23 d}$$

Also,

$$\frac{\partial u}{\partial \xi} = u_{i+1,j} - u_{i,j} \tag{3.24 a}$$

$$\frac{\partial u}{\partial \eta} = 0.25(u_{i+1,j+1} - u_{i+1,j-1} + u_{i,j+1} - u_{i,j-1}) \tag{3.24 b}$$

The spacial derivatives of v and T are evaluated in the same manner.

V. Implicit Contribution

All of the methods presented so far are explicit and

are limited to small time steps by the following numerical stability criterion:

$$\Delta t \leq \frac{1}{\frac{|u|}{\Delta x} + \frac{|v|}{\Delta y} + c\left[\frac{1}{\Delta x^2} + \frac{1}{\Delta y^2}\right]^{1/2}} \tag{3.25}$$

When solving the Navier-Stokes equations it is necessary to have a very fine mesh near walls so that the velocity gradients within the boundary layer are adequately resolved. Unfortunately, this required that Δx or Δy, and therefore Δt, be very small. In this case the equations are said to be stiff and thousands of time steps are required to solve interesting problems.

The difficulty with explicit schemes for Navier-Stokes solutions arises because explicit schemes require that the time step be smaller than the smallest time scale in the problem. Look at the mesh near a wall where Δy is the direction normal to the wall. Since $\frac{1}{\Delta y}$ is much larger than $\frac{1}{\Delta x}$ the equation for the time step becomes

$$\Delta t \leq \frac{\Delta y}{|v| + c} \tag{3.26}$$

Physically this means that the time step must be smaller than the time required for an acoustic wave to cross the width of the narrowist cell. This time step is unreasonably small for two reasons:

1) The mesh was refined to this degree to resolve velocity gradients within the boundary layer, not accoustical waves.

2) Any inviscid effects this deep in the boundary layer should be completely overwhelmed by the viscous stresses. The term that limits the stability of the method is not even important physically.

The use of implicit methods can eliminate this time step restriction.

The basic idea of implicit methods is to evaluate the fluxes using not only the latest known value of the solution as with the explicit methods, but also the unknown solution currently being sought. In particular, use a weighted average of the fluxes at these two time levels.

$$(\bar{P}\cdot\bar{S})_{i+1/2} = (1-f_{i+1/2})(\bar{P}\cdot\bar{S})^{nc}_{i+1/2} + f_{i+1/2}(\bar{P}\cdot\bar{S})^{nn}_{i+1/2} \tag{3.27}$$

Here $f_{i+1/2}$ is the degree of implicitness which varies from zero (fully explicit) to one (fully implicit) as a function of the local CFL number for the surface.

$$f_{i+1/2} = \text{MAX}\left\{\ 0, 1-\frac{0.5}{CFL}\ \right\} \tag{3.28}$$

As with the explicit methods the flux terms are still evaluated differently between the predictor and corrector steps.

First-Order Flux Splitting

The fluxes for first-order flux splitting are

$$(\bar{P}\cdot\bar{S})^{FS}_{i+1/2} = (1-f_{i+1/2})\left[(A^+)^{nc}_{ii,j}\,U^{nc}_{i,j} + (A^-)^{nc}_{ii,j}\,U^{nc}_{i+1,j}\right] + f_{i+1/2}\left[(A^+)^{nn}_{ii,j}U^{nn}_{i,j} + (A^-)^{nn}_{ii,j}U^{nn}_{i+1,j}\right] \tag{3.29 a}$$

$$(\bar{P}\cdot\bar{S})^{FS}_{j+1/2} = (1-f_{j+1/2})\left[(A^+)^{nc}_{i,jj}U^{nc}_{i,j} + (A^-)^{nc}_{i,jj}U^{nc}_{i,j+1}\right] + f_{j+1/2}\left[(A^+)^{nn}_{i,jj}U^{nn}_{i,j} + (A^-)^{nn}_{i,jj}U^{nn}_{i,j+1}\right] \tag{3.29 b}$$

where nc is the current solution, nn is the new solution being sought, and ii goes through the cycle in table 3.1. Substituting these fluxes into equations 3.5 leads to a nonlinear algebraic system of equations which must be solved on each predictor or corrector step. This is impractical, so the system is linearized. For example, take the two implicit terms for the i+1/2 surface when ii=i.

$$(A^+)^{nn}_{i,j}U^{nn}_{i,j} = (A^+)^{nc}_{i,j}U^{nc}_{i,j} + \frac{\partial[(A^+)_{i,j}U_{i,j}]}{\partial U_{i,j}}\Bigg|^{nc}\delta U_{i,j} + \ldots \tag{3.30 a}$$

$$(A^-)^{nn}_{i,j}U^{nn}_{i+1,j} = (A^-)^{nc}_{i,j}U^{nc}_{i+1,j} + \frac{\partial[(A^-)_{i,j}U_{i+1,j}]}{\partial U_{i,j}}\Bigg|^{nc}\delta U_{i,j} + \frac{\partial[(A^-)_{i,j}U_{i+1,j}]}{\partial U_{i+1,j}}\Bigg|^{nc}\delta U_{i+1,j} \tag{3.30 b}$$

where $\delta U_{i,j} = U^{nn}_{i,j} - U^{nc}_{i,j}$.

These flux vectors are <u>not</u> homogeneous of degree one so

$$\frac{\partial[(A^+)_{i,j}U_{i,j}]}{\partial U_{i,j}} \neq (A^+)_{i,j} \tag{3.31}$$

but the true Jacobian is expensive to calculate so the following is assumed.

$$\frac{\partial[(A^+)_{i,j}\ U_{i,j}]}{\partial U_{i,j}} = (A^+)_{i,j} \tag{3.32 a}$$

$$\frac{\partial[(A^-)_{i,j}\ U_{i+1,j}]}{\partial U_{i,j}} = \emptyset \tag{3.32 b}$$

Substituting into equation 3.29 gives

$$(\bar{P}\cdot\bar{S})^{FS}_{i+1/2} = [(A^+)^{nc}_{ii,j}U^{nc}_{i,j} + (A^-)^{nc}_{ii,j}U^{nc}_{i+1,j}] + f_{i+1/2}[(A^+)^{nc}_{ii,j}\delta U_{i,j} + (A^-)^{nc}_{ii,j}\delta U_{i+1,j}] \tag{3.33 a}$$

$$(\bar{P}\cdot\bar{S})^{FS}_{j+1/2} = [(A^+)^{nc}_{i,jj}U^{nc}_{i,j} + (A^-)^{nc}_{i,jj}U^{nc}_{i,j+1}] + f_{j+1/2}[(A^+)^{nc}_{i,jj}\ \delta U_{i,j} + (A^-)^{nc}_{i,jj}\ \delta U_{i,j+1}] \tag{3.33 b}$$

Substituting these fluxes into equations 3.5 leads to a 4x4 block linear algebraic relationship between $\delta U_{i,j}$ and the δU in four neighboring cells.

$$D_{i,j}\ \delta U_{i+1,j} + B_{i,j}\ \delta U_{i,j+1} + A_{i,j}\ \delta U_{i,j} + C_{i,j}\ \delta U_{i,j-1} + E_{i,j}\ \delta U_{i-1,j} = \Delta U_{i,j} \tag{3.34}$$

where $\delta U_{i,j}$ is the time difference of $U_{i,j}$ obtained from the explicit first order flux split method, and

$$D_{i,j} = f_{i+1/2}\ \frac{\Delta t}{Voli,j}\ (A^-)^{nc}_{ii,j} \tag{3.35 a}$$

$$E_{i,j} = - f_{i+1/2} \frac{\Delta t}{Voli,j} (A^+)^{nc}_{ii-1,j} \qquad (3.35\ b)$$

$$B_{i,j} = f_{j+1/2} \frac{\Delta t}{Voli,j} (A^-)^{nc}_{i,jj} \qquad (3.35\ c)$$

$$C_{i,j} = - f_{j-1/2} \frac{\Delta t}{Voli,j} (A^+)^{nc}_{i,jj-1} \qquad (3.35\ d)$$

$$A_{i,j} = I + \frac{\Delta t}{Voli,j} [f_{i+1/2}(A^+)^{nc}_{ii,j} - f_{i-1/2} (A^-)^{nc}_{ii-1,j} + f_{j+1/2}(A^+)^{nc}_{i,jj} - f_{j-1/2}(A^-)^{nc}_{i,jj-1}] \qquad (3.35\ e)$$

This relationship is expressed more compactly as follows.

$$L_I^{FS}(\delta U_{i,j}) = \Delta U_{i,j} \qquad (3.36)$$

The subscript I indicates that this is an inviscid relationship and the superscript FS indicates that it is first-order flux vector splitting.

When equation 3.36 is applied to each interior cell in the finite volume mesh it leads to a large linear system of block algebraic equations. To complete this system a block algebraic relationship must be provided for each boundary cell as well. The boundary cell relationships are developed in Section VII of this chapter. The algebraic relationships within this system are grouped so that the equation for the (i,j) cell is below the equation for the (i,j+1) cell and above the equation for the (i,j-1) cell. Thus each column of cells is grouped together with equations for the i+1 column being higher in the grouping than the equation for the i column, as shown in Figure 3.8.

The coefficient matrix for this system of algebraic

equations is large, sparse, well structured, and diagonally dominant. For example, a 50x50 mesh will result in 10,000x10,000 coefficient matrices with only 800,000 non-zero elements out of 100,000,000 total elements. Furthermore, the non-zero elements of the coefficient matrix are all contained within 5 bands of 4x4 block matrices, with 3 of these bands clustered near the main diagonal. The principle difficulty with implicit methods is solving this large system of equations efficiently. In this investigation these systems are solved iteratively using a Gauss-Seidel line relaxation method. The motivations for using this method, and the details of this method are discussed in Section VIII of this chapter.

Second-Order Flux Splitting

The fluxes for the implicit, second-order flux vector splitting method are obtained from equations 3.33 by replacing all $\delta U_{i,j}$ by $\delta U^{-}_{i+1/2} = \delta U_{i,j} + \phi^{-}_{i+1/2} (\delta U_{i,j} - \delta U_{i-1,j})$ and $\delta U_{i+1,j}$ by $\delta U^{+}_{i+1/2} = \delta U_{i+1,j} + \phi^{+}_{i+1/2} (\delta U_{i+1,j} - \delta U_{i+2,j})$

$$
\begin{aligned}
(\bar{P}\cdot\bar{S})^{FS2}_{i+1/2} = {} & [(A^{+})_{ii,j} (U_{i,j} + \phi^{-}_{i+1/2} (U_{i,j} - U_{i-1,j}))] \\
& + (A^{-})_{ii,j} (U_{i+1,j} + \phi^{+}_{i+1/2}(U_{i+1,j} - U_{i+2,j}))]^{nc} \\
& + f_{i+1/2} [(A^{+})^{nc}_{ii,j}(\delta U_{i,j} + \phi^{-}_{i+1/2}(\delta U_{i,j} - \delta U_{i-1,j})) \\
& + (A^{-})^{nc}_{ii,j} (\delta U_{i+1,j} + \phi^{-}_{i+1/2}(\delta U_{i+1,j} - \delta U_{i+2,j}))]
\end{aligned}
\qquad (3.37\ a)
$$

$$(\bar{P}\cdot\bar{S})^{FS2}_{j+1/2} = [(A^+)_{i,jj}\,(U_{i,j} + \phi^-_{j+1/2}(U_{i,j} - U_{i,j-1})) + (A^-)_{i,jj}\,(U_{i,j+1} + \phi^+_{j+1/2}\,(U_{i,j+1} - U_{i,j+2}))]^{nc} + f_{j+1/2}\,[(A^+)^{nc}_{i,jj}\,(\delta U_{i,j} + \phi^-_{j+1/2}(\delta U_{i,j} - \delta U_{i,j-1})) + (A^-)^{nc}_{i,jj}\,(\delta U_{i,j+1} + \phi^+_{j+1/2}\,(\delta U_{i,j+1} - \delta U_{i,j+2}))] \qquad (3.37\ b)$$

Substituting these fluxes into equations 3.5 yields a 4x4 block linear algebraic relationship between $\delta U_{i,j}$ and the δU in cells (j+1,j), (i+2,j), (i-1,j), (i-2,j), (i,j+1), (i,j+2), (i,j-1), and (i,j-2).

$$D2_{i,j}\delta U_{i+2,j} + D_{i,j}\delta U_{i+1,j} + B2_{i,j}\delta U_{i,j+2} + B_{i,j}\delta U_{i,j+1} + A_{i,j}\delta U_{i,j} + C_{i,j}\delta U_{i,j+1} + C2_{i,j}\delta U_{i,j+2} + E_{i,j}\delta U_{i+1,j} + E2_{i,j}\delta U_{i+2,j} = \Delta U_{i,j} \qquad (3.38)$$

where, $\Delta U_{i,j}$ is the time difference of $U_{i,j}$ obtained from the explicit second order flux split method, and

$$D2_{i,j} = \frac{\Delta t}{Voli,j}\,[-f_{i+1/2}\,\phi^+_{i+1/2}\,(A^-)^n_{ii,j}] \qquad (3.39\ a)$$

$$D_{i,j} = \frac{\Delta t}{Voli,j}\,[f_{i+1/2}\,(1 + \phi^+_{i+1/2})(A^-)^n_{ii,j} + f_{i-1/2}\,\phi^+_{i-1/2}(A^-)^n_{ii-1,j}] \qquad (3.39\ b)$$

$$E2_{i,j} = \frac{\Delta t}{Voli,j}\,[+f_{i-1/2}\,\phi^-_{i-1/2}(A^+)^n_{i-1,j}] \qquad (3.39\ c)$$

$$E_{i,j} = \frac{\Delta t}{Voli,j}\,[-f_{i-1/2}(1 + \phi^-_{i-1/2})(A^+)^n_{ii-1,j} - f_{i+1/2}\,\phi^-_{i+1/2}(A^+)^n_{ii,j}] \qquad (3.39\ d)$$

$$B2_{i,j} = \frac{\Delta t}{Voli,j}\,[-f_{j+1/2}\,\phi^-_{j+1/2}(A^-)^{nc}_{i,jj}] \qquad (3.39\ e)$$

$$B_{i,j} = \frac{\Delta t}{Voli,j}\,[f_{j+1/2}(1 + \phi^+_{j+1/2})(A^-)^{nc}_{i,jj} + f_{j-1/2}\,\phi^+_{j-1/2}(A^-)^{nc}_{i,jj-1}] \qquad (3.39\ f)$$

$$C2_{i,j} = \frac{\Delta t}{Voli,j} [+f_{j-1/2}\ \phi^{-}_{j-1/2} (A^{+})^{nc}_{i,jj-1}] \qquad (3.39\ g)$$

$$C_{i,j} = \frac{\Delta t}{Voli,j} [-f_{j-1/2}(1 + \phi^{-}_{j-1/2})\ (A^{+})^{nc}_{i,jj-1} - f_{j+1/2}\ \phi^{-}_{j+1/2}\ (A^{+})^{nc}_{i,jj}] \qquad (3.39\ h)$$

$$A_{i,j} = I + \frac{\Delta t}{Voli,j} [f_{i+1/2}\ (1 + \phi^{-}_{i+1/2})(A^{+})^{nc}_{ii,j} - f_{i-1/2}\ (1 + \phi^{+}_{i-1/2})(A^{-})^{nc}_{ii-1,j} + f_{i+1/2}(1 + \phi^{-}_{j+1/2})\ (A^{+})^{nc}_{i,jj} - f_{j-1/2}\ (1 + \phi^{+}_{j-1/2})\ (A^{-})^{nc}_{i,jj-1}] \qquad (3.39\ i)$$

This relationship is expressed more compactly as follows.

$$L_I^{FS2}(\delta U_{i,j}) = \Delta U_{i,j} \qquad (3.40)$$

The subscript I indicates that this is an inviscid relationship and the superscript FS2 indicates that it is second-order flux vector splitting.

The coefficient matrices for this system of algebraic equations is large, sparse, and well structured as in the first-order case. The example 50x50 mesh yields 10,000x10,000 coefficient matricies with 1,440,000 nonzero elements out of 100,000,000 total elements. The nonzero elements of the coefficient matrices are all contained within 9 bands of 4x4 block matrices, with 5 of these bands clustered near the main diagonal. Unlike the coefficient matrices from the first-order flux split method, these matrices are not necessarily diagonally dominant. This is unfortunate because diagonal dominance is a sufficient condition for convergence of the Gauss Seidel line relaxation method.

Diffusion Terms

The implicit contribution to the viscous stress and heat conduction terms is obtained using a thin-layer approximation. To obtain the thin-layer approximation the equations are written in Cartesian coordinates aligned with the cell face. If ξ is the coordinate normal to the surface, and η is the cordinate along the surface then the contribution to the fluxes from the diffusion terms is

$$\bar{P}\cdot\bar{S}^{DIFF} = \begin{bmatrix} \phi \\ \sigma'_\xi \ S_x - \tau'_{\xi\eta} \ S_y \\ \tau'_{\xi\eta} \ S_x + \sigma'_\xi \ S_y \\ u'\sigma'_\xi + v'\tau'_{\xi\eta} + q' \end{bmatrix} |\bar{S}| \qquad (3.42)$$

where

$$\sigma'_\xi = -(\lambda+2\mu)\frac{\delta u'}{\delta \xi} - \lambda\frac{\delta v'}{\delta \eta} \qquad (3.43\ a)$$

$$\tau_{\xi\eta} = -\mu\left(\frac{\delta u'}{\delta \eta} + \frac{\delta v'}{\delta \xi}\right) \qquad (3.43\ b)$$

$$q' = -k\frac{\delta T}{\delta \xi} \qquad (3.43\ c)$$

$u' = S_x u + S_y v$ = Velocity normal to surface

$v' = -S_y u + S_x v$ = Velocity tangent to surface

The thin-layer approximation is obtained by neglecting all derivatives in the η direction.

$$\sigma'_\xi = -(\lambda+2\mu)\frac{\delta u'}{\delta \xi} \qquad (3.44\ a)$$

$$\tau'_{\xi\eta} = -\mu\frac{\delta v'}{\delta \xi} \qquad (3.44\ b)$$

The thin-layer diffusion fluxes can then be written.

$$\bar{P}\cdot\bar{S}^{T.L.} = -\begin{bmatrix} \emptyset \\ (\lambda+2\mu)\frac{\partial u'}{\partial \xi} S_x - \mu\frac{\partial v'}{\partial \xi} S_y \\ \mu\frac{\partial v'}{\partial \xi} S_x + (\lambda+2\mu)\frac{\partial u'}{\partial \xi} S_y \\ u'(\lambda+2\mu)\frac{\partial u'}{\partial \xi} S_x + v'\mu\frac{\partial v'}{\partial \xi} S_y + k\frac{\partial T}{\partial \xi} \end{bmatrix} |\bar{S}| \qquad (3.45)$$

$$= -\begin{bmatrix} 1 & \emptyset & \emptyset & \emptyset \\ \emptyset & S_x - S_y & \emptyset & \emptyset \\ \emptyset & S_y & S_x & \emptyset \\ \emptyset & \emptyset & \emptyset & 1 \end{bmatrix} \begin{bmatrix} \emptyset & \emptyset & \emptyset & \emptyset \\ \emptyset & (\lambda+2\mu) & \emptyset & \emptyset \\ \emptyset & \emptyset & \mu & \emptyset \\ \emptyset & u'(\lambda+2\mu) & \mu v' & k \end{bmatrix} \begin{bmatrix} \frac{\partial \rho}{\partial \xi} \\ \frac{\partial u'}{\partial \xi} \\ \frac{\partial v'}{\partial \xi} \\ \frac{\partial T}{\partial \xi} \end{bmatrix} |\bar{S}| \qquad (3.46)$$

The first matrix above rotates from the (ξ,η) coordinate system to the (x,y) coordinate system, R^{-1}. The second is the matrix of diffusion coefficients, M. The vector on the right contains a set of non-conservative variables in the rotated coordinate system, V'. The fluxes may be written in a more compact notation.

$$\bar{P}\cdot\bar{S}^{T.L.} = -R^{-1} M \frac{\partial V'}{\partial \xi} |\bar{S}| = -R^{-1} M R \frac{\partial V}{\partial \xi} |\bar{S}| \qquad (3.47)$$

If ξ is in the i-direction we can approximate the derivative as follows.

$$\frac{\partial V}{\partial \xi} = \frac{V_{i+1,j} - V_{i,j}}{\Delta \xi} = \frac{2|\bar{S}_{i+1/2}|}{(Vol_{i,j} + Vol_{i+1,j})} (V_{i+1,j} - V_{i,j}) \qquad (3.48)$$

Likewise, if ξ is in the j-direction

$$\frac{\partial V}{\partial \xi} = \frac{2|\bar{S}_{j+1/2}|}{(Vol_{i,j} + Vol_{i,j+1})} (V_{i,j+1} - V_{i,j}) \tag{3.49}$$

Substituting into equation 3.47 gives

$$\bar{P}\cdot\bar{S}^{T.L.}_{i+1/2} = - \frac{2|\bar{S}_{i+1/2}|^2}{(Vol_{i+1,j} + Vol_{i,j})} (R^{-1}MR)_{i+1/2}(V_{i+1,j}-V_{i,j}) \tag{3.50 a}$$

$$\bar{P}\cdot\bar{S}^{T.L.}_{j+1/2} = - \frac{2|\bar{S}_{j+1/2}|^2}{(Vol_{i,j+1} + Vol_{i,j})} (R^{-1}MR)_{j+1/2} (V_{i,j+1}-V_{i,j}) \tag{3.50 b}$$

The purpose of the thin-layer approximation is not to get the complete diffusion terms but to provide a simplified implicit contribution to the diffusion terms.

$$\bar{P}\cdot\bar{S}^{(DIFF)}_{i+1/2} = (\text{Explicit Contribution}) - f_{i+1/2}\frac{2|S_{i+1/2}|^2}{(Vol_{i+1,j} + Vol_{i,j})}(R^{-1}MR)_{i+1/2}(V_{i+1,j} - V_{i,j}) \tag{3.51 a}$$

$$\bar{P}\cdot\bar{S}^{(DIFF)}_{j+1/2} = (\text{Explicit Contribution}) - f_{j+1/2}\frac{2|S_{j+1/2}|^2}{(Vol_{i,j+1} + Vol_{i,j})} (R^{-1}MR)_{j+1/2}(V_{i,j+1} - V_{i,j}) \tag{3.51 b}$$

The explicit contribution is the full diffusion terms, with no thin layer approximation, as given by equation 2.9, 3.23, and 3.24.

The above equations may be written in terms of the change in the conservative variables using the

transformation matrix, N.

$$\delta V = N\,\delta U \tag{3.52}$$

Then

$$\bar{P}\cdot\bar{S}^{(DIFF)}_{i+1/2} = \text{(Explicit Contribution)} + (AD^{+})_{i+1/2}\,\delta U_{i,j} + (AD^{-})_{i+1/2}\delta U_{i+1,j} \tag{3.53 a}$$

$$\bar{P}\cdot\bar{S}^{(DIFF)}_{j+1/2} = \text{(Explicit Contribution)} + (AD^{+})_{j+1/2}\,\delta U_{i,j} + (AD^{-})_{j+1/2}\delta U_{i,j+1} \tag{3.53 b}$$

where

$$(AD^{+})_{i+1/2} = + \frac{2f_{i+1/2}|\bar{S}_{i+1/2}|^2}{(Vol_{i,j} + Vol_{i+1,j})}\,(R^{-1}MR)_{i+1/2}N_i \tag{3.54 a}$$

$$(AD^{-})_{i+1/2} = - \frac{2f_{i+1/2}|\bar{S}_{i+1/2}|^2}{(Vol_{i,j} + Vol_{i+1,j})}\,(R^{-1}MR)_{i+1/2}N_{i+1} \tag{3.54 b}$$

$$(AD^{+})_{j+1/2} = + \frac{2f_{j+1/2}|\bar{S}_{j+1/2}|^2}{(Vol_{i,j} + Vol_{i,j+1})}\,(R^{-1}MR)_{j+1/2}N_j \tag{3.54 c}$$

$$(AD^{-})_{j+1/2} = - \frac{2f_{j+1/2}|S_{j+1/2}|^2}{(Vol_{i,j} + Vol_{i,j+1})}\,(R^{-1}MR)_{j+1/2}N_{j+1} \tag{3.54 d}$$

The sum of the flux from second-order flux splitting, equations 3.37, and the flux from the diffusion terms, equations 3.53, are substituted into equations 3.5. The result is a block linear relationship of the same form as that discussed in section V. This relationship may be written compactly as

$$L_I^{FS2}(\delta U_{i,j}) + L_D(\delta U_{i,j}) = \Delta U_{i,j} \tag{3.55}$$

where the explicit diffusion flux is included in $\Delta U_{i,j}$. The diffusion operator is expanded to be a block linear relationship between $\delta U_{i,j}$ and δU in the four neighboring cells.

$$L_D(\delta U_{i,j}) = D^D_{i,j}\delta U_{i+1,j} + B^D_{i,j}\delta U_{i,j+1} + A^D_{i,j}\delta U_{i,j} + C^D_{i,j}\delta U_{i,j-1} + E^D_{i,j}\delta U_{i-1,j} \tag{3.56}$$

where

$$D^D_{i,j} = f_{i+1/2}\ \frac{\Delta t}{Vol\ i,j}\ (AD^-)_{i+1/2,j} \tag{3.57 a}$$

$$E^D_{i,j} = -\ f_{i-1/2}\ \frac{\Delta t}{Voli,j}\ (AD^+)_{i-1/2,j} \tag{3.57 b}$$

$$B^D_{i,j} = f_{j+1/2}\ \frac{\Delta t}{Voli,j}\ (AD^-)_{i,j+1/2} \tag{3.57 c}$$

$$C^D_{i,i} = -\ f_{j-1/2}\ \frac{\Delta t}{Voli,j}\ (AD^+)_{i,j-1/2} \tag{3.57 d}$$

$$A^D_{i,j} = \frac{\Delta t}{Voli,j}\left[f_{i+1/2}\ (AD^+)_{i+1/2,j} - f_{i-1/2}\ (AD^-)_{i-1/2,j} + f_{j+1/2}\ (AD^+)_{i,j+1/2} - f_{j-1/2}\ (AD^-)_{i,j-1/2}\right] \tag{3.57 e}$$

When the block linear relationship of equation 3.55 is applied to each interior cell in the finite volume mesh it yields a large linear system of block algebraic relations which are ordered in the same manner as the case of second-order flux splitting alone. The resulting coefficient matrix has nine nonzero block diagonals with five of these clustered near the main diagonal. This system of equations may be solved in the same manner as the system for the

inviscid terms alone. If the thin-layer approximation had not been used for the implicit contribution to the diffusion terms the resulting system of equations would have been more complicated. For the problems considered in this investigation, treating only the thin layer terms implicitly has proven to yield a stable solution procedure.

VI. Smoothing Terms

A second difference of pressure smoother is included to allow large time steps during the transient phase of steady state calculations. The smoothing is based on simple second order smoothing of the conservative variables.

$$L_s(U_{i,j}) = VS_{i+1/2}(U_{i+1,j} - U_{i,j}) - VS_{i-1/2}(U_{i,j}-U_{i-1,j}) + VS_{j+1/2}\,(U_{i,j+1} - U_{i,j}) - VS_{j-1/2}\,(U_{i,j} - U_{i,j-1}) \tag{3.58}$$

The coefficient for the smoother is proportional to the second difference in pressure.

$$DDP = \frac{|\,P_{i+3/2} - 2P_{i+1/2} + P_{i-1/2}\,|}{(\,P_{i+3/2} + 2P_{i+1/2} + P_{i-1/2})} \tag{3.59}$$

The pressure at a surface is taken to be the average of the pressures in the cells adjacent to the surface. This gives

$$DDP_{i+1/2} = \frac{|\,P_{i+2,j} - P_{i+1,j} - P_{i,j} + P_{i-1,j}\,|}{(P_{i+2,i} + 3P_{i+1,j} + 3P_{i,j} + P_{i-1,j})} \tag{3.60 a}$$

$$DDP_{j+1/2} = \frac{| P_{i,j+2} - P_{i,j+1} - P_{i,j} + P_{i,j-1} |}{(P_{i,j+2} + 3P_{i,j+1} + 3P_{i,j} + P_{i,j-1})} \qquad (3.60\ b)$$

$$VS_{i+1/2} = \max(0,(CS)(DDP_{i+1/2}) - S) \qquad (3.61\ a)$$

$$VS_{j+1/2} = \max(0,(CS)(DDP_{j+1/2}) - S) \qquad (3.61\ b)$$

Since the second difference of pressure is proportional to the square of the mesh spacing this smoothing is actually fourth order.

The smoother is treated fully implicitly so that the U's in equation 3.58 are at the nn time level. Written in delta law form the smoothing contribution becomes

$$\begin{aligned} \text{smoothing} = \frac{\Delta t}{Vol_{i,j}} [& VS_{i+1/2}(U^{nc}_{i+1,j} - U^{nc}_{i,j}) \\ & - VS_{i-1/2}(U^{nc}_{i,j} - U^{nc}_{i-1,j}) \\ & + VS_{i+1/2}(U^{nc}_{i,j+1} - U^{nc}_{i,j}) \\ & - VS_{i-1/2}(U^{nc}_{i,j} - U^{nc}_{i,j-1}) \\ & + VS_{i+1/2}(\delta U_{i+1,j} - \delta U_{i,j}) \\ & - VS_{i-1/2}(\delta U_{i,j} - \delta U_{i-1,j}) \\ & + VS_{j+1/2}(\delta U_{i,j+1} - \delta U_{i,j}) \\ & - VS_{j-1/2}(\delta U_{i,j} - \delta U_{i,j-1})] \end{aligned} \qquad (3.62)$$

The first four lines above are the explicit contribution from the pressure smoothing and are added into ΔU. The remaining four lines are the implicit contribution which form a block algebraic relationship, $L_S(\delta U_{i,j})$, between the five cells with indices (i,j), (i,j+1), (i,j-1), (i+1,j),

and (i-1,j).

When the smoothing in equation 3.62 is added onto equation 3.55 the following relationship results.

$$L_I(\delta U_{i,j}) + L_D(\delta U_{i,j}) + L_S(\delta U_{i,j}) = \Delta U_{i,j} \qquad (3.63)$$

In this relationship the first four lines in equation 3.62 are included in $\Delta U_{i,j}$. The form of this relation, and the resulting system of algebraic equations, is the same as it was before the smoothing terms were added.

VII. Boundary Conditions

Explicit

With the finite volume method the boundaries of a zone are placed at cell interfaces and a layer of boundary cells surrounds the zone. The only purpose of the boundary cells is to satisfy the boundary conditions. For the domain considered there are five possible boundary conditions; solid wall, plane of symmetry, inflow, outflow, and zonal interface.

At solid adiabatic walls the pressure and temperature gradients are assumed to be zero and a no slip (zero velocity at the wall) boundary condition is applied. To resolve the boundary layer the mesh must be refined near the wall so that the cell nearest the wall is deep within the boundary layer. In this case, boundary layer theory shows

that pressure gradient normal to the wall is a higher order effect and can be neglected. Similarly, for adiabatic walls the temperature gradient normal to the wall deep within the boundary layer is negligable. These boundary conditions are satisfied by setting the pressure and internal energy in each boundary cell equal to the pressure and temperature in the interior cell adjacent to the boundary. The no-slip condition is satisfied by setting the velocity in the boundary cell equal and opposite to the velocity in the adjacent interior cell.

The plane of symmetry is a horizontal line at y=Ø. At the plane of symmetry the gradients of pressure, density, temperature and x-components of velocity are all zero. These conditions are satisfied by setting the pressure, density, internal energy, and x-component of velocity in the boundary cell equal to their values in the adjacent interior cell. The y-component of velocity is zero at the plane of symmetry. This condition is satisfied by setting the y-component of velocity in the boundary cell to the negative of the y-component of velocity in the adjacent interior cell.

The treatment of the inflow boundary conditions is guided by the theory of characteristics. A locally one-dimensional flow has four characteristic equations with slopes u, u+c, u, and u-c. If the flow field is supersonic

then all four characteristic equations are propogating information in the positive x-direction. In this case all data must be specified at the inflow boundary. If the flow is subsonic at the inflow boundary, then one of the characteristics, the u-c characteristic, has a negative slope and it propogates information from the interior upstream to the inflow boundary. In this case only three items may be specified at the inflow boundary and the fourth item must be allowed to vary as the solution progresses.

For the case of subsonic inflow, the stagnation pressure, stagnation temperature, and flow angle are specified. These quantities are related to the static pressure and static temperature by the following equations:

$$\frac{p}{p_t} = \left[1 - \frac{\gamma-1}{\gamma+1}\left(\frac{V}{a_*}\right)^2\right]^{\frac{\gamma}{\gamma-1}} \tag{3.64}$$

$$\frac{T}{T_t} = \left[1 - \frac{\gamma-1}{\gamma+1}\left(\frac{V}{a_*}\right)^2\right] \tag{3.65}$$

$$\frac{v}{u} = \mathrm{Tan}(\theta_{IF}) = (\text{Constant}) \tag{3.66}$$

The first two equations above are simply the isentropic relations written in terms of the total velocity, V, and the speed of sound at a sonic throat, a_*. The speed of sound at a sonic throat is calculated from the specified stagnation

temperature.

$$(a_*)^2 = \frac{2}{\gamma+1} RT_t \tag{3.67}$$

Equations 3.64, 3.65, and 3.66 are a system of three equations in four unknowns: p, T, u, and v. To complete the system another equation is needed. For all cases considered the flow angle at the inflow boundary is zero so equation reduces to v=o and the total velocity, V, is equal to the x-component of velocity, u.

The last equation to close the system is the characteristic relation carrying information upstream to the inflow boundary.

$$\frac{\delta p}{\delta t} - \rho c \frac{\delta u}{\delta t} = (u-c)\left[\frac{\delta p}{\delta x} - \rho c \frac{\delta u}{\delta x}\right] \tag{3.68}$$

This equation is forward differenced.

$$\delta p_B - \rho c\, \delta u_B = \frac{(u-c)\Delta t}{\Delta x} [p_I - p_B - \rho c(u_I - u_B)]^n \tag{3.69}$$

The subscripts I and B indicate the first interior cell and the inflow boundary cell, respectively. The prefix δ indicates the forward in time difference of the variable following it.

The algebraic equations 3.64, 3.65 and 3.66 can be

placed in delta law form by considering incremental changes in the variables p, T, and u.

$$\delta p_B = - \frac{2\, p_t}{\gamma+1} \frac{u}{a_*} \left[1 - \frac{\gamma-1}{\gamma+1}\left(\frac{u}{a_*}\right)^2 \right]^{\frac{1}{\gamma-1}} \frac{\delta u_B}{a_*} \qquad (3.70)$$

$$\delta T_B = - 2\frac{\gamma-1}{\gamma+1} \frac{u}{a_*} \frac{\delta u_B}{a_*} \qquad (3.71)$$

$$\delta v = 0 \qquad (3.72)$$

Equations 3.70, 3.71, and 3.72 are three algebraic equations in the three unknowns δp_B, δT_B, and δu_B. They are solved directly for each inflow boundary cell and the pressure, temperature, and velocity are updated.

The delta law formulation of the isentropic relations, equations 3.70 and 3.71, simplifies the implementation of the inflow boundary. Unfortunately, the linearization error allows the stagnation pressure and stagnation temperature to vary from the specified values. To overcome this problem the static pressure and static temperature in each boundary cell is recalculated from equations 3.64 and 3.65 using the updated velocity.

The treatment of outflow boundary conditions is also guided by the theory of characteristics. If the flow normal to the outflow boundary is supersonic then all

characteristics have positive slopes and no information propogates upstream from the boundary cell to the interior cell. In this case the four locally one dimensional characteristic equations are used to update the solution in the boundary cell. If the flow normal to the outflow boundary is subsonic then the u'-c characteristic propogates information upstream from the boundary cell to the interior cell. In this case, one item must be specified at the boundary cell.

For subsonic outflow the static pressure is specified. The remaining variables in the boundary cell are calculated using the three downstream running characteristic equations. As with the variables specified at the inflow boundary, the requirement of constant pressure at the outflow boundary is written in delta law form.

$$\delta p_B = \emptyset \tag{3.73}$$

This equation is combined with the three characterisic relations.

$$\delta\rho_B + \frac{1}{c^2}\delta p_B = -\frac{u'_I \,\Delta t|\bar{s}|}{Vol_I}\left[\rho_B - \rho_I + \frac{1}{c^2}(p_B - p_I)\right] = R_1 \tag{3.74 a}$$

$$\delta p_B + \rho c\,\delta u'_B = -\frac{(u'+c)\Delta t|\bar{s}|}{Vol_I}\left[p_B - p_I + \rho c(u'_B - u'_I)\right] = R_2 \tag{3.74 b}$$

$$\delta v'_B = \frac{u'_I \,\Delta t\,|\bar{s}|}{Vol_I}\left[v'_B - v'_I\right] = R_3 \tag{3.74 c}$$

The above three equations, along with equation 3.73 are four linear algebraic equations in the four unknowns $\delta\rho_B$, $\delta u'_B$, $\delta v'_B$, and δp_B. This system is solved directly and the boundary cell solution is updated.

At the interzone boundaries the solution in the boundary cell is set equal to the solution in the corresponding cell in the adjacent zone.

Implicit

The explicit boundary conditions described previously use the solution at the latest known time level. Implicit boundary conditions, however, depend on the solution at the unknown time level being sought. This means that the solution in the boundary cells is obtained simultaneously with the solution in the interior cells. Since the implicit boundary conditions are generally linearized in the same way as the interior solution procedure the implicit boundary conditions will simply be contributions to the large linear system of algebraic equations described earlier. The goal of this section is to develope implicit versions of the boundary conditions described in the previous section and write them as block algebraic equations relating the solution change in the boundary cell to the change in the solution in the adjacent interior cells.

The first boundary condition considered is for solid walls. For viscous flows the velocity at the wall is zero. To impose this boundary condition it is advantageous to treat the inviscid fluxes separately from the viscous fluxes, in the same manner as these boundary conditions are treated explicity. To enforce zero net flux through the wall δU in the boundary cell is set by reflecting the δU from the first interior cell; this in effect is the treatment used for free-slip wall boundary conditions. The treatment of the viscous fluxes is simply to set the velocity components in δU in the boundary cell to the negative of the velocity components in δU of the first interior cell. Separate treatment of the inviscid and viscous fluxes at the wall assures that no excessive dissipation or spurious numerical fluxes of tangential momentum occur. Details of boundary condition treatment are described below.

The inviscid flux treatment for the no-flow through the wall boundary condition is satisfied by the equation for the boundary cell which relates the change in the solution within the boundary cell to the change in the solution in the adjacent interior cell. The viscous flux treatment for the no-slip boundary condition is implemented by altering the viscous Jacobians in the equation for the adjacent interior cell.

First consider the application of the no-flow boundary condition. This condition is satisfied by the following relation

$$\delta U'_B = E\delta U'_I \tag{3.76}$$

where $\delta U'$ is the change in the conservative variables based on velolcities components normal to the boundary, u', and tangent to the boundary, v'. The conservative variables based on the global coordinate system are obtained from the conservative variables based on the local coordinate system by multiplying the latter by the inverse of the rotation matrix

$$\delta U = R^{-1}\delta U' \ . \tag{3.77}$$

This yields

$$\delta U_B = RER^{-1}\delta U_I \ . \tag{3.78}$$

The E matrix is a reflection matrix:

$$E = \begin{bmatrix} 1 & 0 & 0 & 0 \\ 0 & -1 & 0 & 0 \\ 0 & 0 & 1 & 0 \\ 0 & 0 & 0 & 1 \end{bmatrix} \tag{3.79}$$

The coefficient matrices for this block algebraic equation are loaded into the global coefficient matrix at the position corresponding to the i,j location of the boundary cell. For instance, at j=1, i=3 the coefficient matrices

are written:

$$B_{3,1} = - RER^{-1} \tag{3.80}$$

$$A_{3,1} = I \tag{3.81}$$

and all other coefficient matrices for this cell are zero.

The no-slip boundary condition for the viscous fluxes is satisfied by altering the viscous Jacobians. This is possible because the dependence of the solution in the boundary cell on the solution at the adjacent interior cell is known.

$$\delta U_B = E^{NS} \delta U_I \tag{3.82}$$

where

$$E^{NS} = \begin{bmatrix} 1 & 0 & 0 & 0 \\ 0 & -1 & 0 & 0 \\ 0 & 0 & -1 & 0 \\ 0 & 0 & 0 & 1 \end{bmatrix} \tag{3.83}$$

Now consider the block algebraic relation for the first interior cell and expand it so that the multiplications by the viscous and inviscid Jacobians are separate terms.

$$\ldots + (A^-)\,\delta U_I + (AD^-)\,\delta U_I + (A^+)\,\delta U_B + (AD^+)\,\delta U_B + \ldots \tag{3.84}$$

Use equation 3.82 to write the last term of the above equation in terms of δU_I.

$$\ldots + (A^-)\,\delta U_I + (A^-)\,\delta U_I + (A^+)\,\delta U_B + (AD^+)\,E^{NS}\,\delta U_I + \ldots \tag{3.85}$$

This approach eliminates the dependence of the implicit viscous flux on the change in the solution within the boundary cell. The coefficient matrices for the global matrix are then modified as follows for j=2.

$$C_{i,j} = f_{j-1/2} \frac{\Delta t}{Vol_{i,j}} (A^{+})^{n}_{i,jj-1} \tag{3.86 a}$$

$$A_{i,j} = I - \frac{\Delta t}{Vol_{i,j}} [\ldots + f_{j-1/2}((A^{-})^{n}_{i,jj-1} + (AD^{-})^{n}_{i,j-1/2} + (AD^{+})_{i,j-1/2} E^{NS})] \tag{3.86 b}$$

At a plane of symmetry the inviscid terms are treated the same as they are at a solid wall (free-slip). The viscous terms are treated in a manner similar to that for a solid wall, the only difference being the reflection matrix. For the plane of symmetry

$$\delta U_B = E^{FS} \delta U_I \tag{3.87}$$

where

$$E^{FS} = \begin{bmatrix} 1 & 0 & 0 & 0 \\ 0 & 1 & 0 & 0 \\ 0 & 0 & -1 & 0 \\ 0 & 0 & 0 & 1 \end{bmatrix} \tag{3.88}$$

The plane of symmetry can be located only at j = jl - 1/2 in the interior zones or ie = ile -1/2 in the exterior zones. Consider only the plane of symmetry at the j = jl - 1/2 surface.

At the interior cell adjacent to the plane of symmetry boundary the two modified coefficient matrices for the block algebraic relation are

$$B_{i,jl-1} = f_{jl-1/2} \frac{\Delta t}{Vol_{i,jl-1}} (B^-)^n_{i,j-1} \qquad (3.89\ a)$$

$$A_{i,jl-1} = I - \frac{\Delta t}{Vol_{i,jl-1}} [\ldots + f_{jl-1/2}$$
$$((A^+)_{i,jl-1} + (AD^+)_{i,jl-1/2} + (AD^-)_{i,jl-1} E^{FS}) + \ldots] \qquad (3.89\ b)$$

This is completely equivalent to what was done in the no-slip case except the reflection matrix is different.

To treat the inflow boundary condition implicitly the differencing of the characteristic relation carrying information upstream must be done implicitly. This is done by evaluating the spacial differencing using a weighted average of the difference at the known time level, nc, and the unknown time level, nn.

$$\delta p_B - \rho c \delta u_B = -(1-f_{3/2}) \frac{(u-c)\Delta t}{\Delta x} [p_I - p_B - c(u_I - u_B)]^{nc}$$
$$- f_{3/2} \frac{(u-c)\Delta t}{\Delta x} [(p_I - p_B) - \rho c (u_I - u_B)]^{nn} \qquad (3.90)$$

This equation is rewritten.

$$\delta p_B - \rho c \delta u_B = - \frac{(u-c)\Delta t}{\Delta x} [\, p_I - p_B - \rho c (u_I - u_B)]^{nc}$$

$$- f_{3/2} \frac{(u-c)\Delta t}{\Delta x} [\, \delta p_I - \delta p_B - \rho c (\delta u_I - \delta u_B)] \qquad (3.91\ a)$$

$$\left(1 - f_{3/2} \frac{(u-c)\Delta t}{\Delta x}\right) [\delta p_B - \rho c \delta u_B] + f_{3/2} \frac{(u-c)\Delta t}{\Delta x} [\delta p_I - \rho c \delta u_I]$$

$$= - \frac{(u-c)\Delta t}{\Delta x} [p_I - p_B - c(u_I - u_B)]^{nc} \qquad (3.91\ b)$$

This equation is the implicit equivalent of equation 3.69. Provided that δp_I and δu_I are known this equation, in combination with equations 3.70, 3.71, and 3.72 can be solved for δp_B, δT_B, δu_B, and δv_B.

Equation 3.91 b above is used at the inflow boundary for the interior zones. For the inflow boundaries in the exterior zone a simplified equation is used. This equation is obtained by neglecting the second term of equation 3.91b.

$$\left(1 - f_{3/2} \frac{(u-c)\Delta t}{\Delta x}\right) [\delta p_B - \rho c \delta u_B] =$$

$$- \frac{(u-c)\Delta t}{\Delta x} [p_I - p_B - \rho c (u_I - u_B)]^{nc} \qquad (3.92)$$

The second term of equation 3.91 b is responsible for coupling the inflow boundary condition to the interior solution during the solution of the linear system. The simplified relationship above neglects this coupling. As a result, the modified boundary condition can be applied as if

it were an explicit boundary condition. Yet it retains the unconditional stability of an implicit boundary condition. The advantage of this approach is simplicity.

The outflow boundary conditions are made implicit by evaluating R_1, R_2, and R_3 in equations 3.74, and using a weighted sum of the solution at the known time level nc and the unknown time level nn. The result is

$$(1 + d_1)(\delta\rho_B + \frac{1}{c^2}\delta p_B) - d_1(\delta\rho_I + \frac{1}{c^2}\delta p_I) = R_1^n \qquad (3.93\ a)$$

$$(1 + d_2)(\delta p_B + \rho c\delta u_B') - d_2(\delta p_I - \rho c\delta u_I') = R_2^n \qquad (3.93\ b)$$

$$(1 + d_1)\delta v_B' - d_1\delta v_I' = R_3^n \qquad (3.93\ c)$$

$$(1 + d_4)(\delta p_B - \rho c\delta u_B') - d_4(\delta p_I - \rho c\delta u_I') = R_4^n \text{ - supersonic} \qquad (3.93\ d)$$

$$\delta p_B = \emptyset \quad \text{- subsonic} \qquad (3.93\ e)$$

where

$$d_1 = \frac{u_I'\,\Delta t\,|S|}{Vol_I}\ , \qquad (3.94\ a)$$

$$d_2 = \frac{(u_I'+c)\,\Delta t\,|S|}{Vol_I}\ , \text{ and} \qquad (3.94\ b)$$

$$d_4 = \frac{(u_I'-c)\,\Delta t\,|S|}{Vol_I}\ . \qquad (3.94\ c)$$

These are four equations relating the change of the nonconservative variables in the boundary cell to the change of the nonconservative variables within the first interior

cell. This block linear algebraic relationship is incorporated into the global system of equations when the external zone is not included.

When an external zone is included the terms coupling the exit boundary solution to the interior solution are neglected. The equations for the outflow boundary condition then become

$$(1 + d_1)(\delta\rho_B + \frac{1}{c^2}\delta p_B) = R_1^n \qquad (3.95\ a)$$

$$(1 + d_2)\ (\delta p_B + \rho c \delta u'_B) = R_2^n \qquad (3.95\ b)$$

$$(1 + d_1)\delta v'_B = R_3^n \qquad (3.95\ c)$$

$$(1 + d_4)\ (\delta p_B - \rho c \delta u'_B) = R_4^n \quad \text{- supersonic} \qquad (3.95\ d)$$

$$\delta p_B = \emptyset \quad \text{- subsonic} \qquad (3.95\ e)$$

Since these equations are uncoupled from the global system they are solved first, as if an explicit boundary condition were being used.

The zonal interface boundary conditions along the lines dividing the interior zones are satisfied by simply removing from the global coefficient matrix the rows and columns corresponding to the zonal interface boundary cells. This causes the solution in the cell on one side of the dividing line to interact directly with the solution in the cell on the other side of the zonal dividing line.

The zonal boundary conditions for the dividing lines

between the interior and exterior zones is handled differently. Since the exterior zone uses a different set of indices it is more convenient to solve it as a separate set of equations. The systems of equations for the interior and exterior zones are then approximately solved separately and are coupled together through interation by mearly setting the U within this boundary cell equal to its latest value in the corresponding interior cell of the adjacent zone. Since the systems are solved using an interative method, this zonal coupling procedure is implemented in a manner that is consistent with the overall solution procedure. More details concerning interzone boundary conditions will be provided in Section VIII.

VIII. System of Linear Algebraic Equations

The implicit method presented here requires the solution of a large linear system of algebraic equations on both the predictor and corrector steps. This system is sparse and well structured as shown in Figure 3.81. In particular, this system is composed of 9 bands of 4X4 matrices with 5 of these bands clustered near the main diagonal. The system could be solved directly using a Gaussian elimination procedure. Unfortunately, this system has a large bandwidth and a Gaussian elimination procedure, or variation thereof, would fill all of the elements out to the outermost

diagonal. For a 50X50 mesh this would require storage for 8,000,000 floating point numbers, even though only 360,000 numbers were initially nonzero. Clearly this storage requirement is unacceptable.

The inefficiencies inherent in the direct methods force the use of approximate solution procedures. These methods generally attempt to approximate the solution of the original system by solving a series of simpler systems to which direct methods can be applied efficiently. Two approximate solution procedures were investigated for the linear system of Figure 3.8. In the first, the coefficient matrix for the linear system is approximately factored into the product of two simpler matices. This approach was pioneered by Beam and Warming (Reference 11) and Briley and McDonald (Reference 12) for schemes based on central differencing. The second procedure approximately solves the system using line Gauss-Seidel relaxation.

The approximate factorization approach is to write the coefficient matrix for the system as the product of two simpler matrices as shown in Figure 3.9. In this case the coefficient matrix in Figure 3.8 is factored into a block pentadiagonal matrix and a matrix that may be rearranged by row and column operations to become a block pentadiagonal matrix. The B, B2, C, C2, D, D2, E, and E2 elements indicated in Figure 3.9 are the same as those defined

previously. The AI and AJ matrices are new and are defined below.

$$AI_{i,j} = I + \frac{\Delta t}{Voli,j} [f_{i+1/2} (1 + \phi^{-}_{i+1/2})(A^{+})^{nc}_{ii,j} - f_{i-1/2} (1+\phi^{+}_{i-1/2})(A^{-})^{nc}_{ii-1,j} \quad (3.96\ a)$$

$$AJ_{i,j} = I + \frac{\Delta t}{Voli,j} [f_{j+1/2} (1 +\phi^{-}_{j+1/2})(A^{+})^{nc}_{i,jj} -f_{j-1/2} (1 + \phi^{+}_{j-1/2})(A^{-})^{nc}_{i,jj} \quad (3.96\ b)$$

where the A^{+} and A^{-} Jacobians are defined in equations 3.10 and the ii and jj indices go through the cycle in table 3.1 presented before. The two resulting block pentadiagonal systems are solved consecutively using the block pentadiagonal solver described in Appendix B.

There is an error associated with the approximate factorization because the product of the two component matrices results in a matrix which is different than the desired coefficient matrix. The difference of these two matrices is the approximate factorization error matrix. This matrix is shown in Figure 3.10 for first order flux splitting. Each term of the error matrix involves the product of an i-direction Jacobian with a j-direction Jacobian. Since these Jacobians are proportional to the CFL numbers in the i- and j-directions respectively the product of these Jacobians is proportional to the product of the CFL numbers in the i- and j-directions. In general, then, the

approximate factorization method should perform well when one or both of the i- or j-direction CFL numbers is small, and perform poorly when both the i- and j-direction CFL numbers are large. Unfortunately, thrust reversing nozzles often contain sharp corners and, near a sharp corner, the CFL numbers in both the i- and j-directions are generally large. For these cases the approximate factorization method has an unacceptable limitation on the time step size.

The line Gauss-Seidel relaxation method reduces the bandwidth of the system by taking either the upper or lower off diagonal terms, multiplying them by the solution at the previous iteration level, and subtracting the result from the right hand side of the equation. This effectively applies the contribution of the choosen off diagonal terms as a deferred correction. Define IT as the iteration level. On the even iteration levels (IT even) the lower off diagonal terms are defered and on the odd iteration levels (IT odd) the upper off diagonal terms are deferred. If the coefficient matrix is such that the line Gauss-Seidel relaxation method converges, the approximate solution will approach the correct solution as the number of iterations becomes large. For first-order flux vector splitting the coefficient matrix is diagonally dominant and the line Gauss-Seidel relaxation procedure is guaranteed to converge (diagonal dominance is a sufficient condition for

convergence of a Gauss-Seidel relaxation procedure). For second-order flux vector splitting the coefficient matrix is not diagonally dominant. Despite this, the line Gauss-Seidel relaxation procedure has not diverged for any of the problems attempted.

The implementation of the line Gauss Seidel method is best understood by dividing the coefficient matrix into a large number of submatrices as shown in Figure 3.8. Each row of submatrices is a linear block algebraic equation relating the solutions within five adjacent columns of cells.

$$(D2C)\delta UC_{i+2} + (DC)\delta UC_{i+1} + (AC)\delta UC_{i} + (EC)\delta UC_{i-1} + (E2C)\,\delta UC_{i-2} = \Delta UC_{i} \qquad (3.97)$$

There is one such relationship for each column of cells with the submatrix, AC, being a block pentadiagonal matrix and the submatrices DC, EC, D2C, and E2C being block diagonal matrices. Defining IT as the iteration level the line Gauss Seidel method is implemented as follows.

For IT odd:

1) Set the implicit outflow boundary condition at the right boundary (viewed in the computational plane).

2) Sweep upstream applying the relationship for each column. For the i-column multiply the DC matrix by δUC_{i+1}^{IT}, the D2C matrix by δUC_{i+2}^{IT}, the EC matrix by δUC_{i-1}^{IT-1}, and the

E2C matrix by δUC_{i-2}^{IT-1}. Then subtract the sum of these products from the right hand side and solve the block pentadiagonal system for δUC_i^{IT}. Repeat this until the left boundary is reached.

For IT even:

3) Set the implicit inflow boundary condition at the left boundary (viewed in the computational plane).

4) Sweep downstream repeating the process in step 2 except that DC and D2C now multiply δUC_{i+1}^{IT-1} and δUC_{i+2}^{IT-1}, and EC and E2C now multiply δUC_{i-1}^{IT} and δUC_{i-2}^{IT}.

5) Repeat the process until the desired iteration level has been reached. It was found that only two to four iterations were required to achieve stability and that overall convergences of the time marching procedure was not improved by additional iterations.

The line Gauss-Seidel relaxation procedure was adopted because the time marching scheme based on approximate factorization exhibited undesirable instabilities. For example, one of the test cases is the symmetric, fully deployed thrust reversing nozzle shown in Figure 4.1. The key feature of this nozzle is the sharp corner at the intersection of the lower flap wall with the forward reverser port wall. The initial conditions for the solution are stagnation conditions within the nozzle, a low static pressure at the exit, and zero velocity everywhere. A

physical device that might provide these conditions is a diaphram at the nozzle exit plane which is broken at time t=Ø. When the diaphram is broken an expansion wave travels upstream through the nozzle until the inflow boundary is reached. The inflow boundary conditions then begin pumping enough air through the inflow boundary to keep the stagnation pressure and temperature at the specified values. When approximate factorization is used an instability occurs shortly after the expansion wave has passed the sharp corner.

To determine the cause of the instabilities a numerical experiment was performed using first-order flux vector splitting. The implicit coefficient matrix (for the predictor step), based on the transient flow field shown in Figures 3.11 through 3.13, was solved using both approximate factorization and line Gauss-Seidel relaxation with 2, 3, 4, 5, 6, and 2Ø iterations. Figure 3.14 shows the resulting solutions as a function of the CFL number for the normalized time difference of density, $\delta\rho/\rho$, in the first cell after the corner near the wall. It is clear that the approximate factorization procedure gives poor results in this case but that the line Gauss-Seidel relaxation gives very good results if 3 or more iterations are used. Figure 3.15 shows similar results for the normalized time difference of total energy. While of limited scope, this comparison

provides substantial evidence that the Gauss-Seidel relaxation procedure is superior for flows with sharp corners.

The time marching scheme based on the line Gauss-Seidel relaxation procedure has been successfully applied to this fully deployed thrust reversing nozzle. Details of these calculations are given in Chapter 4, Section 2, but it is significant to note that this method was stable with CFL numbers an order of magnitude larger than the CFL number at which the approximately factored method was unstable.

IX. Accuracy and Stability Analysis for Model Equation

The solution procedure presented in the preceeding sections is a two-step explicit-implicit method. This method locally varies the degree of implicitness so that the procedure is explicit in regions where the explicit stability criterion is satisfied, and fully implicit when the explicit stability criterion is exceeded significantly. In this section the accuracy of this method is analyzed at its two extremes (explicit and fully implicit) for the following simple model equation (the linear wave equation).

$$u_t + \lambda u_x = 0$$

Also in this section, the fully implicit method is shown to be unconditionally stable.

Accuracy

First consider the two-step explicit method, with spacially second-order upwind differencing, applied to the wave equation.

$$\overline{u_i^{n+1}} = u_i^n - c(\tfrac{3}{2}u_i^n - \tfrac{4}{2}u_{i-1}^n + \tfrac{1}{2}u_{i-2}^n) \qquad (3.98\ a)$$

$$u_i^{n+1} = \tfrac{1}{2}u_i^n + \tfrac{1}{2}\overline{u_i^{n+1}} - \tfrac{1}{2}c(\tfrac{3}{2}\overline{u_i^{n+1}} - \tfrac{4}{2}\overline{u_{i-1}^{n+1}} + \tfrac{1}{2}\overline{u_{i-2}^{n+1}}) \qquad (3.98\ b)$$

where $c = \frac{\lambda \Delta t}{\Delta x}$

This two-step scheme may be combined to form a single-step scheme in the linear case.

$$u_i^{n+1} = u_i^n - c(\tfrac{3}{2}u_i^n - \tfrac{4}{2}u_{i-1}^n + \tfrac{1}{2}u_{i-2}^n) + \frac{c^2}{2}(\tfrac{9}{4}u_i^n - \tfrac{24}{4}u_{i-1}^n + \tfrac{22}{4}u_{i-2}^n - \tfrac{8}{4}u_{i-3}^n + \tfrac{1}{4}u_{i-4}^n) \qquad (3.99)$$

To evaluate the accuracy of this method the values of u at positions other than (i,n) are approximated using Taylor series expansions about point (i,n). Proceeding in this manner, it is found that the second term on the right hand side of equation 3.99 is a second-order accurate approximation to the first partial derivative of u with respect to x.

$$\tfrac{3}{2}u_i^n - \tfrac{4}{2}u_{i-1}^n + \tfrac{1}{2}u_{i-2}^n = [\Delta x\ u_x - \tfrac{1}{3}\Delta x^3 u_{xxx} + O(\Delta x^5)]_i^n \qquad (3.100)$$

Likewise, the last term is a second-order accurate approximation to the second partial derivative of u with respect to x.

$$\frac{9}{4}u_i^n - \frac{24}{4}u_{i-1}^n + \frac{22}{4}u_{i-2}^n - \frac{8}{4}u_{i-3}^n + \frac{1}{4}u_{i-4}^n$$

$$= [\Delta x^2 u_{xx} - \frac{2}{3}\Delta x^4 u_{xxxx} + \emptyset(\Delta x^5)]_i^n \qquad (3.101)$$

Equations 3.100 and 3.101 are substituted into equation 3.99, along with a Taylor series expansion for u_i^{n+1}. The result is

$$u_t + \lambda u_x = -\frac{\Delta t}{2}[u_{tt} - \lambda^2 u_{xx}] + \frac{\lambda}{3}\Delta x^2 u_{xxx} + H.O.T. \qquad (3.102)$$

The leading term in the truncation error is eliminated by differentiating equation 3.102 with respect to t and subtracting λ times the derivative of equation 3.102 with respect to x.

$$u_{tt} - \lambda^2 u_{xx} = -\frac{\Delta t}{2}[u_{ttt} - \lambda u_{ttx} - \lambda^2 u_{txx} + \lambda^3 u_{xxx}] + H.O.T. \qquad (3.103)$$

Substituting into equation 3.102 yields:

$$u_t + \lambda u_x = +\frac{\Delta t^2}{4}[u_{ttt} - \lambda u_{ttx} - \lambda^2 u_{txx} + \lambda^3 u_{xxx}] + \frac{\lambda}{3}\Delta x^2 u_{xxx} + H.O.T. \qquad (3.104)$$

The first term of the truncation error in equation 3.104 can be eliminated in a similar manner. The reduced equation is the wave equation with the leading term being of order Δx^2.

$$u_t + u_x = \frac{\lambda}{3}\Delta x^2 u_{xxx} \qquad (3.105)$$

The two step explicit method with second order upwind differencing is therefore second order accurate in both space and time.

Now consider the fully implicit procedure with spacially second order upwind differencing.

$$u_i^{\overline{n+1}} = u_i^n - c[\frac{3}{2}u_i^{\overline{n+1}} - \frac{4}{2}u_{i-1}^{\overline{n+1}} + \frac{1}{2}u_{i-2}^{\overline{n+1}}] \qquad (3.106\ a)$$

$$u_i^{\overline{n+2}} = u_i^{\overline{n+1}} - c\{\frac{3}{2}u_i^{\overline{n+2}} - \frac{4}{2}u_{i-1}^{\overline{n+2}} + \frac{1}{2}u_{i-2}^{\overline{n+2}}\} \qquad (3.106\ b)$$

$$u_i^{n+1} = \frac{1}{2}\{u_i^n + u_i^{\overline{n+2}}\} \qquad (3.106\ c)$$

Equation 3.106 may be combined, in the linear case, to form a single step scheme.

$$\begin{aligned} u_i^{n+1} - u_i^n &= c[\tfrac{3}{2}u_i^n - \tfrac{4}{2}u_{i-1}^n + \tfrac{1}{2}u_{i-2}^n] \\ &\quad - 2c[\tfrac{3}{2}u_i^{n+1} - \tfrac{4}{2}u_{i-1}^{n+1} + \tfrac{1}{2}u_{i-2}^{n+1}] \\ &\quad + \frac{c^2}{8}[9u_i^n - 24u_{i-1}^n + 22u_{i-2}^n - 8u_{i-3}^n + u_{i-4}^n] \\ &\quad - \frac{c^2}{4}[9u_i^{n+1} - 24u_{i-1}^{n+1} + 22u_{i-2}^{n+1} - 8u_{i-3}^{n+1} + u_{i-4}^{n+1}] \end{aligned} \qquad (3.107)$$

For this equation it is best to expand the Taylor series about the point (i,n+1). The results for the four terms following the equals sign in equation 3.107 are given below.

$$\frac{3}{2}u_i^n - \frac{4}{2}u_{i-1}^n + \frac{1}{2}u_{i-2}^n = [\Delta x\, u_x - 3\Delta t\Delta x\, u_{tx}]_i^{n+1} + H.O.T. \qquad (3.108\ a)$$

$$\frac{3}{2}u_i^{n+1} - \frac{4}{2}u_{i-1}^{n+1} + \frac{1}{2}u_{i-2}^{n+1} = [\Delta x u_x - \frac{\Delta x^3}{3}u_{xxx}]_i^{n+1} + H.O.T. \qquad (3.108\ b)$$

$$\frac{9}{4}u_i^n - \frac{24}{4}u_{i-1}^n + \frac{22}{4}u_{i-2}^n - \frac{8}{4}u_{i-3}^n + \frac{1}{4}u_{i-4}^n$$
$$= [\Delta x^2 u_{xx} - 4\Delta t\Delta x^2 u_{txx}]_i^{n+1} + H.O.T. \qquad (3.108\ c)$$

$$\frac{9}{4}u_i^{n+1} - \frac{24}{4}u_{i-1}^{n+1} + \frac{22}{4}u_{i-2}^{n+1} - \frac{8}{4}u_{i-3}^{n+1} + \frac{1}{4}u_{i-4}^{n+1}$$
$$= [\Delta x^2 u_{xx} - \frac{2}{3}\Delta x^4 u_{xxxx}]_i^{n+1} \qquad (3.108\ d)$$

Equations 3.108 are substituted into equation 3.107, along with a Taylor series expansion to u_i^n.

$$(u_t + \lambda u_x) = \frac{\Delta t}{2}(u_{tt} - 6\lambda u_{tx} - \lambda^2 u_{xx}) + H.O.T. \qquad (3.109)$$

This equation is reduced in the same way that equation 3.102 is reduced. The resulting reduced equation is

$$u_t + \lambda u_x = 3\Delta t\lambda^2 u_{xx} + \emptyset(\Delta t^2, \Delta x^2) \qquad (3.110)$$

The fully implicit method with spacially second order upwind differencing is second order accurate in space, first order accurate in time.

Stability

The stability of the fully implicit scheme is studied using a Von Neumann stability analysis. The analysis consists of writing the solution as a Fourier series and searching for frequencies for which the error grows exponentially.

$$u(x,t) = \sum b_m(t) e^{ikmx} \qquad (3.111)$$

Since the model equation is linear, it is sufficient to consider an arbitrary term of the Fourier series:

$$u_m(x,t) = b_m(t)e^{ikmx} \tag{3.112}$$

This allows the solution at the point (i-1,n) to be conveniently written in terms of solution at the point (i,n).

$$u_m(x_{i-1},t^n) = u_m(x_i,t^n)\ e^{-i\beta} \tag{3.113}$$

where β=km x is a frequency parameter.

Apply the analysis to equations 3.106

$$u_i^{\overline{n+1}} = g_1\ u_i^n \tag{3.114 a}$$

$$u_i^{\overline{n+2}} = g_2\ u_i^{\overline{n+1}} = g_1\ g_2\ u_i^n \tag{3.114 b}$$

$$u_i^{n+1} = \frac{1}{2}\{1 + g_1\ g_2\}\ u_i^n = g_3 u_i^n \tag{3.114 c}$$

where

$$g_1 = g_2 = \frac{1}{1 + c[\frac{3}{2} - \frac{4}{2}e^{-i\beta} + \frac{1}{2}e^{-i\beta}]} \tag{3.115}$$

For the scheme to be stable the modulus of amplification factor, g_3, must be less than or equal to one. This is equivalent (equations 3.114 c and 3.115) to requiring the modulus of g_1 to be less than or equal to one. Thus the

modulus of the denominator of equation 3.115 must be greater than or equal to one.

$$\left|\frac{1}{g_1}\right| = \left| 1 + c\left[\frac{3}{2} - \frac{4}{2}e^{-i\beta} + \frac{1}{2}e^{-i2\beta}\right]\right| \geq 1 \qquad (3.116)$$

Expand equation 3.116 in terms of the trigonometric functions and multiply by its conjugate.

$$\left|\frac{1}{g_1}\right|^2 = \left\{ 1 + c\left[\frac{3}{2} - \frac{4}{2}\cos\beta + \frac{1}{2}\cos 2\beta\right]\right\}^2 + c^2\left[\frac{4}{2}\sin\beta - \frac{1}{2}\sin 2\beta\right]^2 \qquad (3.117\ a)$$

$$\left|\frac{1}{g_1}\right|^2 = (Re)^2 + (Im)^2 \qquad (3.117\ b)$$

The term $(Im)^2$ is always greater than or equal to zero, therefore having $(Re)^2$ greater than or equal to one is sufficient for the stability of the scheme. Expand $\cos 2\beta$ in equation 3.117 a using the double angle formula.

$$(Re) = 1 + c\left[\frac{3}{2} - \frac{4}{2}\cos\beta + \cos^2\beta - \frac{1}{2}\right] \qquad (3.118\ a)$$

$$(Re) = 1 + c(1 - \cos\beta)^2 \qquad (3.118\ b)$$

From equation 3.118 b it is clear that (Re) is always greater than one. The fully implicit method is therefore unconditionally stable.

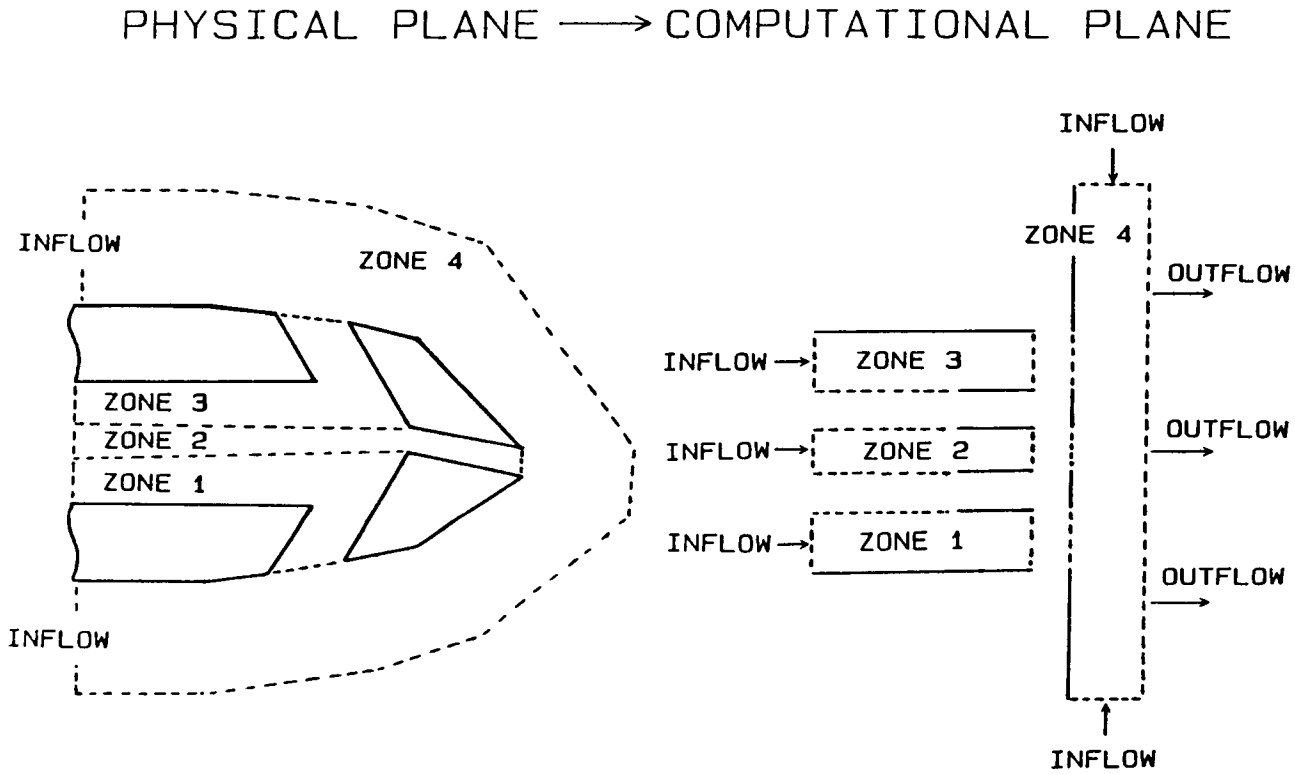

Figure 3.1 Zonal Arrangement for Thrust Reversing and Thrust Vectoring Nozzle Program.

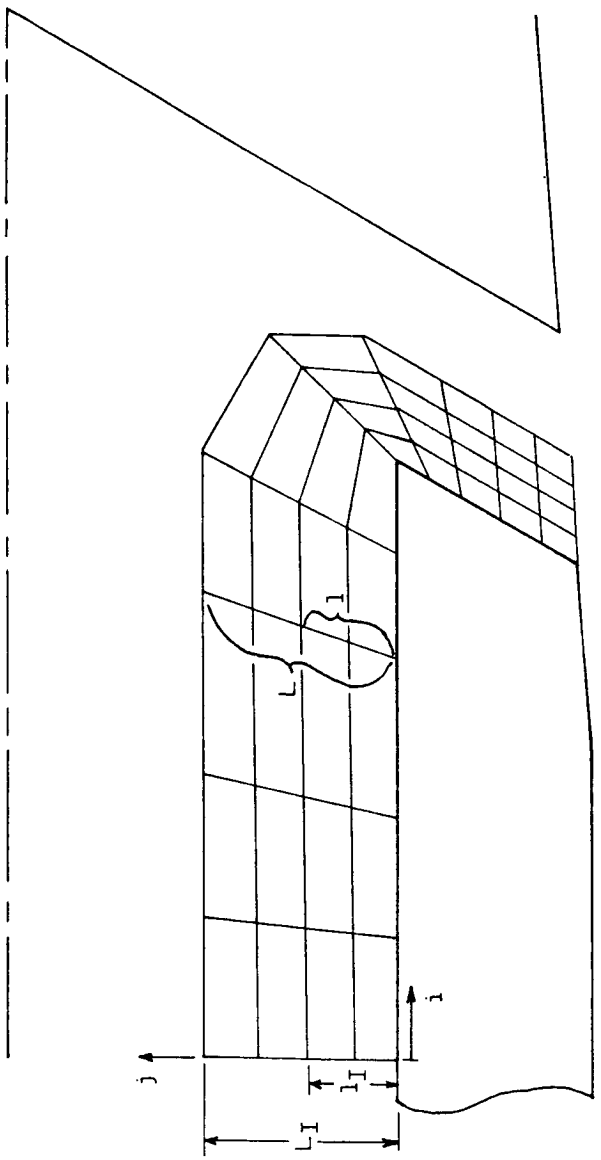

Figure 3.2 A Region in the Interior Mesh.

A = Total Arclength Along Inner Boundary of Region.
a = Arlength to Current Line Along Inner Boundary of Region.

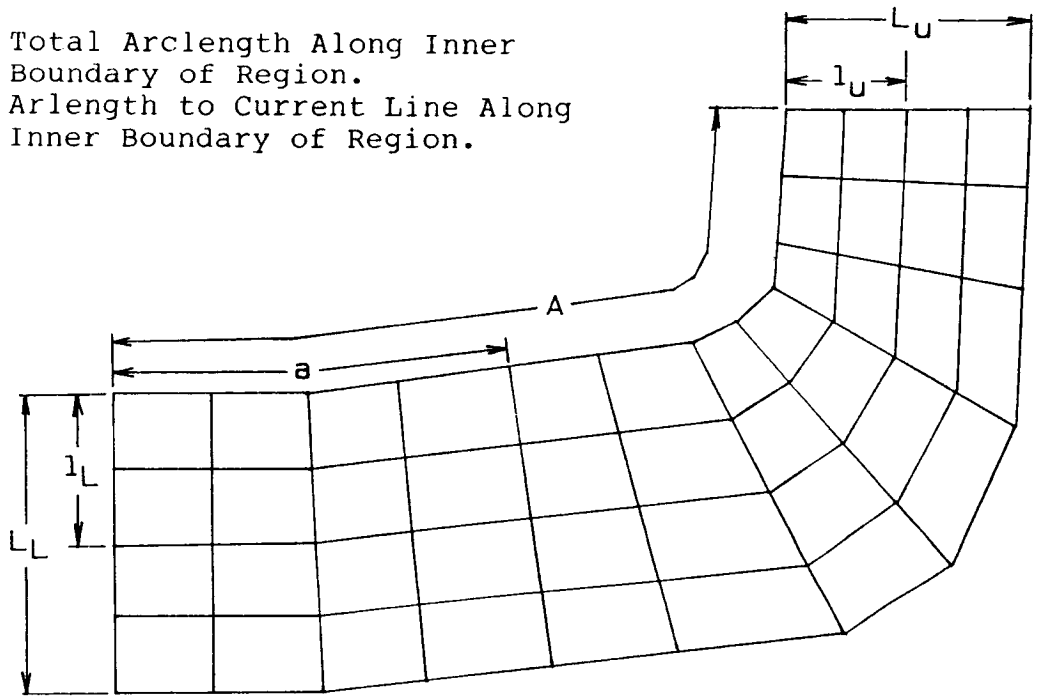

Figure 3.3 A Region in the Exterior Zone.

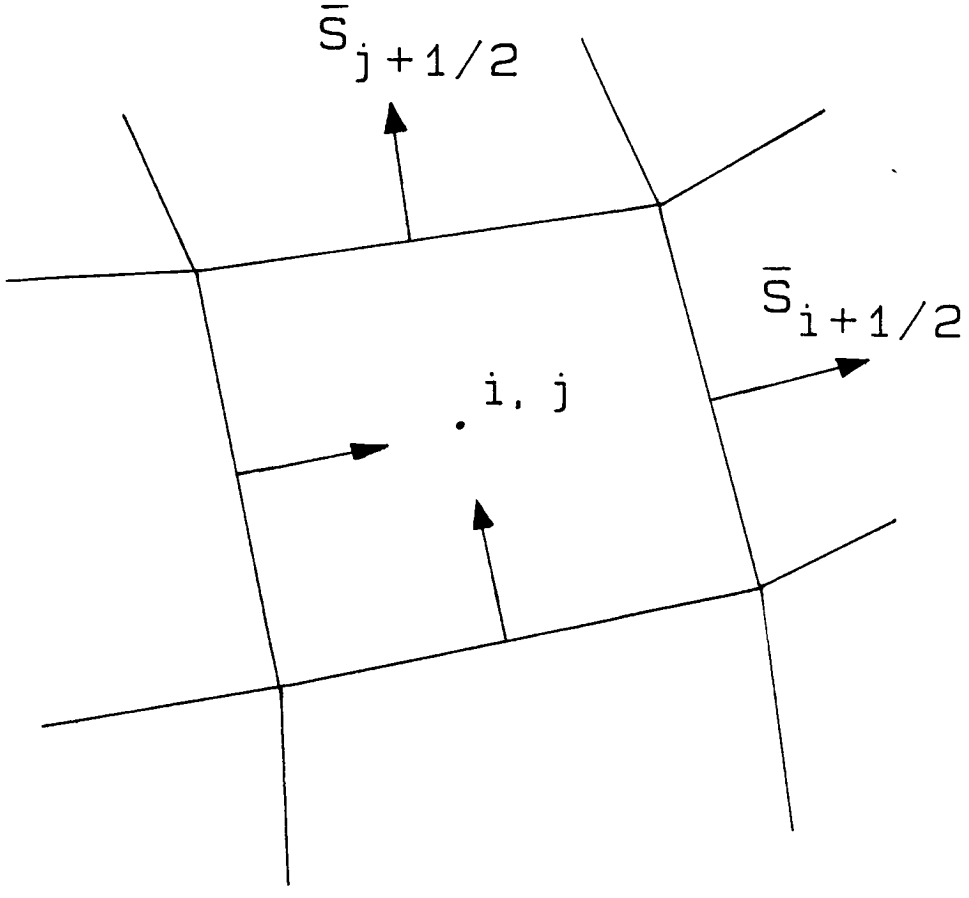

Figure 3.4 Finite volume cell.

C-2

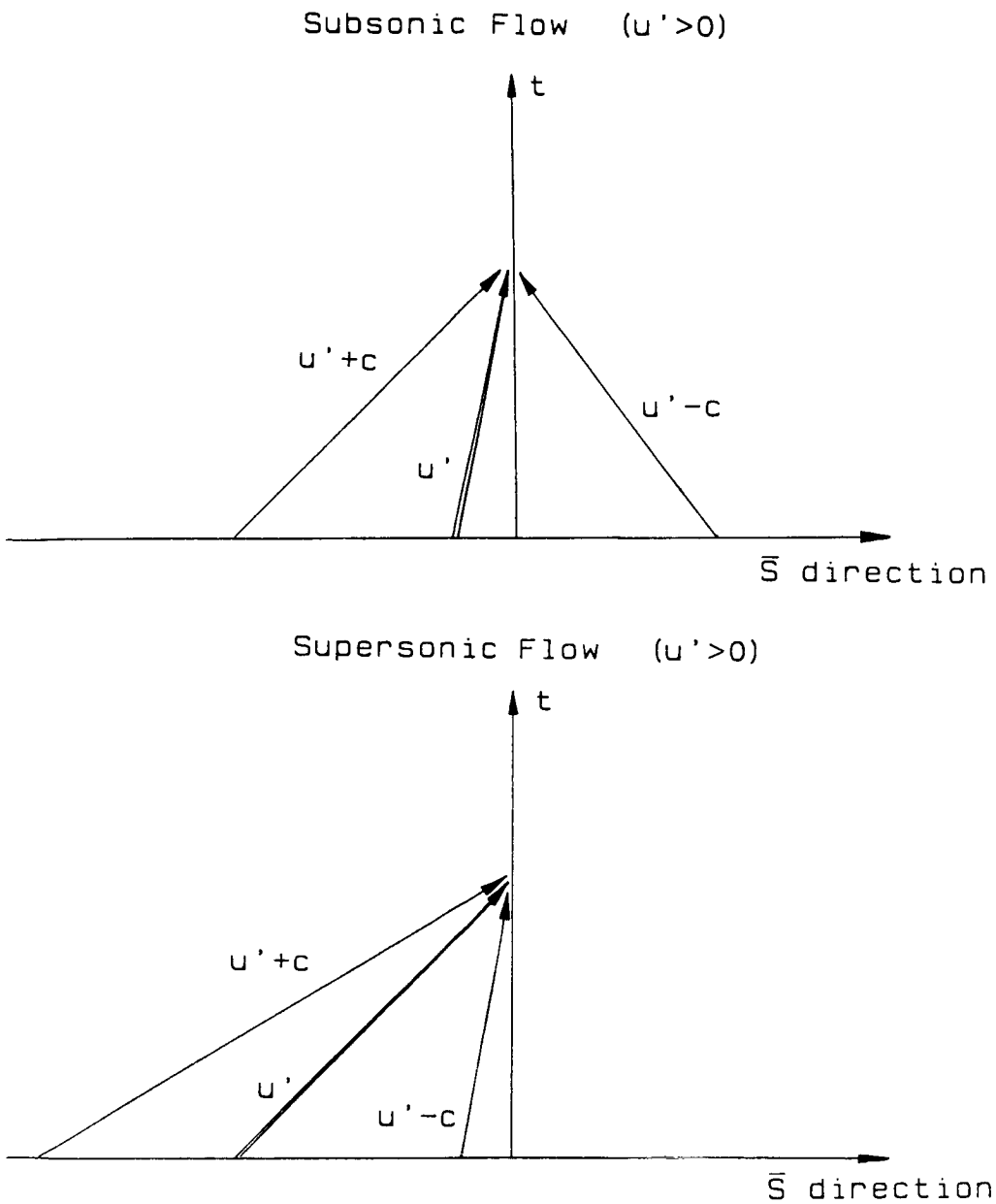

Figure 3.5 Propagation of Information Along Locally One-Dimensional Time Dependent Characteristics.

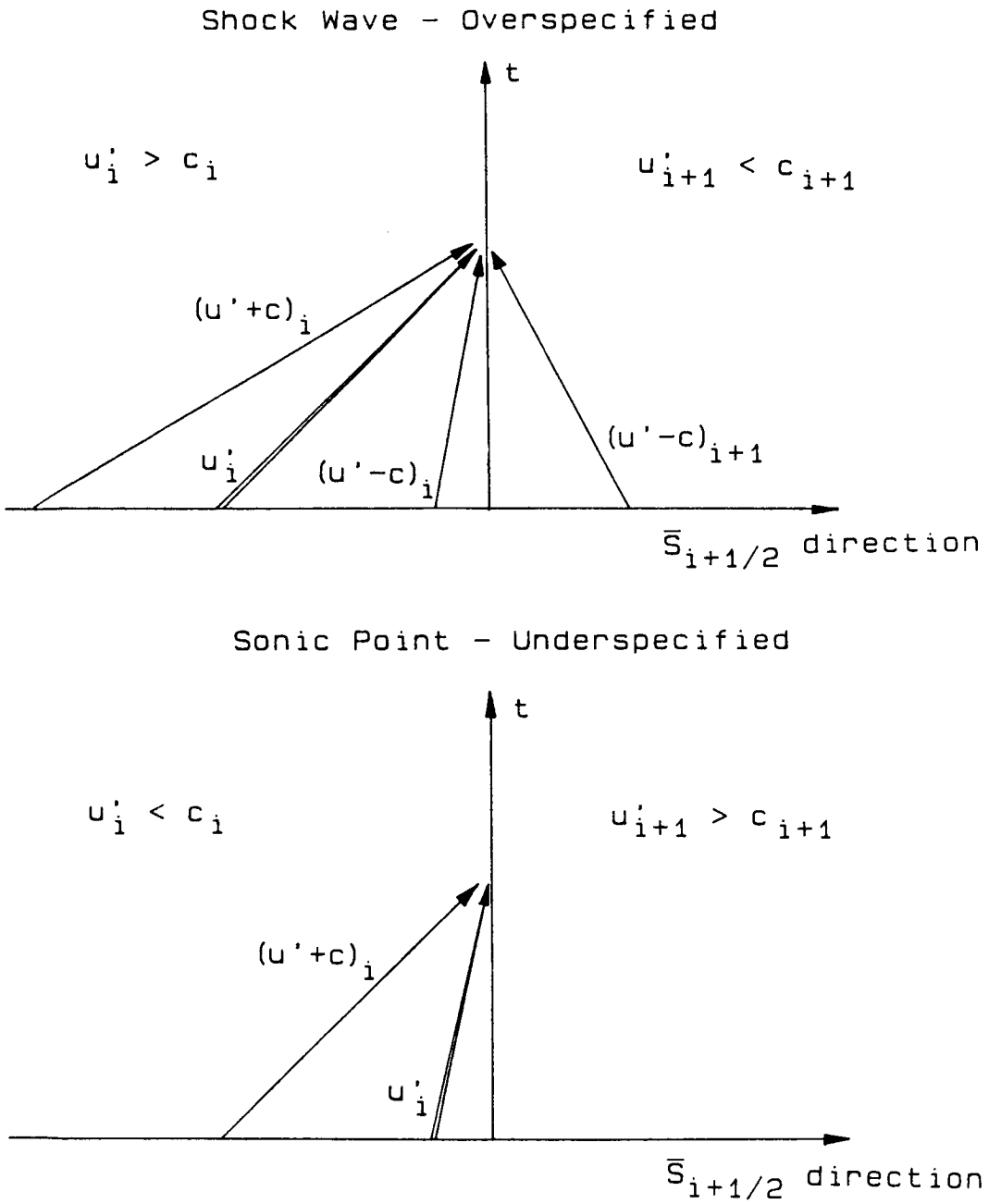

Figure 3.6 Characteristics Resulting from Steger and Warming Flux Splitting.

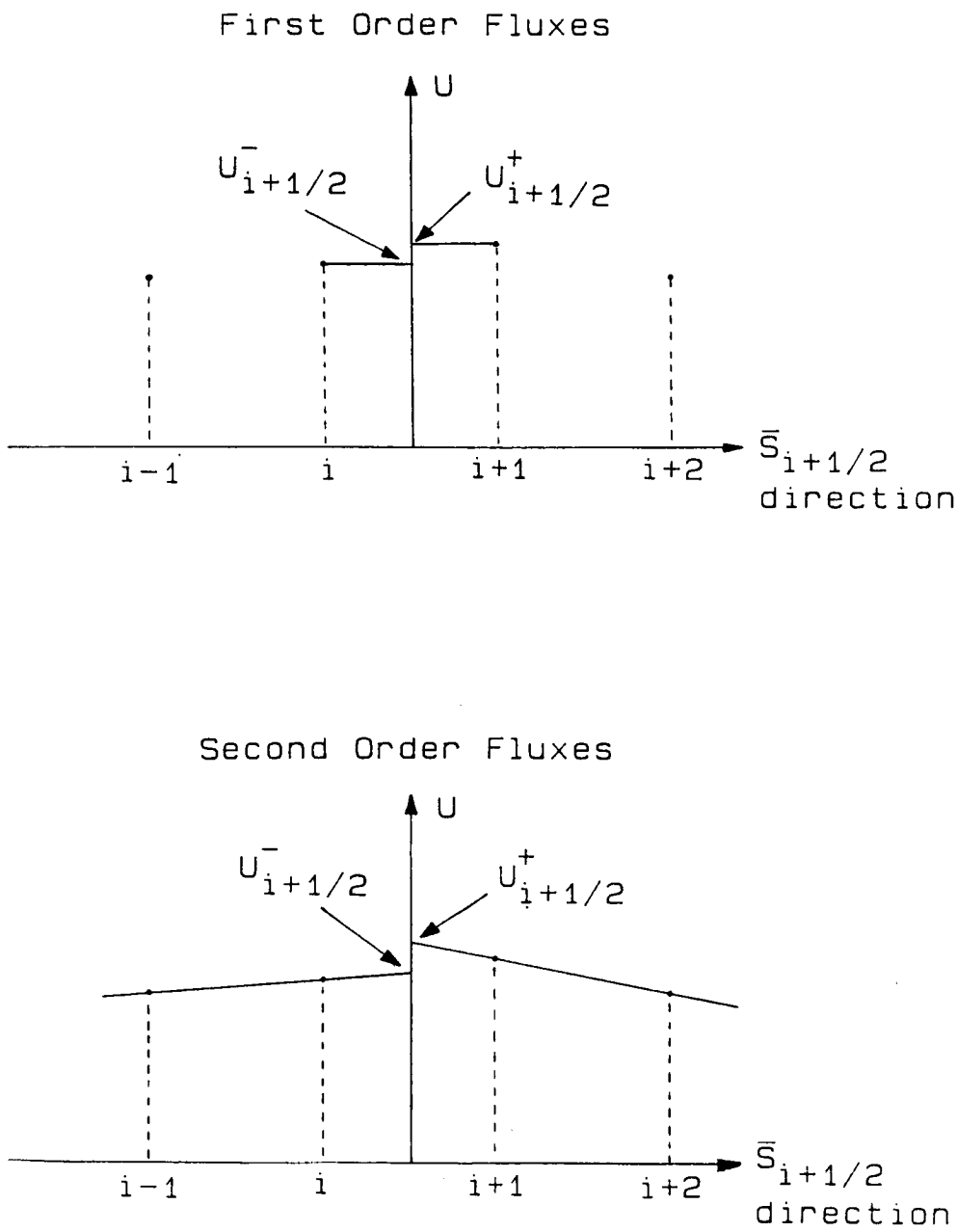

Figure 3.7 Extrapolations to the i+1/2 Surface for First- and Second-Order Flux Splitting.

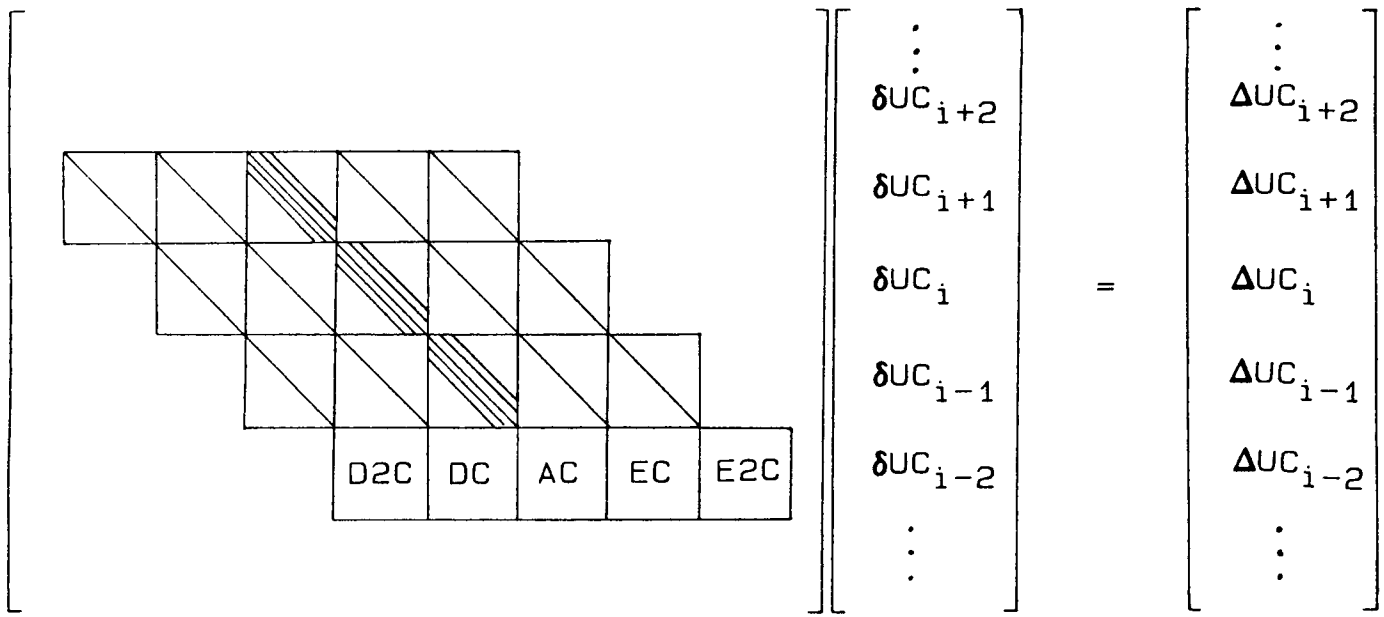

Figure 3.8a Arrangement of Linear System.

$$\delta UC_i = \begin{bmatrix} \cdot \\ \cdot \\ \cdot \\ \delta U_{i,\,j+1} \\ \delta U_{i,\,j} \\ \delta U_{i,\,j-1} \\ \cdot \\ \cdot \\ \cdot \end{bmatrix} \qquad \Delta UC_i = \begin{bmatrix} \cdot \\ \cdot \\ \cdot \\ \Delta U_{i,\,j+1} \\ \Delta U_{i,\,j} \\ \Delta U_{i,\,j-1} \\ \cdot \\ \cdot \\ \cdot \end{bmatrix}$$

Figure 3.8b Definitions for Figure 3.8a.

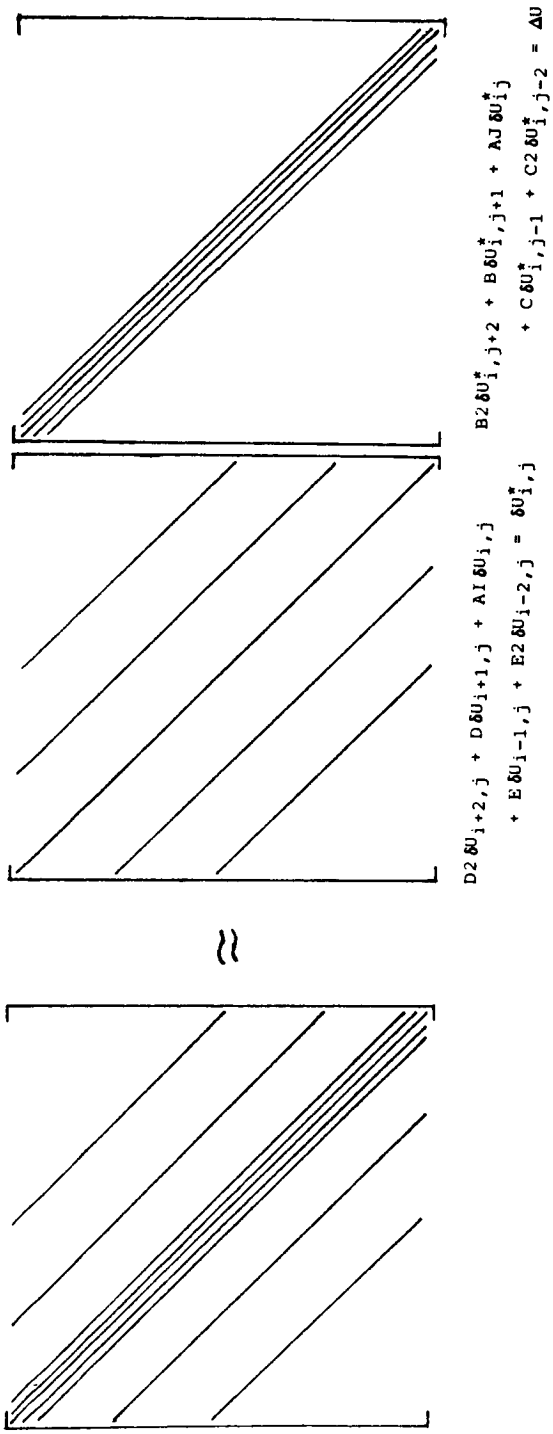

Figure 3.9 Approximate Factorization of Global Coefficient Matrix.

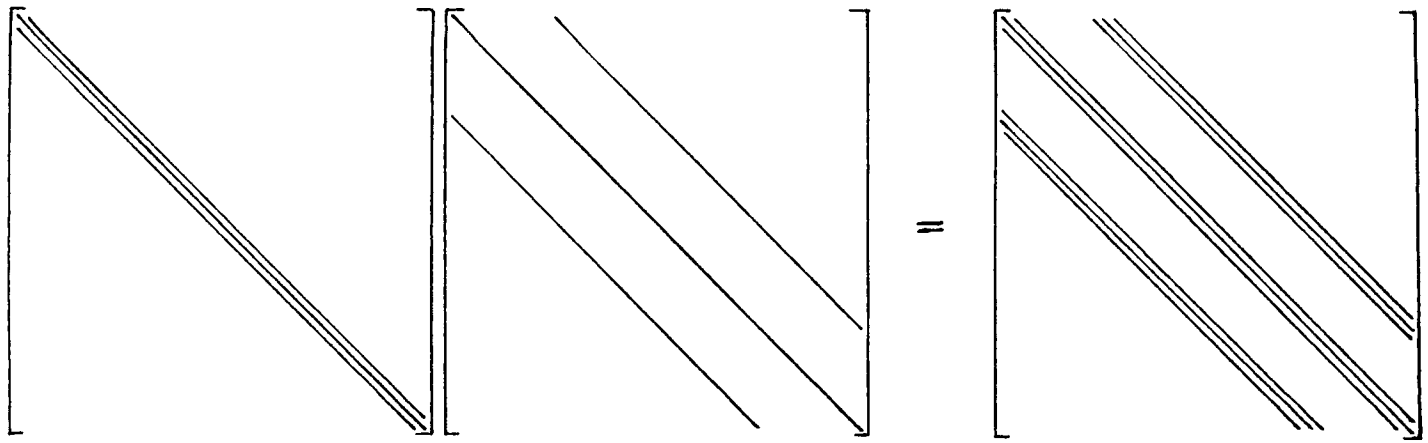

Figure 3.10 Error Due to Approximate Factorization.

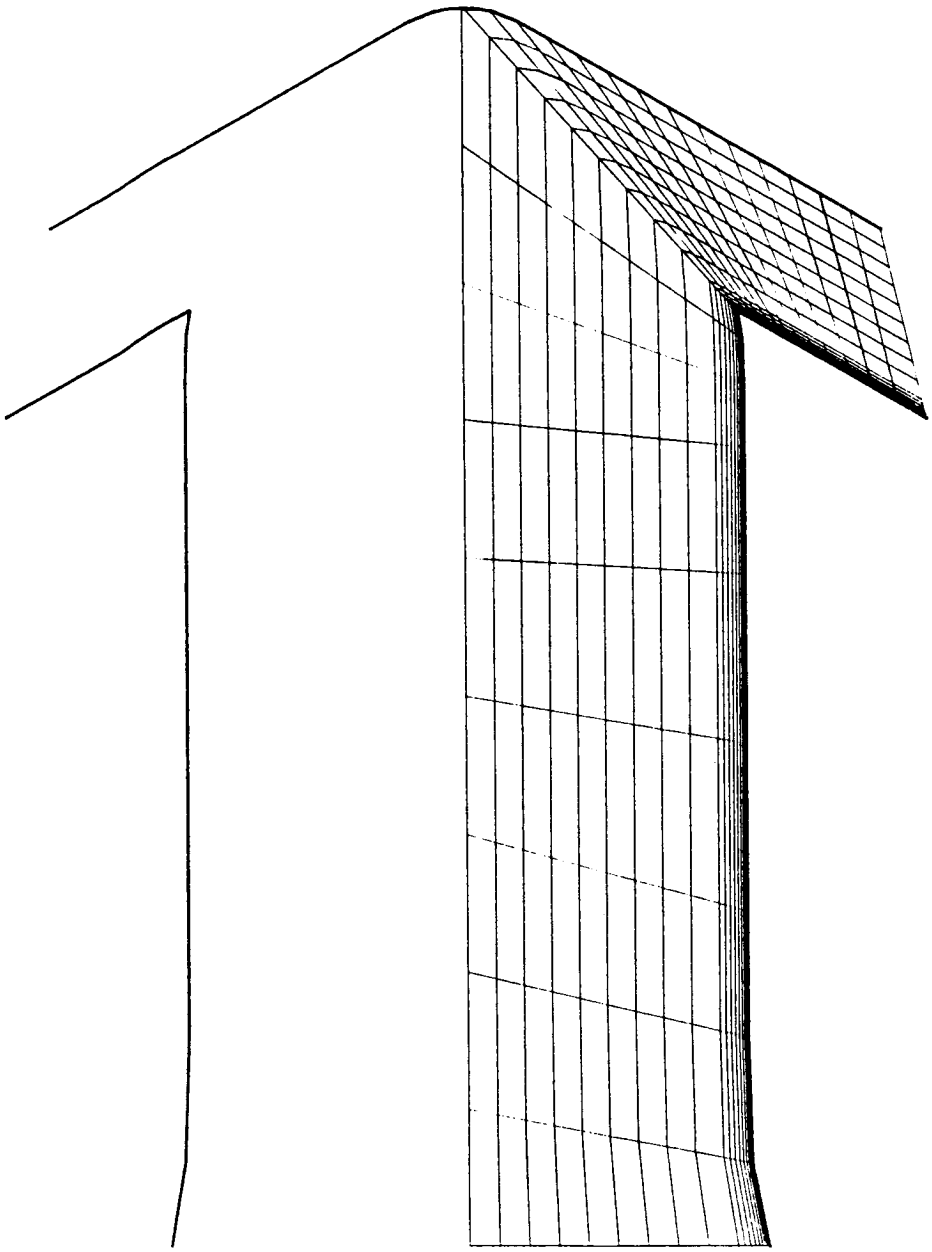

Figure 3.11 Mesh for Fully Deployed Nozzle.

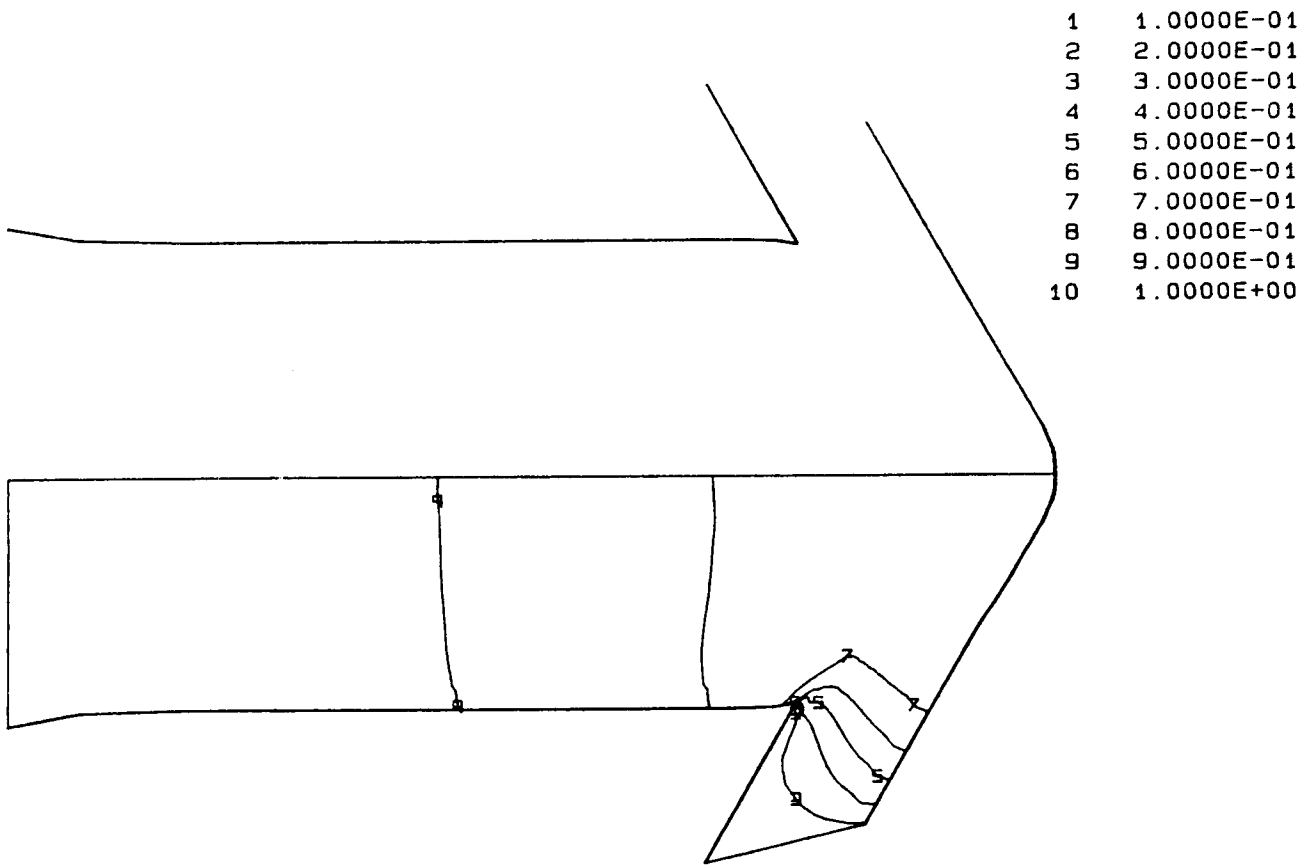

Figure 3.12 Pressure Contours During Initial Transients.

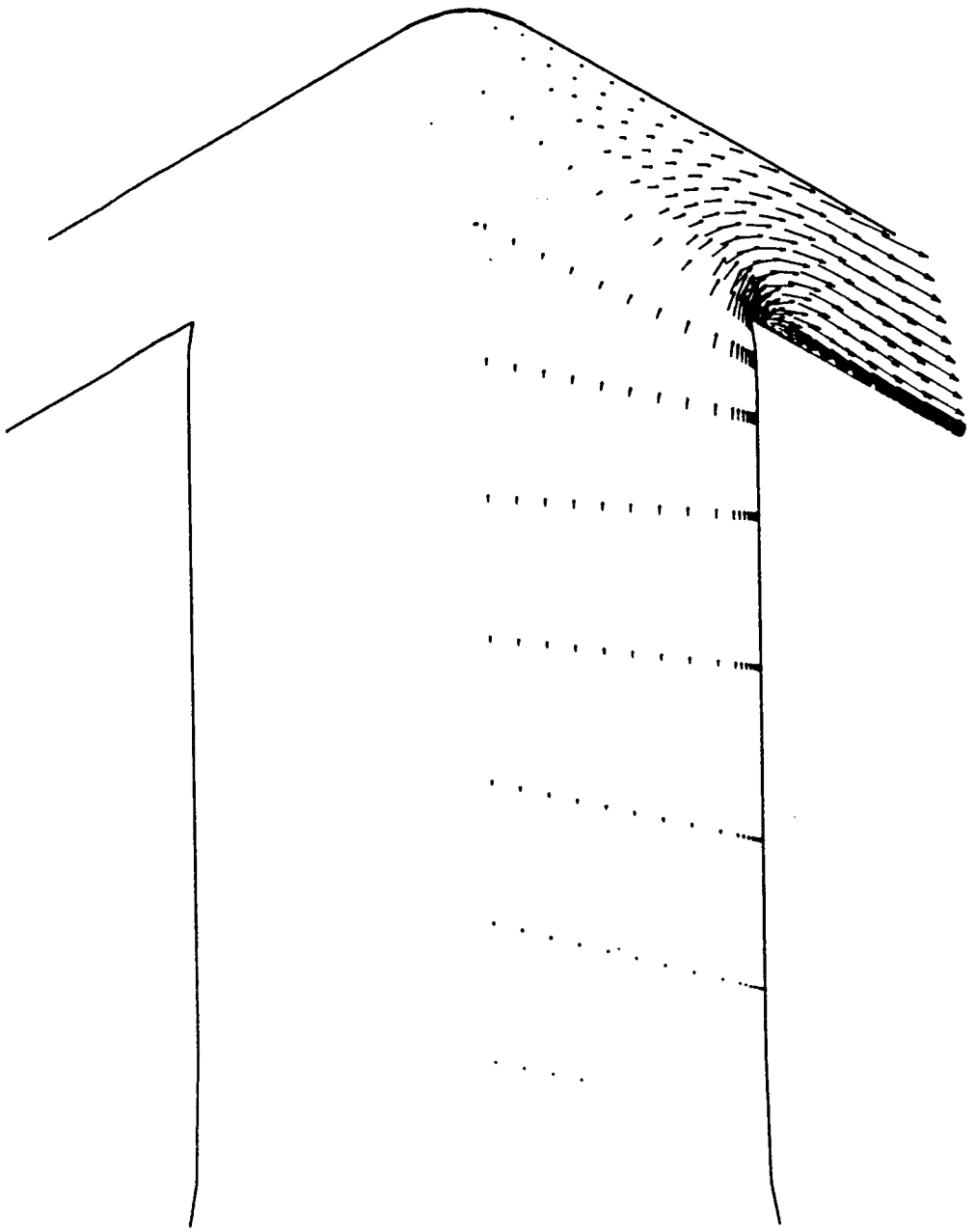

Figure 3.13 Velocity Vectors During Initial Transients.

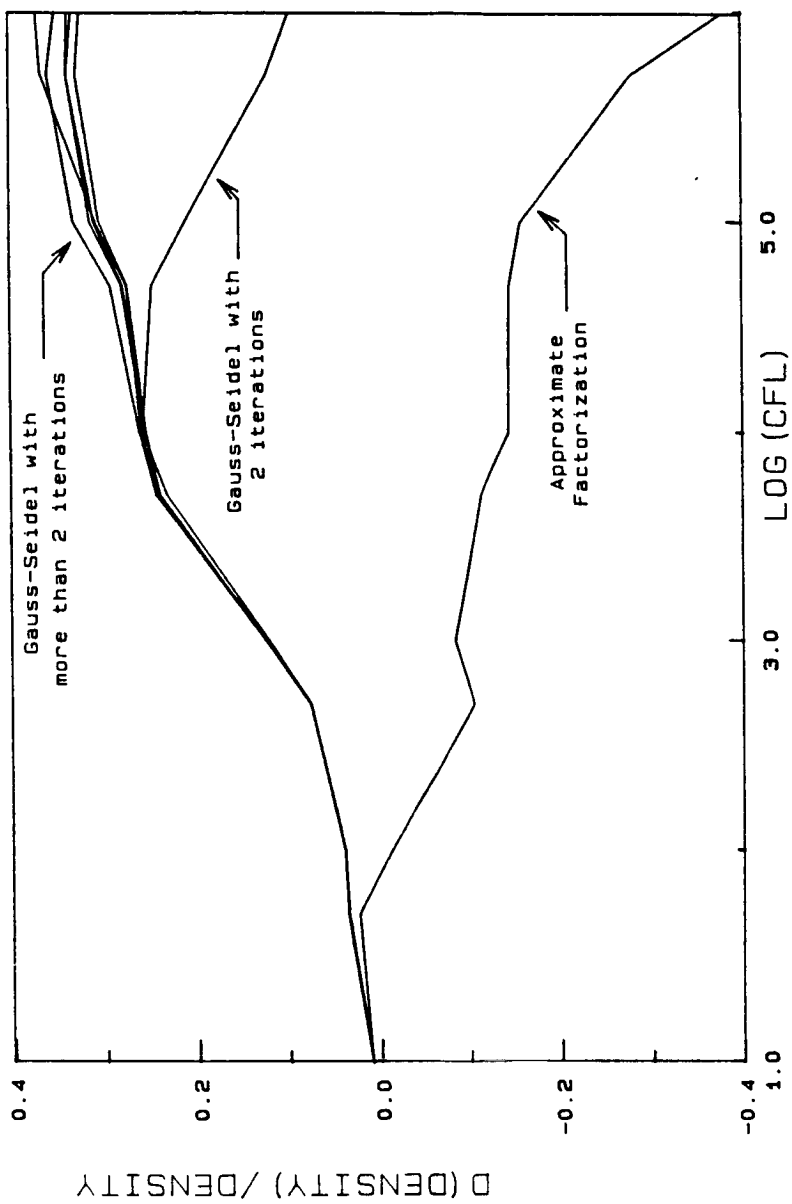

Figure 3.14 Normalized Time Difference of Density From Approximate Solutions of Linear System.

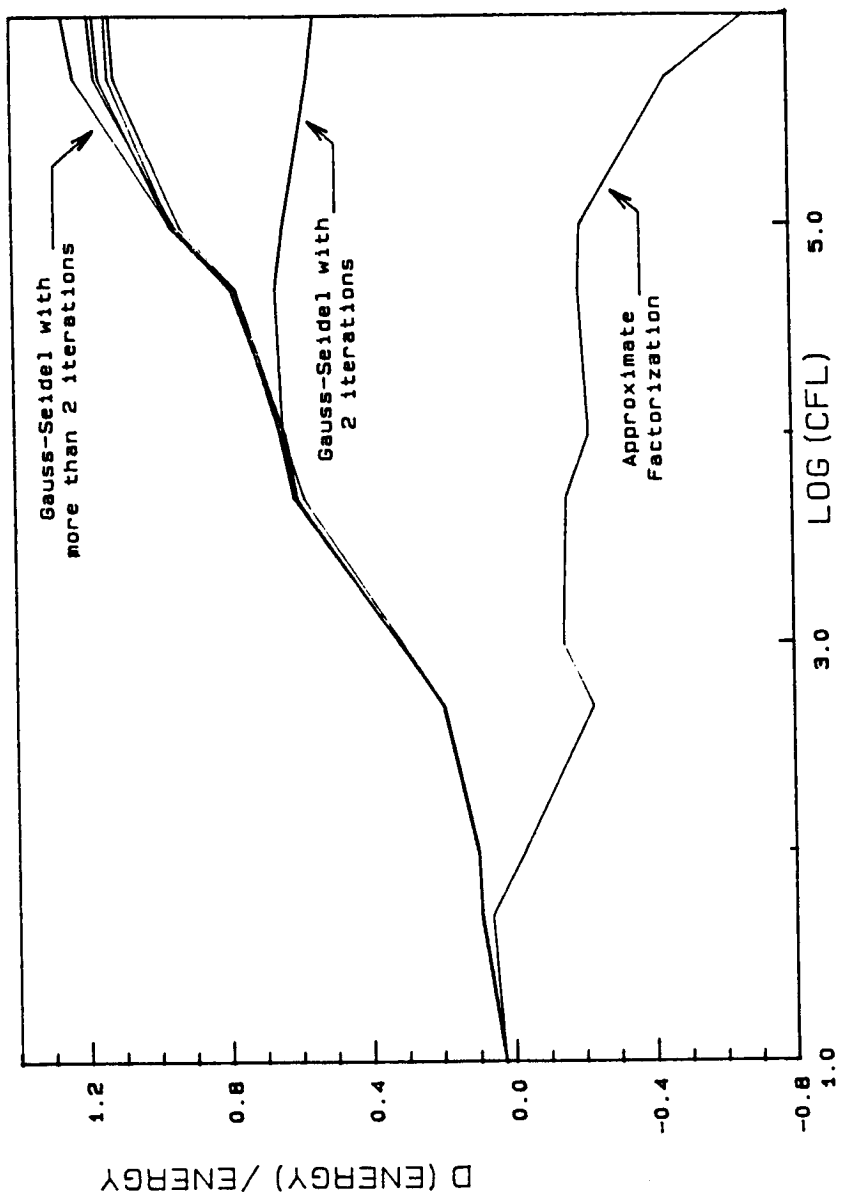

Figure 3.15 Normalized Time Difference of Energy from Approximate Solutions of Linear System.

CHAPTER 4

Results and Conclusions

I. Preliminary Comments

The computer program described in Chapter 3 has been applied to five thrust reversing nozzle configurations. The first configuration, described in Section II of this chapter, is a fully deployed thrust reversing nozzle with a flow turning angle of 130 degrees. The second configuration, described in Section III, is a 50% deployed thrust reversing nozzle. The third configuration, described in Section IV, is a 50% deployed thrust reversing nozzle with the forward thrust port vectored downward 15 degrees. The final two configurations are transient flow problems. In Section V, a calculation of a rapid change in thrust vectoring angle is described and in Section VI a calculation of a rapid change from partial to full thrust reverser deployment is described.

In Sections II through IV the computed results are compared with available experimental data. In all three cases the discharge coefficients and normalized thrusts are

compared. The discharge coefficient is the mass flow divided by the ideal mass flow and the thrust is normalized by the ideal thrust. Formulas for the ideal mass flow and ideal thrust are given in Appendix C.

II. Fully Deployed Thrust Reversing Nozzle

The first test case used during this investigation is the fully deployed thrust reverisng nozzle depicted in Figure 4.1. This configuration was choosen because considerable experimental data is available for it. Re and Leavit (Reference 1) have measured the variation of thrust and discharge coefficient with nozzle pressure ratio (NPR) and Putnam and Strong (Reference 3) have made wall static pressure measurements for a series of nozzle pressure ratios.

The internal flow field for this nozzle was calculated using first-order flux splitting for a range of nozzle pressure ratios from 2.0 to 7.0. The calculations were performed using the 32x27 single zone mesh in Figure 4.2. This mesh is divided into two regions for mesh generation purposes. The lower region is generated to keep the mesh nearly orthogonal to the wall. The mesh is refined along the flap and forward reverser port wall to resolve the boundary layer. No attempt has been made to resolve the boundary layer along the blocker. Since the boundary layer

along the blocker is embedded in a highly favorable pressure gradient it should be very thin and not significantly effect the flow.

A typical convergence history for these calculations is shown in Figure 4.3. This plot shows the variation of mass flow error with time step for a nozzle pressure ratio of three. The first-order accurate solution required 48 time steps to converge. The maximum CFL number for these calculations was set to 50,000 for the first four steps, 100,000 for the next four steps, and 150,000 for the forty remaining time steps.

The flow within this nozzle was also calculated for NPR=3.0 using second-order flux vector splitting and the mesh shown in Figure 4.4. The internal mesh is the same as that in Figure 4.2 and an external mesh was added to estimate the effect of the external flow. The second-order flux splitting is less robust than first-order flux splitting and the CFL number must be set lower. In this case the maximum CFL number was set to 2,000. Starting from a first-order solution 360 time steps were required to get a converged second-order solution.

The adequacy of the mesh refinement within the turbulent boundary layer is presented in Figure 4.5 for the second-order calculation with NPR=3.0. This plot gives the distribution of the law of the wall coordinate, y^+, for the

mesh points closest to the wall. The variable on the abscissa, I, is an index which varies from one at the inflow boundary, to 15 just before the sharp corner, to 31 at the outflow boundary. Baldwin and Lomax (Reference 7) state that a y^+ of less than two for the mesh point nearest the wall, is adequate to resolve the turbulent boundary layer. As shown in Figure 4.5, the y^+ for the mesh point nearest the wall is less than two everywhere except at the entrance and near the sharp corner. The y^+ at the entrance is close enough to two that the resolution should be sufficient. Near the corner the flow is rapidly accelerated and the boundary layer becomes very thin. In this case, the equilibrium assumption inherent in the Baldwin Lomax model is questionable. In any case this region is very small (two points with y^+ significantly greater than two) and it is not likely to adversely affect the flow. Overall, the mesh refinement near the wall is considered adequate.

Pressure contours in the region of the exit port for nozzle pressure ratios of three, and five are given in Figures 4.6 and 4.7, respectively. The pressures, obtained using the first-order method, are normalized by their respective specified stagnation pressures and all cases had the same exit pressure.

The pressure contours, obtained from the second-order method for a nozzle pressure ratio of three, are shown in

Figure 4.8. In all three figures the high gradients near the corner are evident. The second-order contours, Figure 4.8, are nearly the same as the first-order contours (Figure 4.6) for pressures greater than half the stagnation pressure. However, there are considerable differences along the forward wall of the reverser port with the second-order method giving lower pressures than the first-order method.

Mach number contours in the region of the exit port for nozzle pressure ratios of three and five are given in Figures 4.9 and 4.10, respectively. Note that the NPR=3.0 case has a small region of supersonic flow near the exit, and the NPR=5.0 case has a much larger region of supersonic flow in the reverser port. The Mach number contours, obtained from the second-order method with NPR=3.0, are shown in Figure 4.11. The second-order method yields higher Mach numbers than the first-order method (Figure 4.9). It also appears that the boundary layer separation bubble, on the forward wall of the reverser port, is larger in the second-order case than the first-order case.

Velocity vectors are also given in the region of the exit port. Figure 4.12a shows the velocity vectors for NPR=3.0. A thin layer of separation is evident on the forward wall of the reverser port. This separation is shown more clearly in Figure 4.12b. Figures 4.13a and 4.13b show the velocity vectors for NPR=5.0. The separation region is

smaller than that calculated for NPR=3.Ø. For comparison, the velocity vectors, obtained from the second-order method with NPR=3.Ø, are shown in Figure 4.14a and 4.14b. The boundary layer separation obtained from the second-order method, Figure 4.14b, is more extensive than that obtained from the first-order method, Figure 4.12b. In the first-order solution the separation covers 31 percent of the forward wall of the reverser port wall and in the second-order case it covers 45 percent of the wall.

The calculated variation of discharge coefficient with nozzle pressure ratio is given in Figure 4.15. Also shown are the discharge coefficients obtained experimentally by Re and Leavit (Reference 1). It is seen that the analysis overestimates the discharge coefficient by two to four percent. This is to be expected since the effect of the sidewall boundary layers is neglected. The side wall boundary layers will reduce the effective throat area and hence the mass flow. Also shown in Figure 4.15 is the second-order calculation at NPR=3.Ø (single point). The discharge coefficient from the second- order calculation is slightly higher than from the first- order method. The comparison with the experimental is good for discharge coefficient.

The calculated variation of thrust with nozzle pressure ratio is compared with the experimental results of Re and

Leavitt in Figure 4.16. The first-order results indicate a lower amount of reverse thrust than the experimental results with errors ranging from twenty-nine percent of the ideal thrust at NPR = 2.0 to eleven percent at NPR = 7.0. Also shown in Figure 4.16 is the thrust obtained from the second-order method. This thrust compares better with experiment, the error being 14.6 percent of the gross thrust compared to a 22.0 percent error from the first-order method.

The errors in thrust warrant some discussion. The error is related to the size of the separation bubble calculated on the forward wall of the reverser port. In the calculations the size of the separation bubble seems to be underestimated and the pressure on this surface is overestimated. This hypothesis is substantiated in part by the improved results obtained from the second-order method. As mentioned earlier, the separation bubble is larger in the second-order results than in the first-order results. This hypothesis is also supported by the pressure field within the nozzle.

Figures 4.17 through 4.19 compare the calculated pressure field with sidewall pressures measured by Putnam and Strong for NPR=3.0. All three figures are for lines, parallel to the blocker wall, passing from the plane of symmetry to the exit plane. The line for Figure 4.17 is 0.203 cm from the blocker wall. At this location the

pressures calculated with the second-order method compare very well with the measured sidewall pressures. The pressures calculated with the first-order method also compare well with the experimental results, but not as well as the second-order results. Since this line is close to the blocker it is an indication that the blocker pressure distribution is accurately predicted. Since the contribution to the thrust from a surface is approximately the integral of the pressure over the surface area, the contribution to the thrust from the blocker is also accurately predicted.

The line for Figure 4.18 is 0.838 cm from the blocker wall, or approximately half way to the forward wall of the reverser port. Again both first-order and second-order solutions compare well with the experimental results over most of the line. However, the calculated and experimental results differ considerably within the exit port.

The line for Figure 4.19 is 1.437 cm from the blocker wall, or nearly to the forward wall of the reverser port. Here the sharp corner is identified by the rapid drop in pressure. Both the first- and second-order results do well up to the corner, but smear out the expansion and miss the minimum pressure. The second-order solution is better than the first-order solution, missing the minimum pressure by 12 percent of the stagnation pressure as opposed to a 20

percent discrepancy with the first-order solution.

The final comparison, Figure 4.20, of calculated pressures with experiment is for pressures along the flap, rounding the sharp corner, and down the forward wall of the reverser port. These pressures are plotted in terms of the arclength along the wall from the inflow boundary. The experimental results from four lateral stations are also plotted. Note that there is considerable variation amongst the experimental results, particularly near the exit plane. This variation indicates the magnitude of the three dimensional effects. It is interesting to note that two pressure distributions, both lying within the range of experimental pressures presented in Figure 4.20, can yield thrusts varying by up to six percent of the ideal thrust. The most that can be expected of a two-dimensional solution is for it to be within this range.

Unfortunately, the calculated pressures do not lie within the range of pressures measured by Putnam and Strong (Reference 3). Both the first- and second-order calculations do well before the sharp corner, but predict a recompression along the forward wall of the reverser port before it is indicated by the experiment results. Thus, both the first- and second-order calculations overestimate the pressure, and hence force, on the forward wall of the reverser port. This accounts for the low calculated reverse

thrust compared to the thrust obtained by Re and Leavitt (Reference 1). It should be noted that the second-order results are considerably better than the first-order results. This indicates that the discrepancy between calculation and experiment is, in part, due to numerical dissipation. The amount of numerical dissipation present in a calculation depends on the refinement of the mesh and the skewness of the grid, as well as the order and type of method used. A coarser or more highly skewed mesh has greater numerical dissipation than a finer or nearly orthogonal mesh. Unfortunately, the complex geometries considered force some degree of skewness to the mesh. The refinement, however, is controlled by the user. To obtain an accurate solution all features of the flow must be resolved. Examination of the velocity vectors in Figure 4.14b shows that the shear layer at the edge of the separation bubble is in a region of coarse mesh. Refining the mesh in this region should substantially reduce the amount of numerical dissipation in this region, and improve the solution. Unfortunately, this calculation was not possible due to limited computer resources.

Another item which might contribute to the error in the pressure distribution along the forward wall of the reverser port is the forward wall of the reverser port in the turbulence model. An overestimation of the eddy viscosity

could reduce the size of the separation bubble and cause the early recompression seen in Figure 4.20. The Baldwin Lomax turbulence model, described in Section III of Chapter 1, has been shown to yield satisfactory results for some separated flows (Reference 7) but has never been tested on a problem as complex as the thrust reversing nozzle.

Finally, the flow does have significant three-dimensional effects as mentioned earlier. The spanwise variations in flap pressure distributions (Figure 4.20) are probably due to large scale vortices present in the reverser port. How these vortices interact with the boundary layer separation is not clear. It is possible that the separation bubble is enlarged by the vortices. If this is the case an accurate prediction of thrust for this geometry can never be obtained from a two-dimensional calculation. In any case, the two-dimensional calculation does provide good quantitative results for the discharge coefficient and reasonable qualitative results for the thrust.

III. Partially Deployed Thrust Reversing Nozzle

The second test case is the partially deployed thrust reversing nozzle shown in Figure 4.21. This nozzle geometry, tested by Carson, et.al. (Reference 2), is based on a realistic multifunction nozzle design presented by Stevens, Thayer, and Fullerton (Reference 13). The

experimental results include discharge coefficients and thrust for a range of nozzle pressure ratio and ambient external Mach number. A calculation is presented for this nozzle with a nozzle pressure ratio of two and an ambient external Mach number of zero.

The calculation was performed using the mesh shown in Figure 4.21. Due to limited computer resources, this mesh is very coarse and none of the wall boundary layers are adaquately resolved.

The resulting discharge coefficient is .89 compared to .993 from the experiment of Carson, et.al. There is evidence that the mesh is inadaquate for accurately calculating the mass flow. The problem was run to convergence using the first-order accurate results and then switched to second-order accuracy. The first-order result for discharge coefficient is only .78 compared to .89 from second-order accuracy. If the mesh were sufficiently fine the difference would be less dramatic.

It should be noted that the areas of the reverser ports for the model tested by Carson, et.al. are somewhat larger than for the nozzle used in the calculation. the combined areas of the three exit ports in the experiment were 36.11 cm^2 as opposed to 34.89cm^2 for the calculation (based on two nozzles, each with a width of 7.77 cm). Carson, et.al. based their ideal mass flow calculation on the throat area

of the baseline forward thrust nozzle, 34.24 cm^2. Correcting the calculated discharge coefficient (by simply multiplying by the ratio of areas) yields a discharge coefficient of Ø.92.

The calculated thrust is found to be slightly higher than the measured thrust. The calculated thrust, normalized by the ideal thrust based on the measured mass flow, is Ø.253, whereas the measured thrust, normalized by the ideal thrust based on the measured mass flow, is Ø.23. This comparison is suprisingly good considering the coarseness of the mesh.

The pressure contours, Mach number contours, and velocity vectors for this nozzle are given in Figures 4.22 through 4.24. It is clear from Figure 4.23 that the flow remains subsonic until it leaves the exit port. Thus, the internal flow is influenced by the external flow and the external zone is needed.

IV. Partially Deployed Thrust Reversing Nozzle with Vectoring

The third test case, shown in Figure 4.25, is the same 50% deployed thrust reversing nozzle discussd in Section III with the forward thrust port vectored 15° downward. This nozzle was also tested by Carson, et.al., and the discharge coefficient and thrust were obtained for a range of nozzle

pressure ratios and two free stream Mach numbers. The calculation was made at a nozzle pressure ratio of two with an ambient free stream Mach number of zero.

As with the unvectored case the calculation was performed using a coarse mesh. The mesh is composed of four zones: three internal zones and an external zone. The dimensions of the mesh for all three internal zones is 21x1Ø. For the external zone the mesh dimensions are 17x1Ø7.

The calculation was run to convergence first order accurate (64 time steps). The resulting discharge coefficient is Ø.77, which is consistent with the results for the unvectored case. The calculated thrust, normalized by the ideal thrust, is Ø.146 and the normal force, normalized by the ideal thrust is Ø.Ø65 Note that the ideal thrust is based on the measured mass flow (Appendix C).

The thrust and normal force normalized by the ideal thrust based on the calculated mass flow are Ø.19 and Ø.Ø85.

The experimental results for this case had considerable asymmetry. The thrust was measured for vectoring of 15^{o} both upward and downward. With nozzle flow vectored downward the normalized thrust was Ø.18 whereas it was Ø.34 when vectored upward. The computed normalized thrust is at the lower end of this range. Likewise, the computed jet turning angle of 24^{o} lies between the experimental results

of -5° and 45°.

The calculated pressure contours, Mach number contours, and velocity vectors for this case are shown in Figures 4.26 through 4.28. It appears, from the Mach contours in Figure 4.27 that there is no supersonic flow. The results for the unvectored nozzle, however, indicate small regions of supersonic flow just outside each exit port when second-order accuracy is used. It appears that the first-order accuracy, in combination with the coarse mesh, has resulted in excessive total pressure loss. This seems to be the reason for the low discharge coefficient. If this calculation was done using second-order accuracy, or the mesh was refined, the calculated discharge coefficient would be much closer to the measured discharge coefficient.

V. Transient Change in Thrust Vectoring Angle

A calculation was made of a transient change in thrust vectoring angle. The nozzle was initially unvectored and the vectoring angle was changed from 0° to 30° over a period of .3 msec. The actual wall velocity followed a cosine function of time with the maximum velocity being nearly half the speed of sound. This very fast change was necessary for transient effects to be observed. The initial solution is shown in Figures 4.29 through 4.31. The mesh uses three internal zones with the lower and upper zones having

dimensions 23x16 and the middle zone having dimensions 23x8. The nozzle pressure ratio is 5.0.

The effects of the moving wall are seen by comparing the pressure contours during the final stages of the reconfiguration, Figure 4.34, with the pressure contours after the reconfiguration is complete, Figure 4.37. The 0.2 contour in Figure 4.34 extends from the exit of the rear port half the distance to the corner. In Figure 4.37 this contour has relaxed so that it connects to the wall near the exit port and intersects the exit plane at a higher position. No experimental data is available for this case.

VI. Transient Change in Thrust Reverser Deployment

A calculation was made of a transient change in degree of thrust reverser deployment. The nozzle was initially 70 percent deployed with the rear port width being 0.05 ft. The rear port was then closed, as the reverser ports were opened, over a period of .3 msec.

The results, shown in Figures 4.38 through 4.46, indicate much more dramatic transient affects than the transient thrust vectoring case. As shown in the pressure contours, (Figure 4.43) the closing rear port compresses the air near the port to much greater than the stagnation pressure at the inflow boundary. As the port closes the pressure becomes large enough that the flow near the

entrance to the port reverses direction and the air flows back into the nozzle as shown in Figures 4.42a and 4.42b. There is no experimental data available for this case.

VII. Conclusions

An implicit finite volume program has been developed for the calculation of two-dimensional thrust reversing nozzle flows. Thrust reversing nozzles typically have sharp corners, and the rapid expansion and large turning angles near these corners lead to unacceptable time step limitations when conventional approximate factorization methods are used. In this investigation these limitations are overcome by replacing the approximate factorization with a line Gauss-Seidel relaxation. This method is implemented with a zonal mesh so that flows through complex nozzle geometries can be efficiently calculated.

Results are presented from calculations using both first- and second-order fully upwind differencing. In most cases, the second-order method compared better with the experimental results than the first-order method. The second-order method was limitted, by stability, to lower CFL numbers than the first-order method. The lower CFL numbers resulted in longer run times for the second-order method. (Typically, 360 time steps for the second-order method compared to 48 time steps for the first-order method).

Despite this limitation, the second-order method still requires two to three orders of magnitude fewer time steps than an explicit method when turbulent boundary layers are adequately resolved.

The comparisons of the calculated results with experiment were mixed. For the fully deployed nozzle (Section II of this chapter) the calculated discharge coefficient compared well with experiment but the amount of reverse thrust was underestimated. Conversely, for the two partially deployed nozzles (Sections III and IV) the calculated thrust compares well with experiment but the discharge coefficient is underestimated. The underestimation of the discharge coefficient for the partially deployed nozzles is undoubtably due to the coarse mesh used for the calculation. The underestimation of the reverse thrust for the fully deployed nozzle is thought to be caused by a combination of insufficient mesh density, limitations of the turbulence model, and three-dimensional effects in the experiment which cannot be predicted with a two-dimensional model (see Section II of this chapter).

The computer program is robust, efficient, and capable of calculating the complex flows within thrust reversing nozzles.

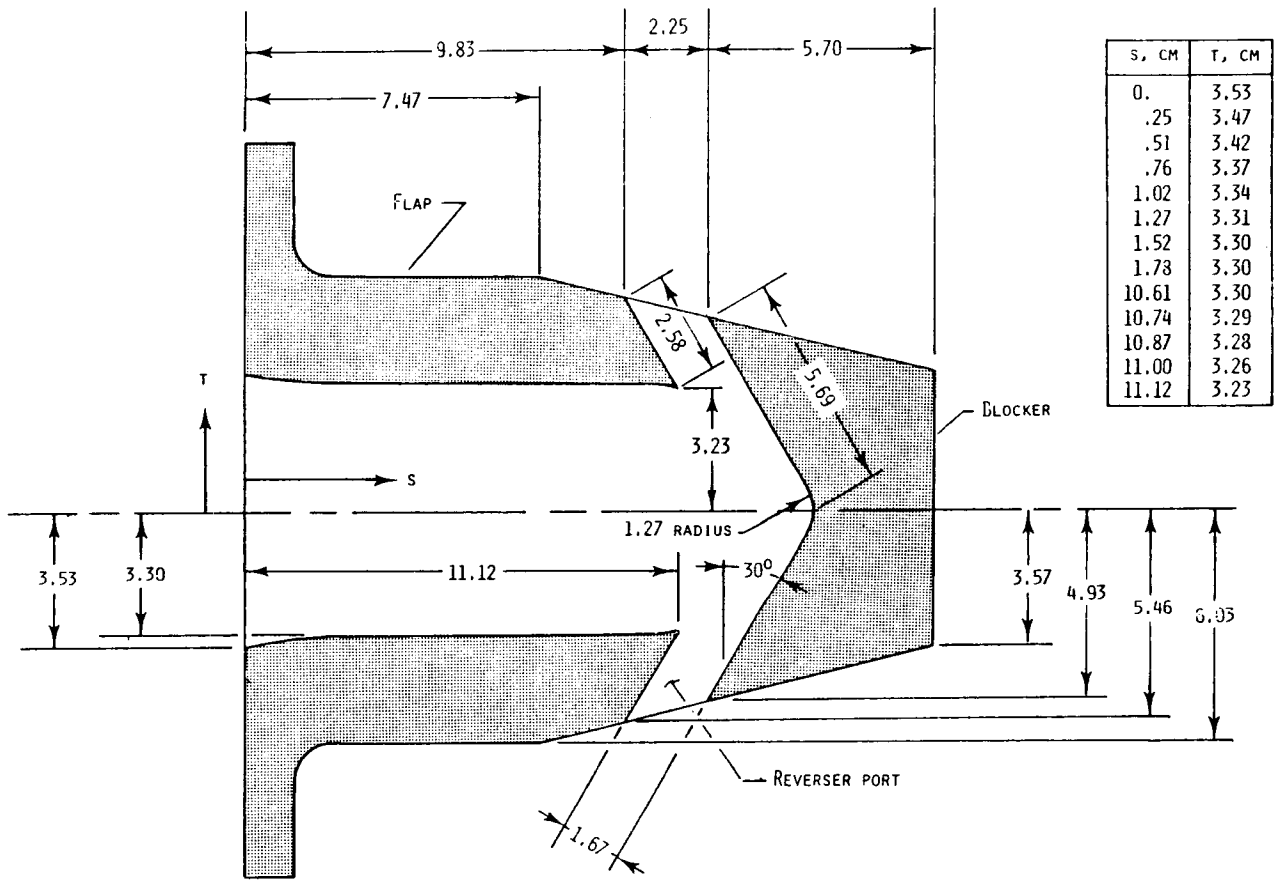

S, CM	T, CM
0.	3.53
.25	3.47
.51	3.42
.76	3.37
1.02	3.34
1.27	3.31
1.52	3.30
1.78	3.30
10.61	3.30
10.74	3.29
10.87	3.28
11.00	3.26
11.12	3.23

Figure 4.1 Details of 2-D Convergent-Divergent Thrust-Reversing Nozzle. Internal width of nozzle is 10.160 cm. All Dimensions are in centimeters unless otherwise noted.

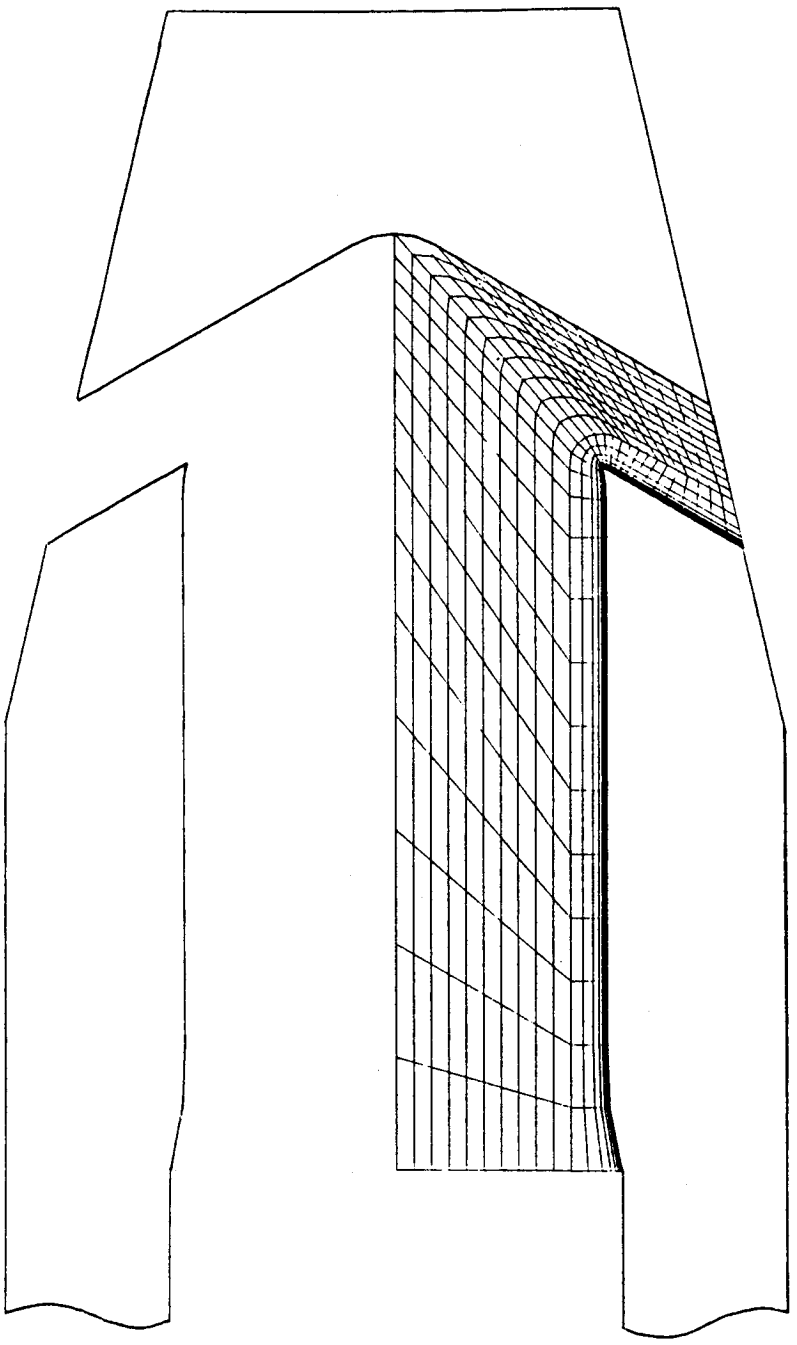

Figure 4.2 Mesh for Fully Deployed Thrust Reversing Nozzle. Interior Flow Calculation - 32x27 Cells.

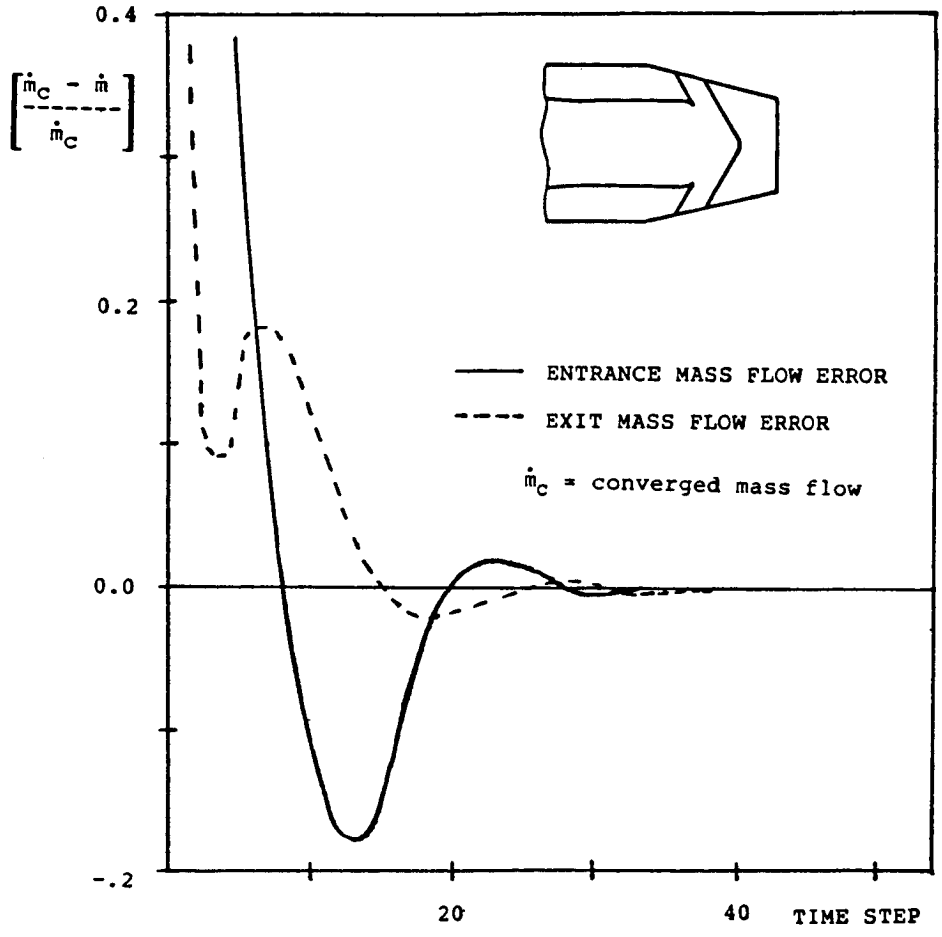

Figure 4.3 Mass Flow Convergence History for the Fully Deployed Thrust Reversing Nozzle.

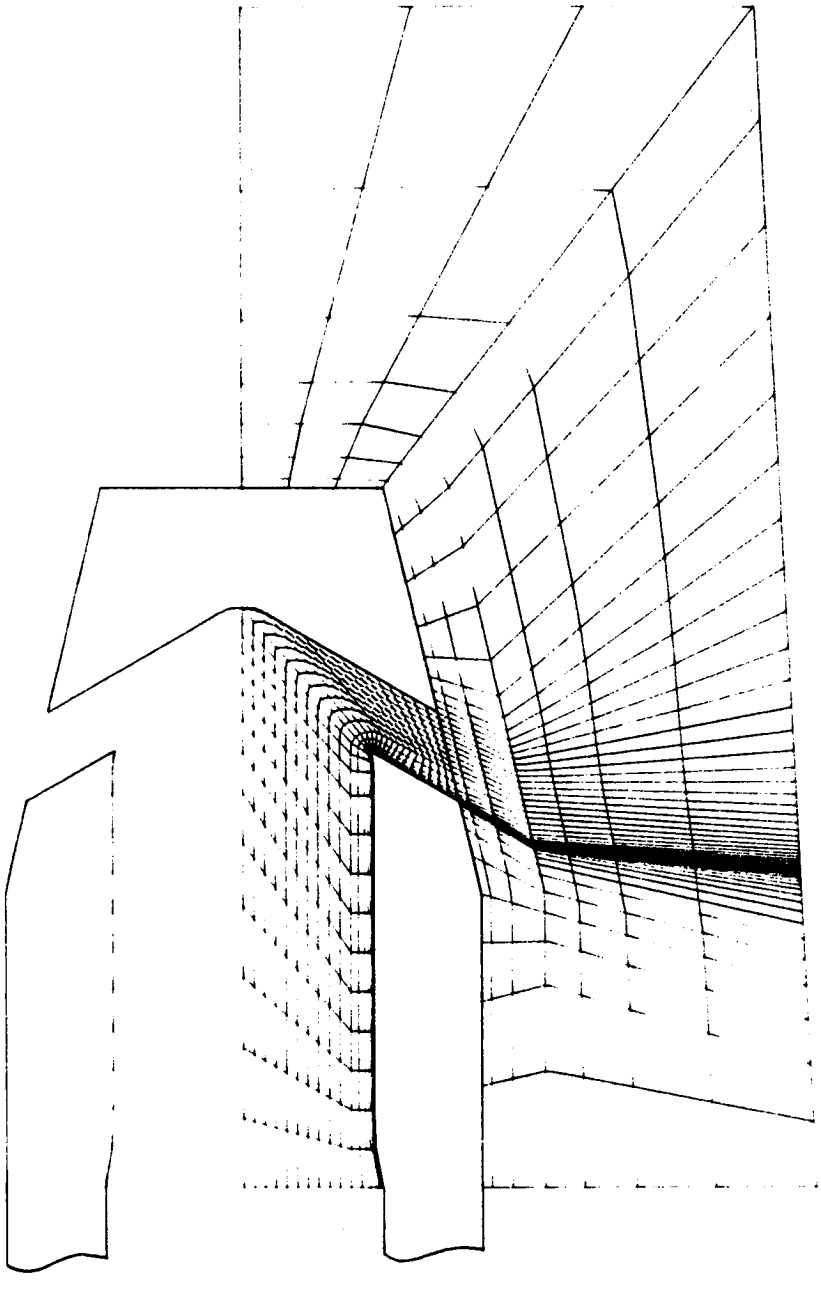

Figure 4.4 Mesh for Fully Deployed Thrust Reversing Nozzle
32x27 Internal Mesh - 9x56 External Mesh

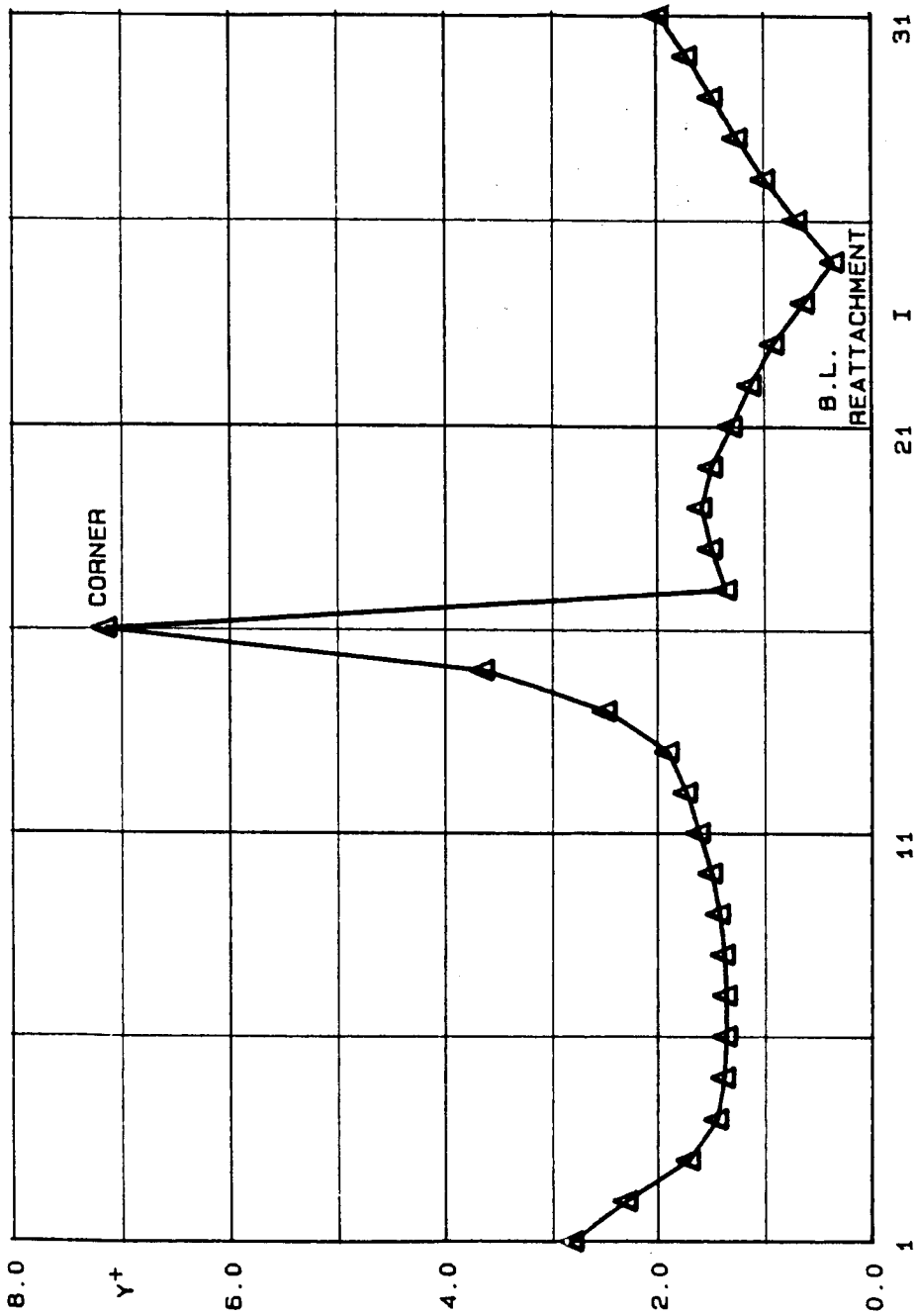

Figure 4.5 Evaluation of Grid Refinement Along Flap. Y^+ Distribution for Cells Nearest Wall.

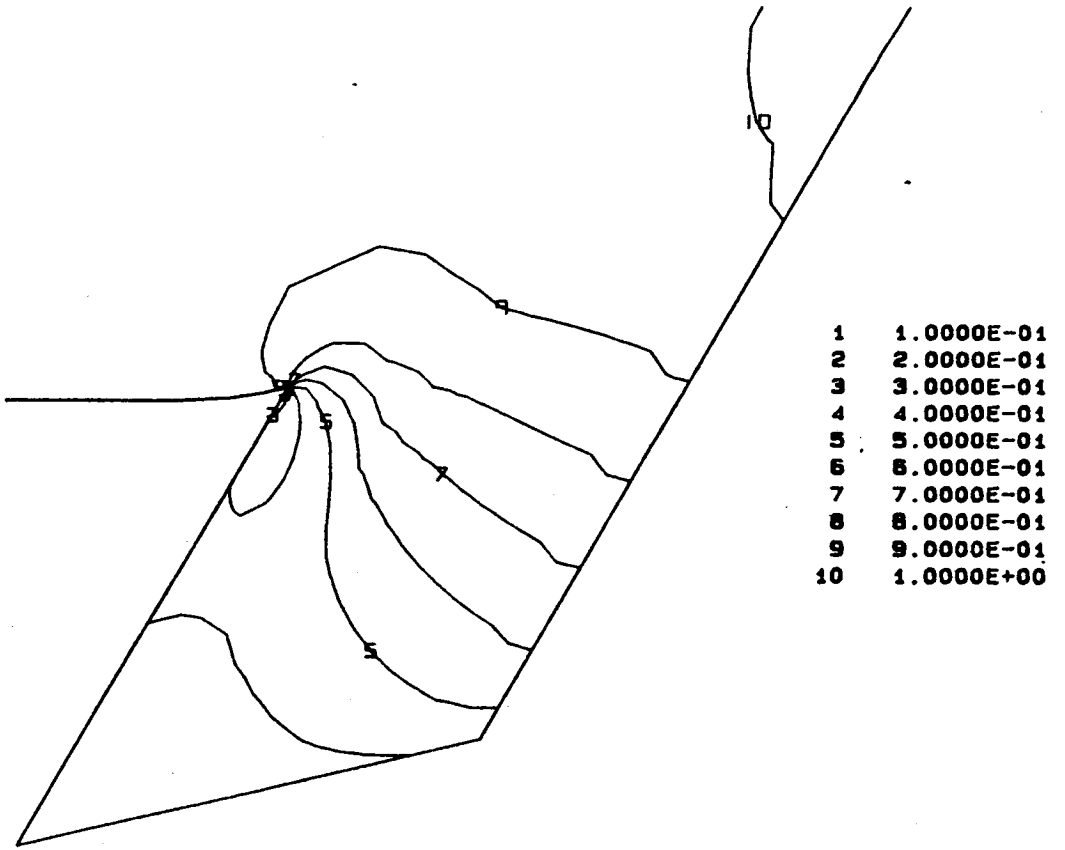

Figure 4.6 Pressure Contours for Fully Deployed Thrust Reversing Nozzle - NPR = 3.0 - 32x27 Mesh - First-Order.

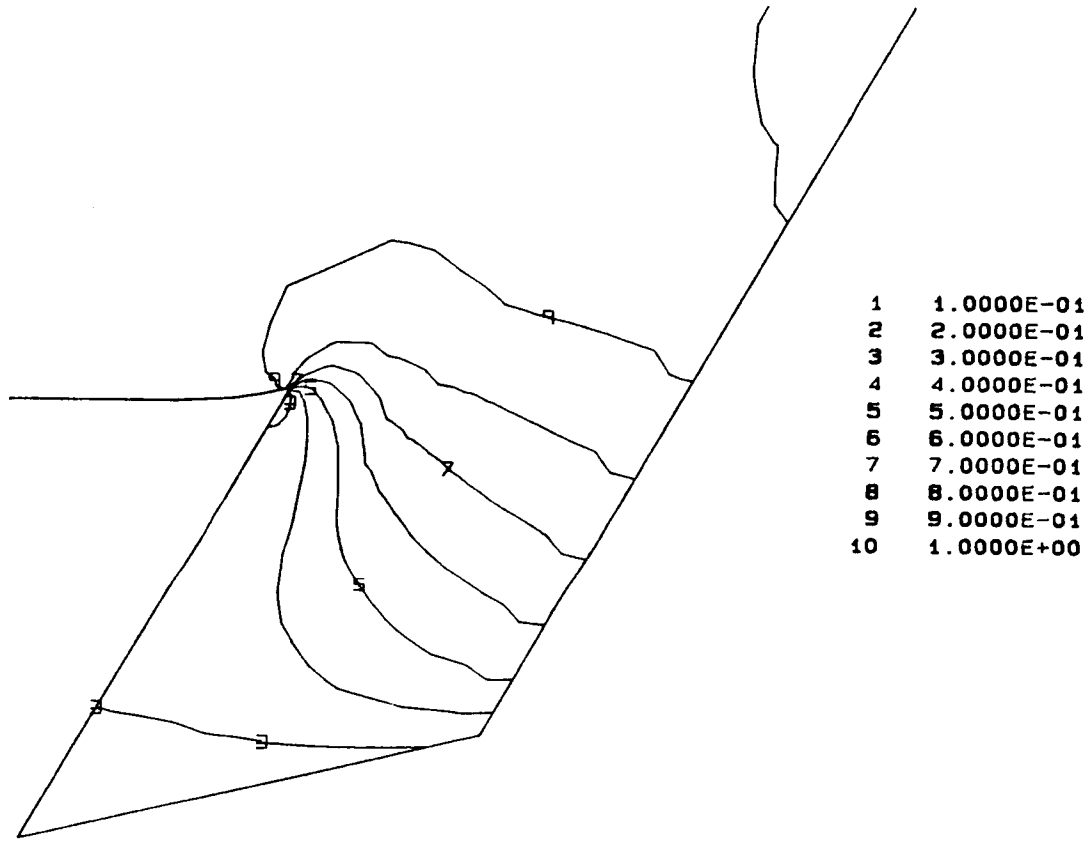

Figure 4.7 Pressure Contours for Fully Deployed Thrust Reversing Nozzle - NPR = 5.0 32x27 Mesh - First-Order.

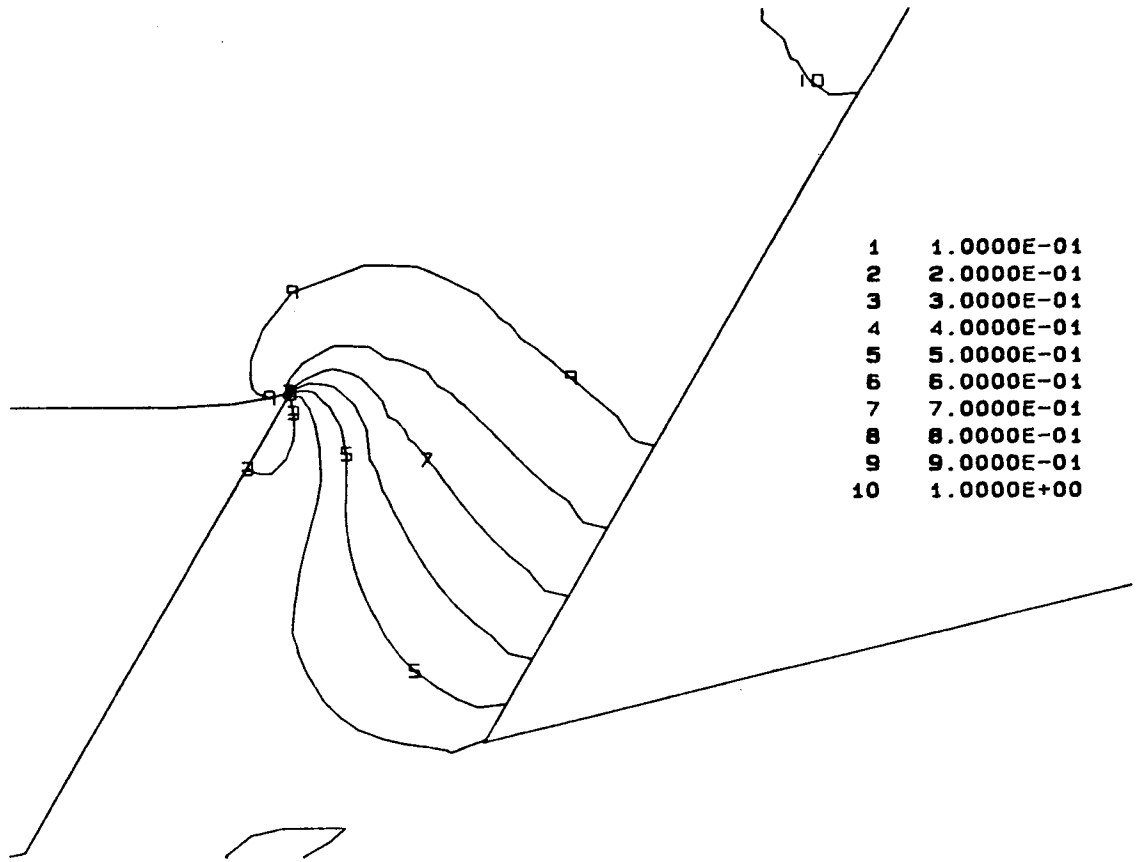

Figure 4.8 Pressure Contours for Fully Deployed Thrust Reversing Nozzle - NPR = 3.0 - 32x27 Mesh - Second-Order.

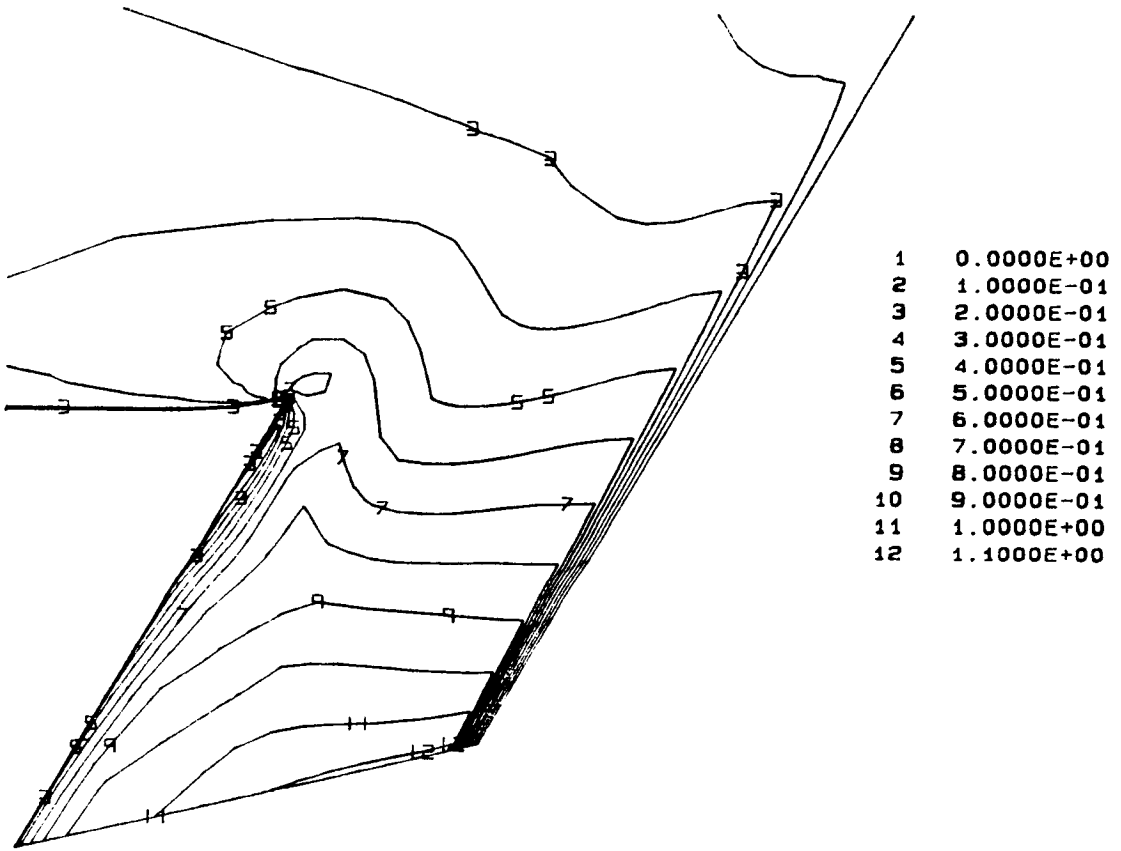

Figure 4.9 Mach Number Contours for Fully Deployed Thrust Reversing Nozzle - NPR = 3.0 - 32x27 Mesh - First-Order.

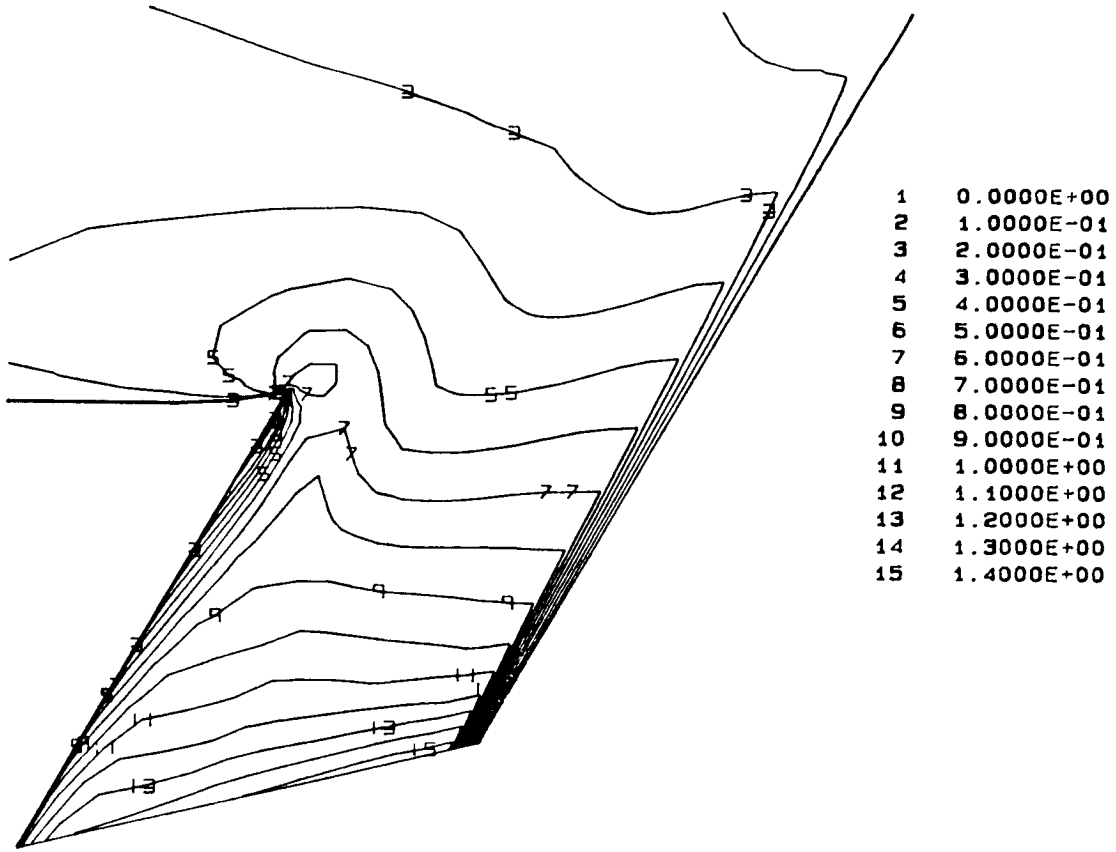

Figure 4.10 Mach Number Contours for Fully Deployed Thrust Reversing Nozzle - NPR = 5.0 - 32x27 Mesh - First-Order.

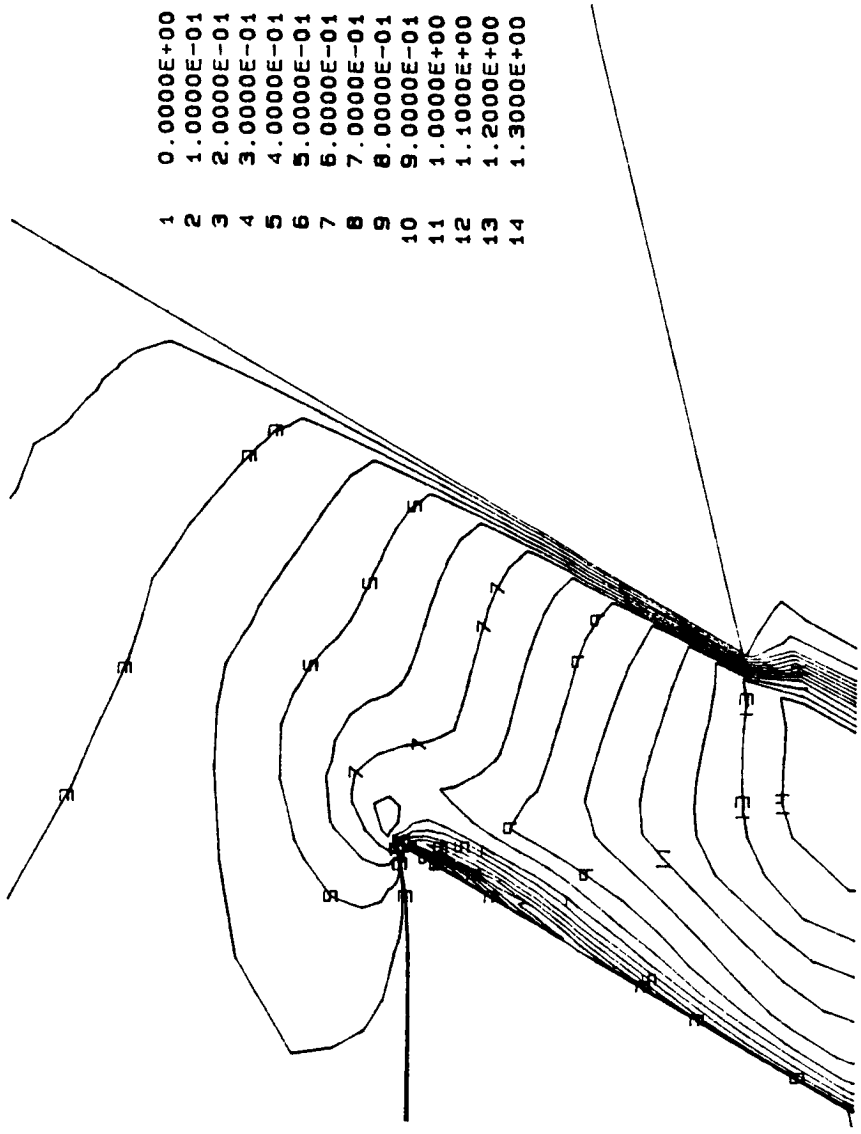

Figure 4.11 Mach Number Contours for Fully Deployed Thrust Reversing Nozzle - NPR = 3.0 - 32x27 Mesh - Second-Order.

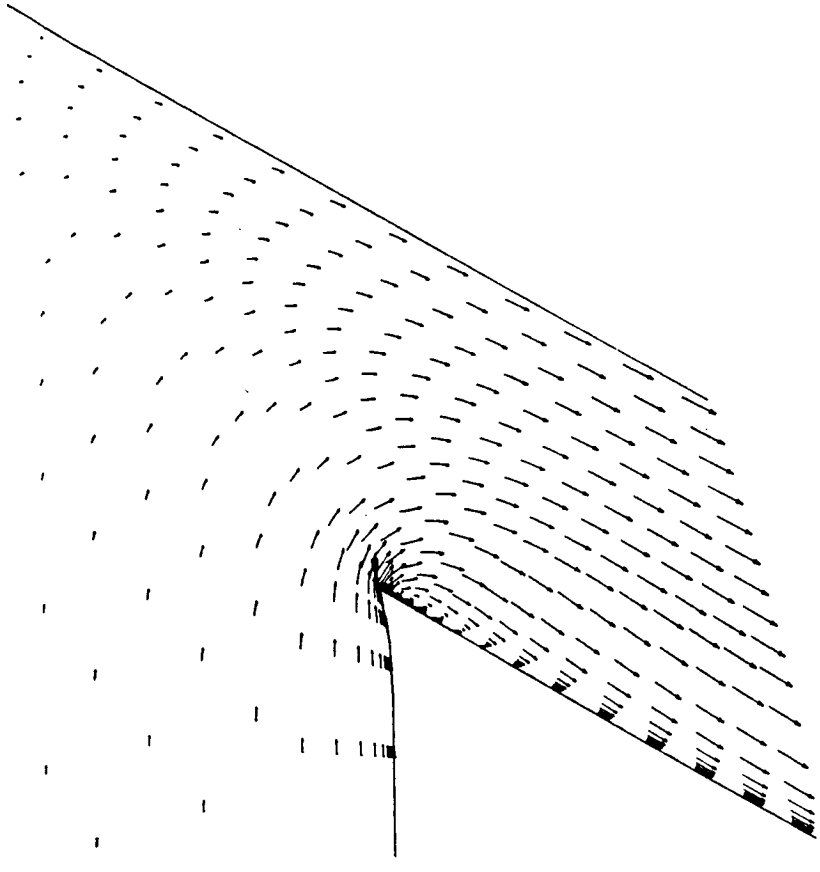

Figure 4.12a Velocity Vectors for Fully Deployed Thrust Reversing Nozzle - NPR = 3.0 - 32x27 Mesh - First-Order.

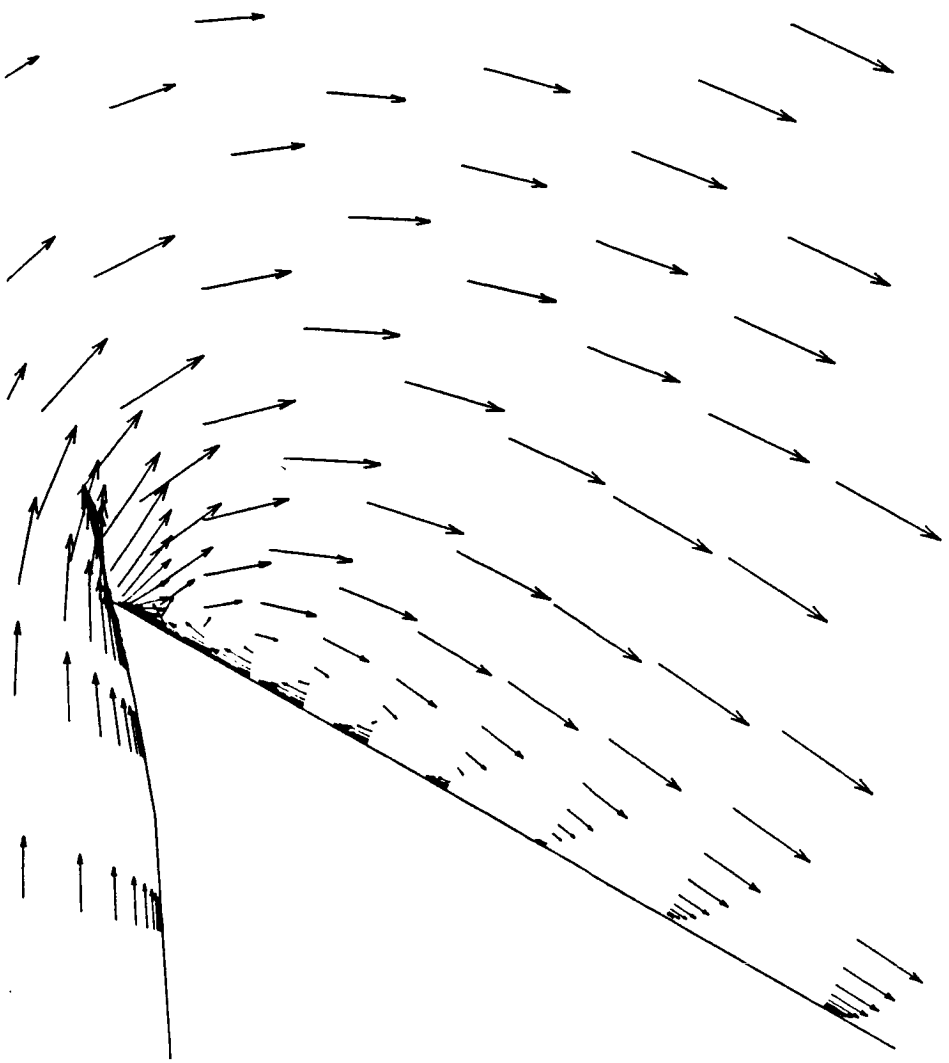

Figure 4.12b Details of Separation - NPR = 3.0 - First-Order.

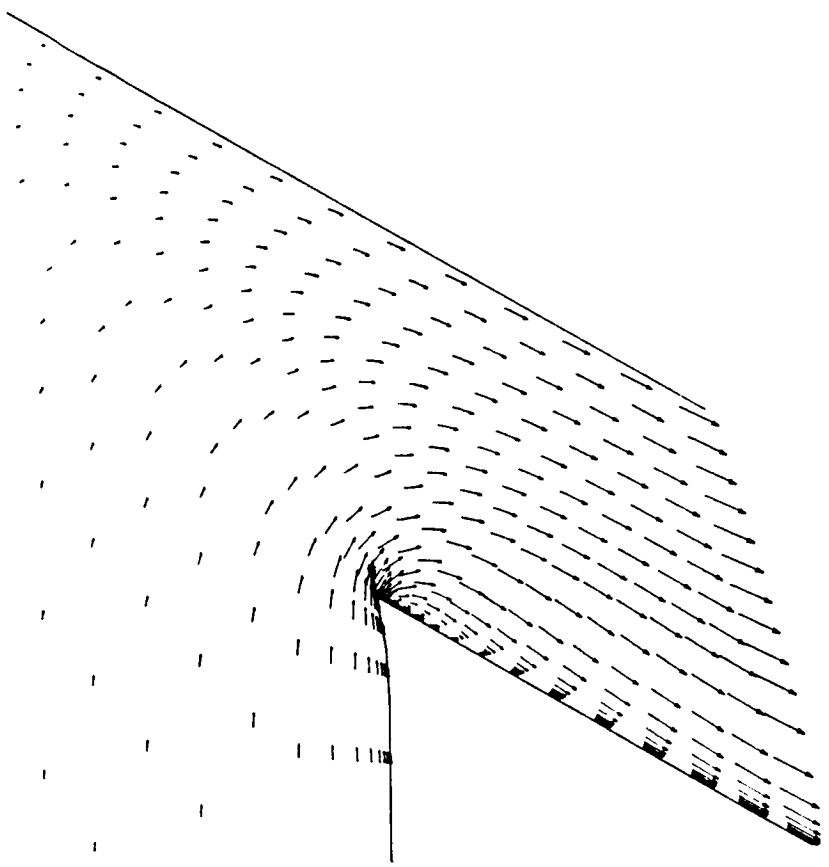

Figure 4.13a Velocity Vectors for Fully Deployed Thrust Reversing Nozzle - NPR = 5.0 - 32x27 Mesh - First-Order.

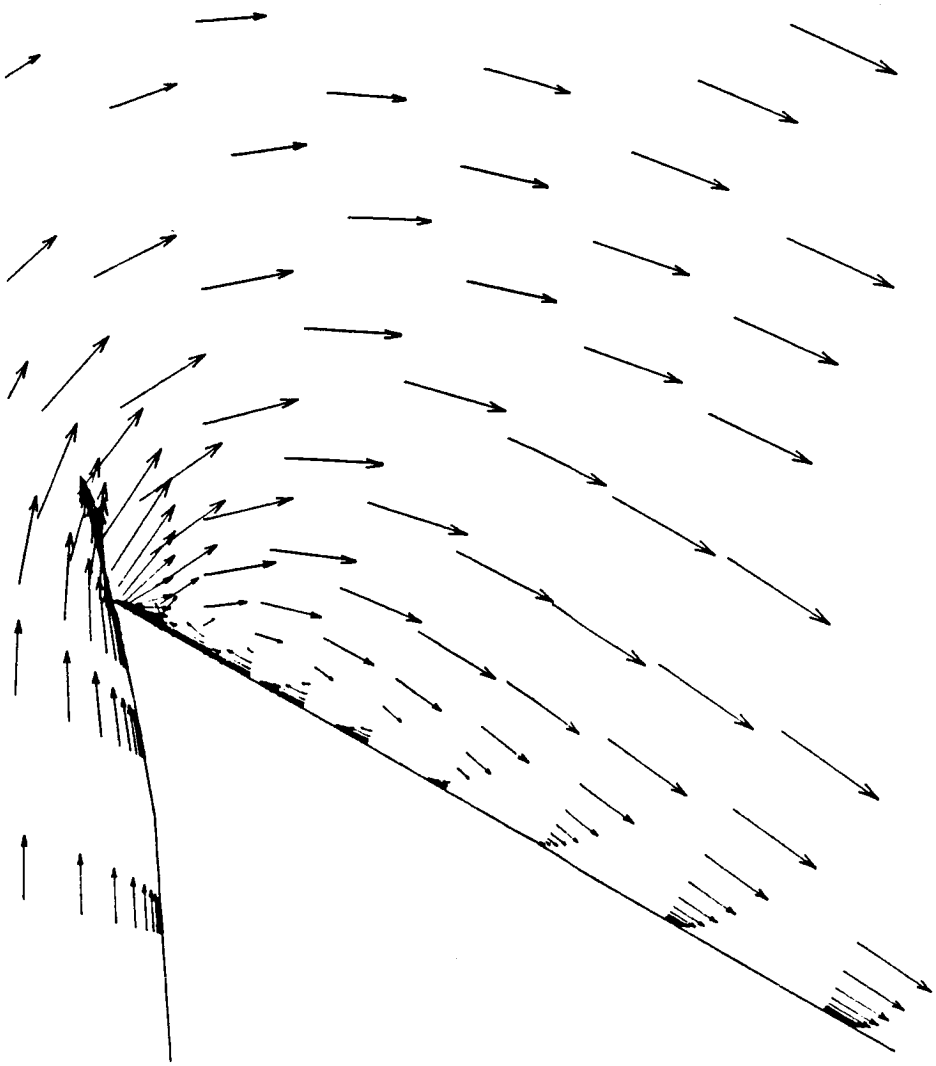

Figure 4.13b Details of Separation - NPR = 5.0 - First-Order.

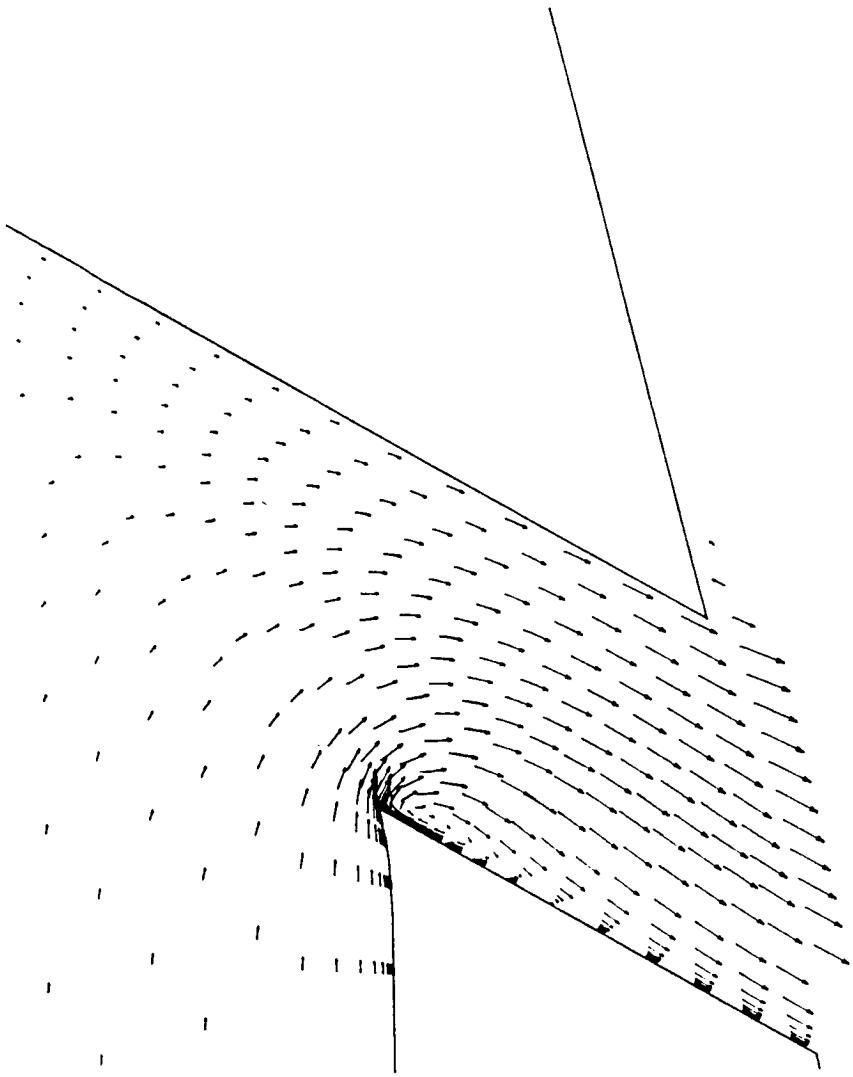

Figure 4.14a Velocity Vectors for Fully Deployed Thrust Reversing Nozzle NPR = 3.0 - 32x27 Internal Mesh - 9x56 External Mesh - Second-Order.

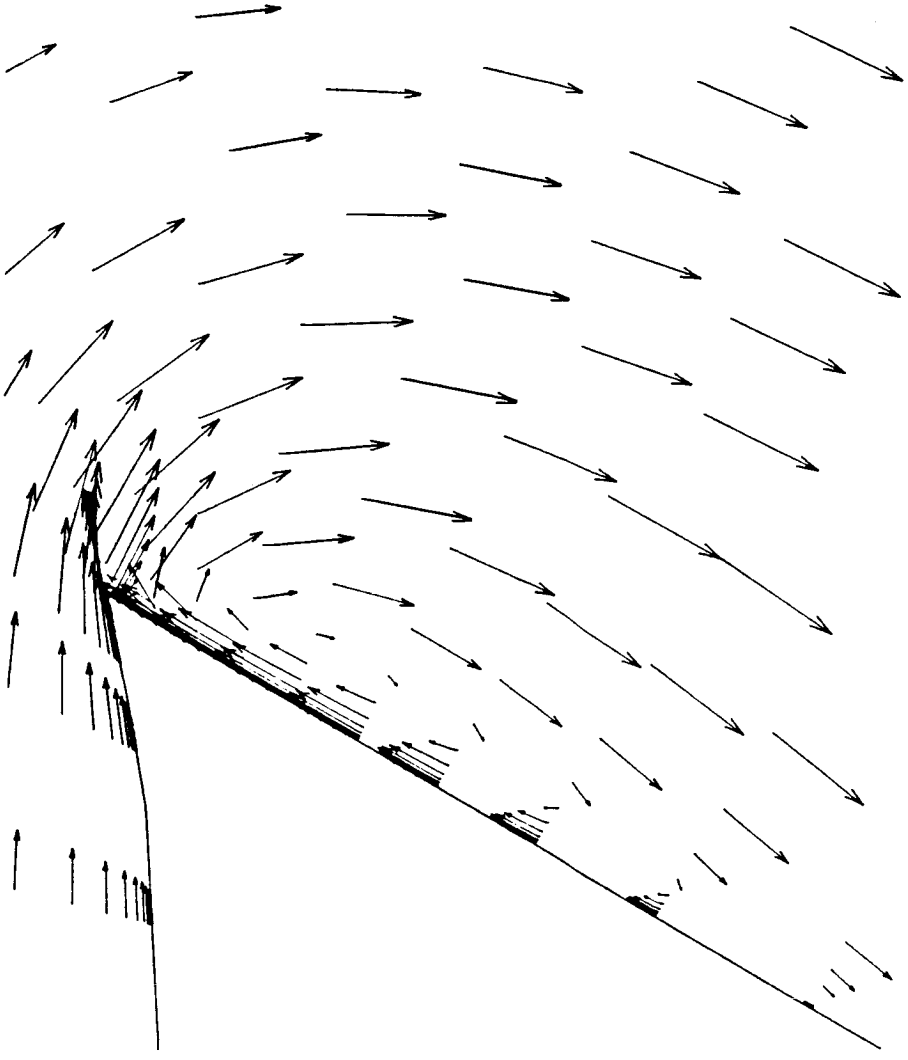

Figure 4.14b Details of Separation - NPR = 3.0 - Second-Order.

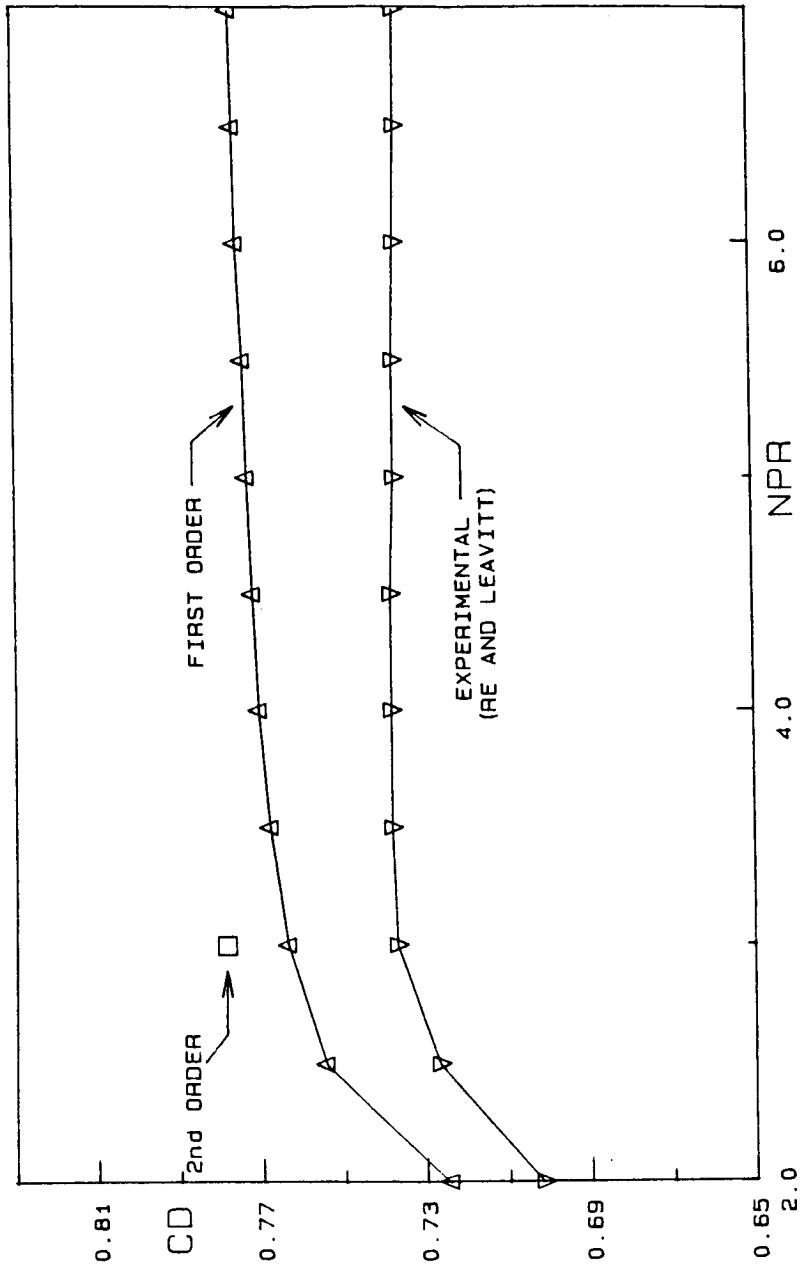

Figure 4.15 Variation of Discharge Coefficient with Nozzle Pressure Ratio for Fully Deployed Thrust Reversing Nozzle.

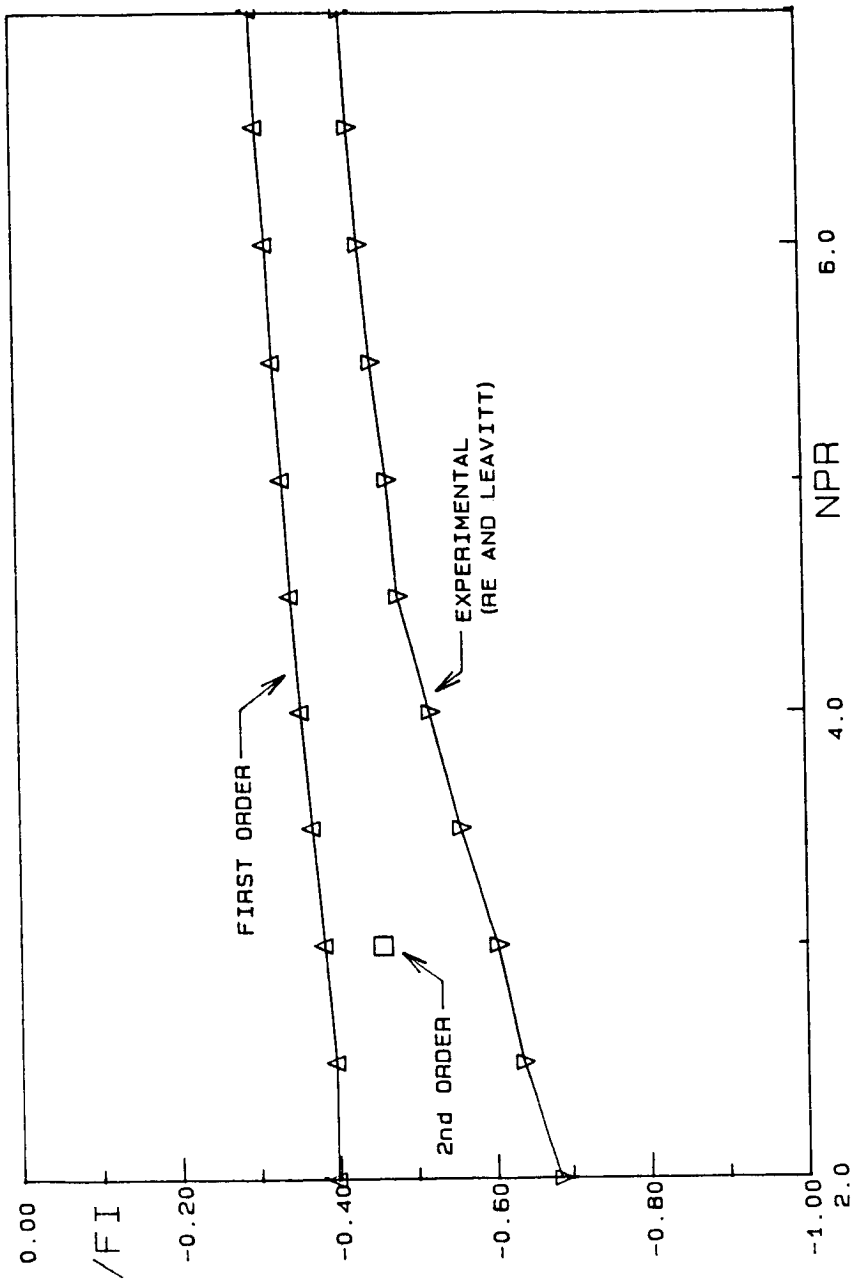

Figure 4.16 Variation of Normalized Thrust with Nozzle Pressure Ratio for a Fully Deployed Thrust Reversing Nozzle.

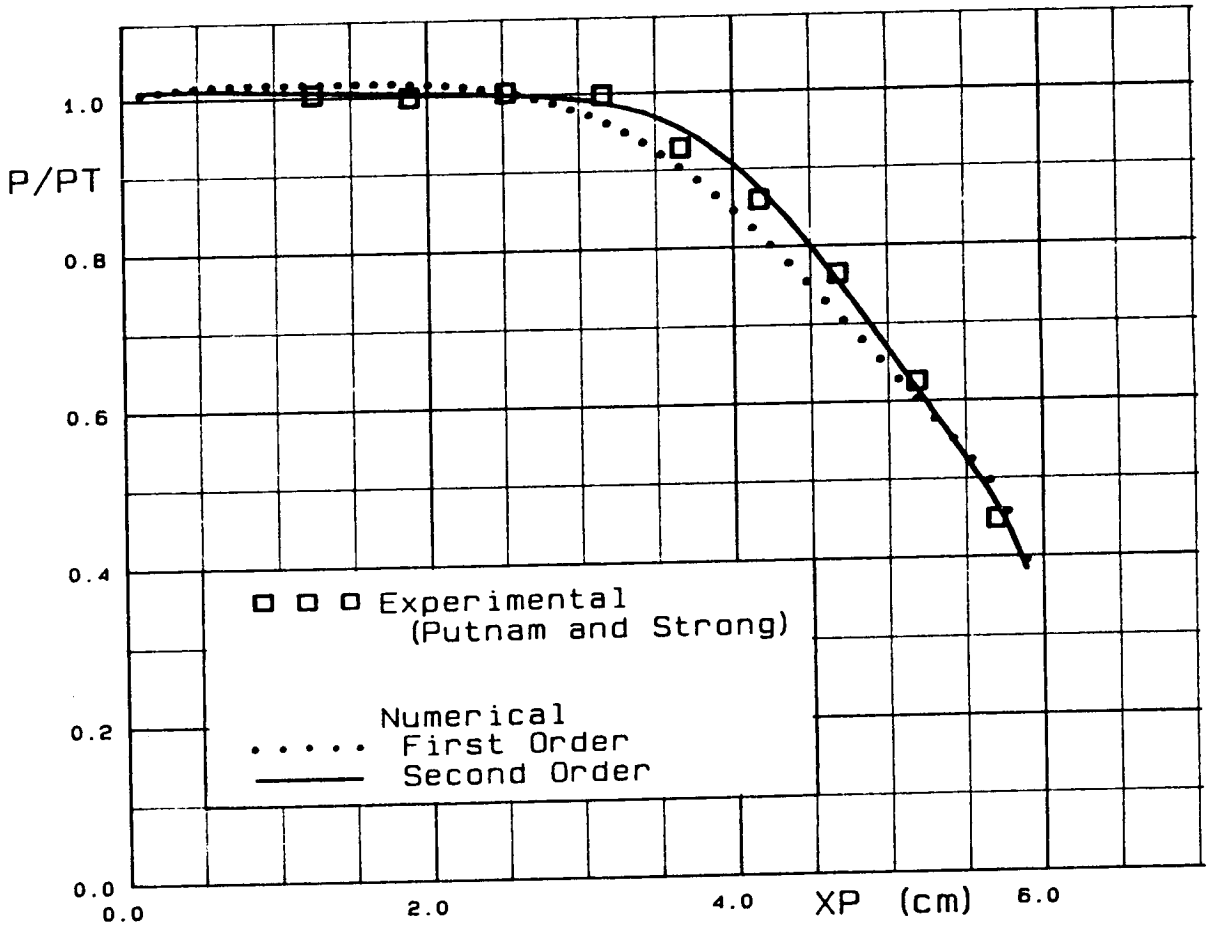

Figure 4.17 Sidewall Pressure Distribution at ZP = 0.203 cm - NPR = 3.0

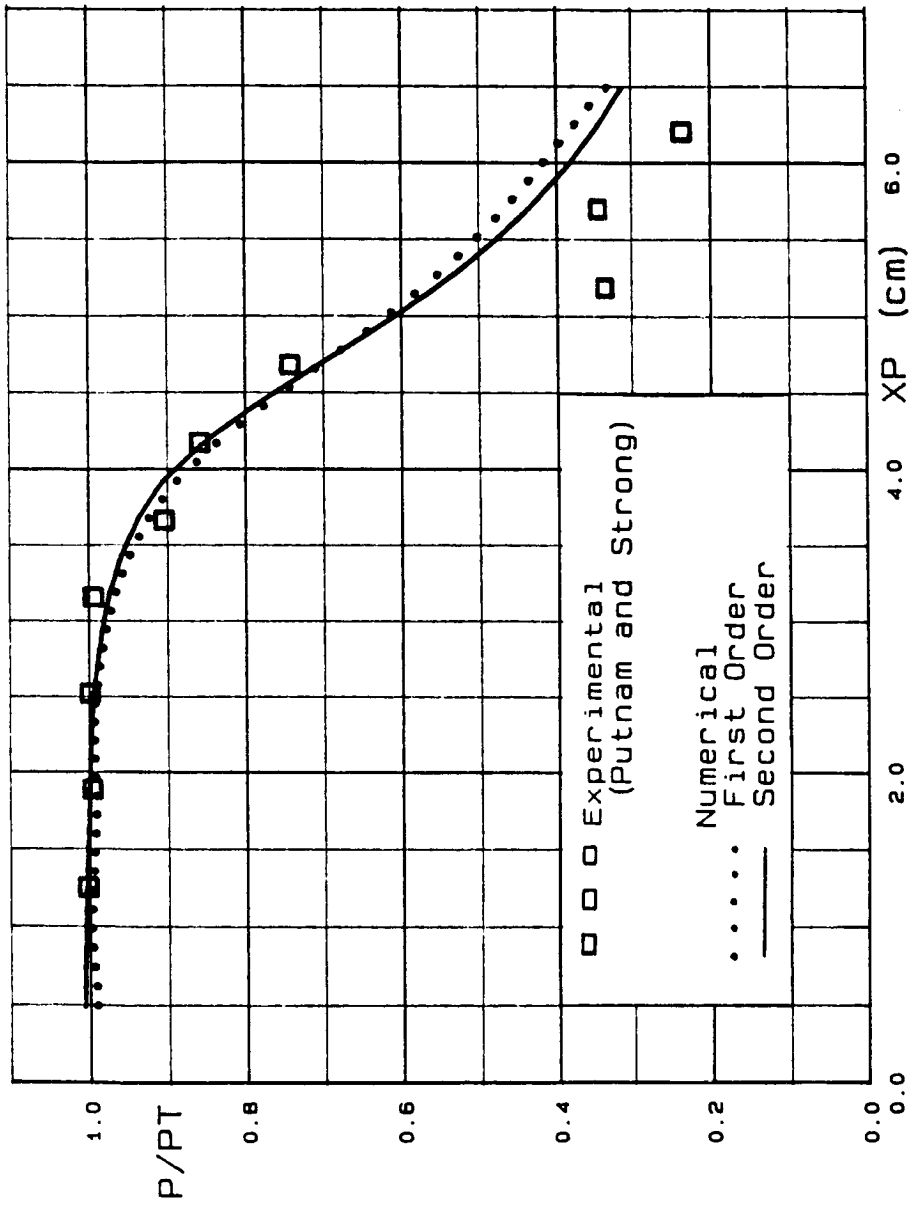

Figure 4.18 Sidewall Pressure Distribution at ZP = 0.838 cm - NPR = 3.0.

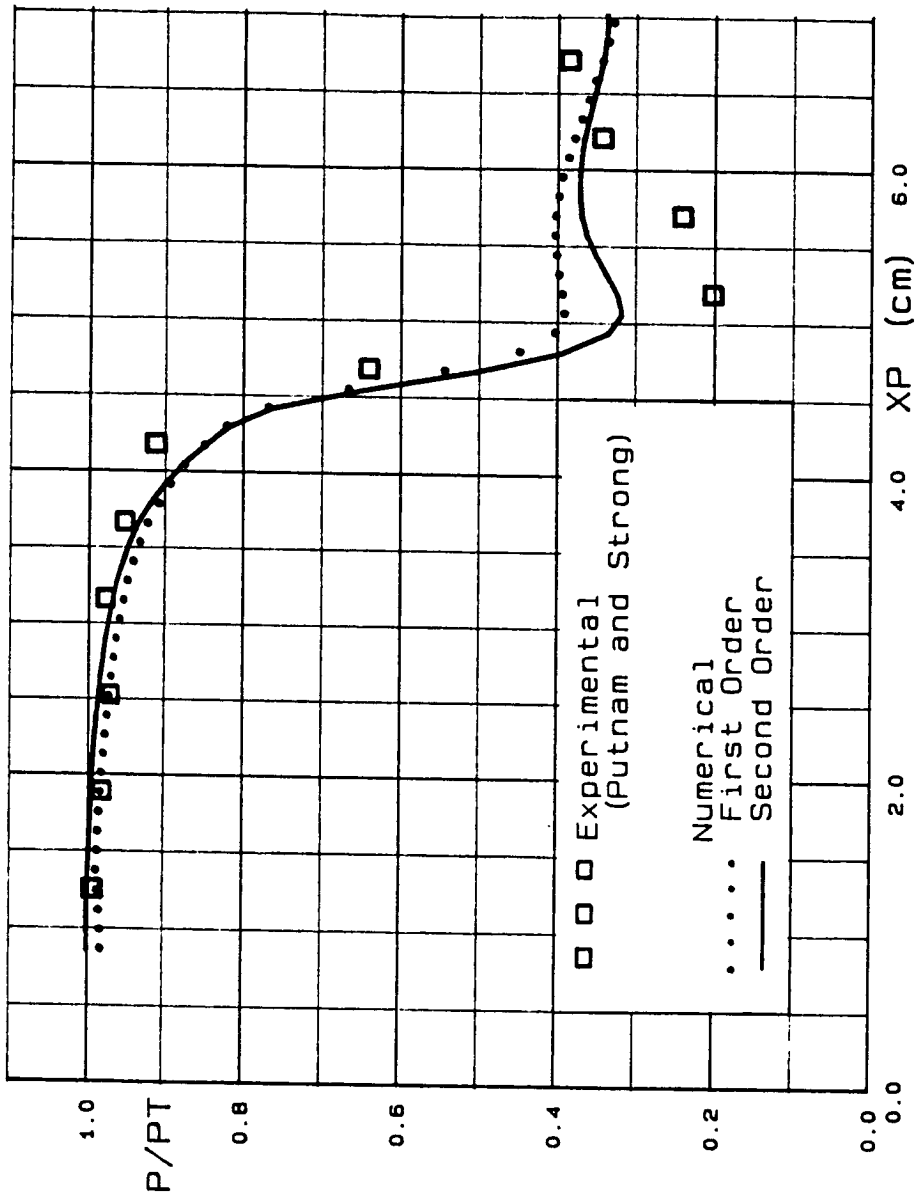

Figure 4.19 Sidewall Pressure Distribution at ZP = 1.473 cm - NPR = 3.0.

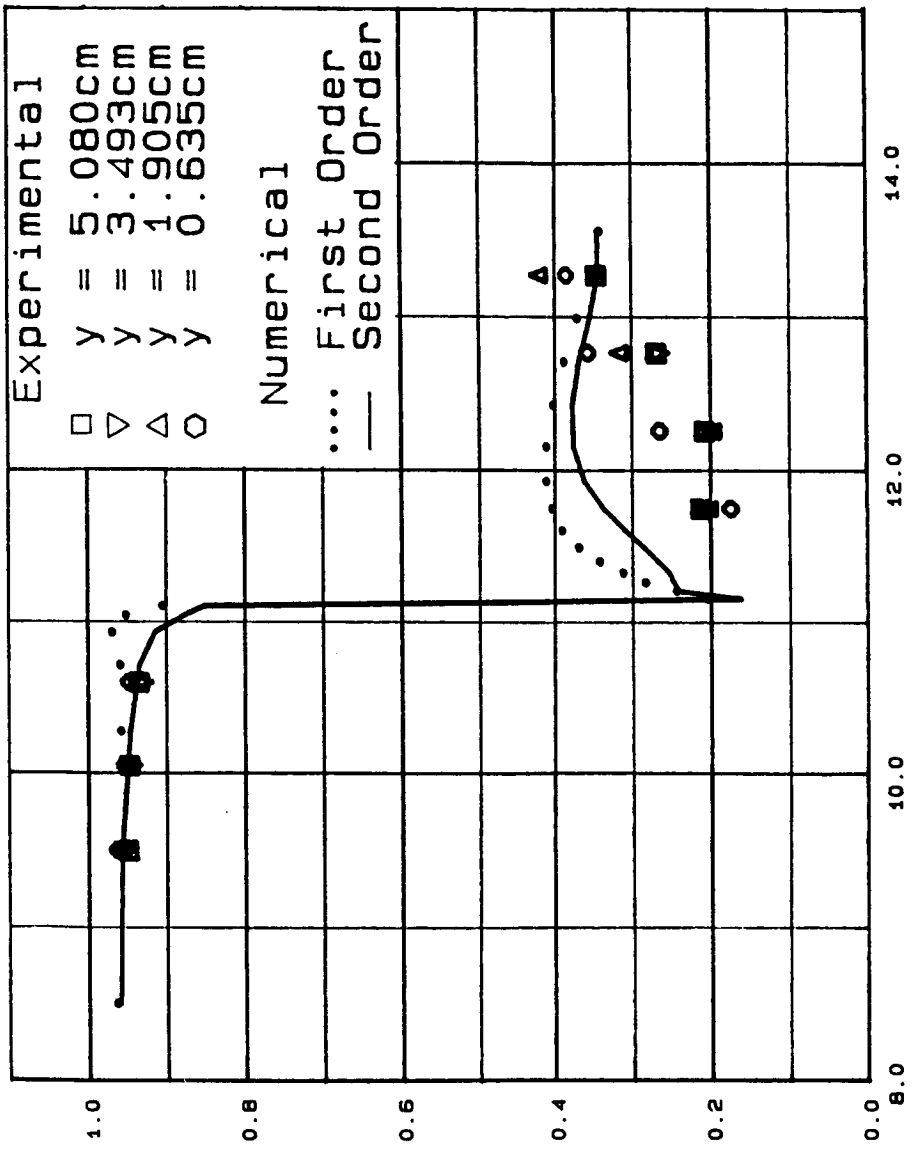

Figure 4.20 Pressures Along Flap for NPR = 3.0.

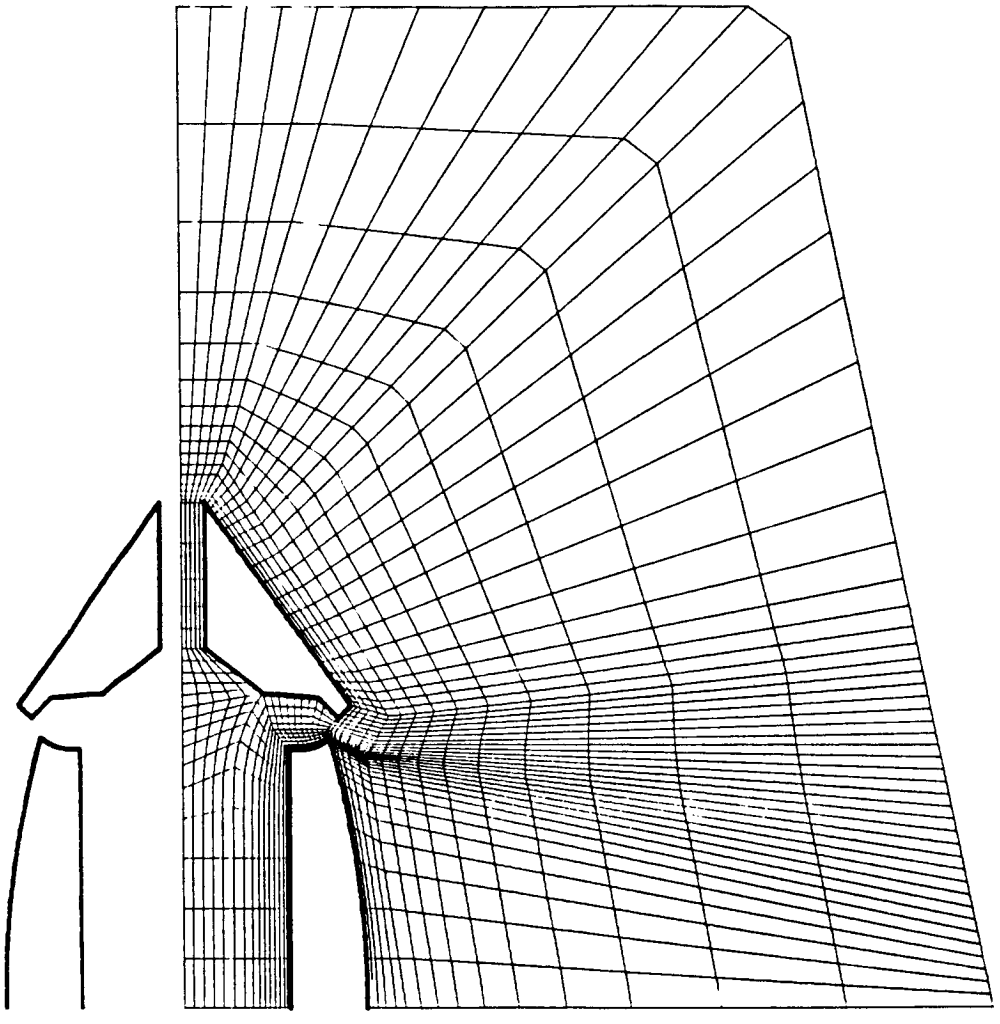

Figure 4.21 Mesh for 50% Deployed Thrust Reversing Nozzle 22x20 Internal Mesh and 18x55 External Mesh

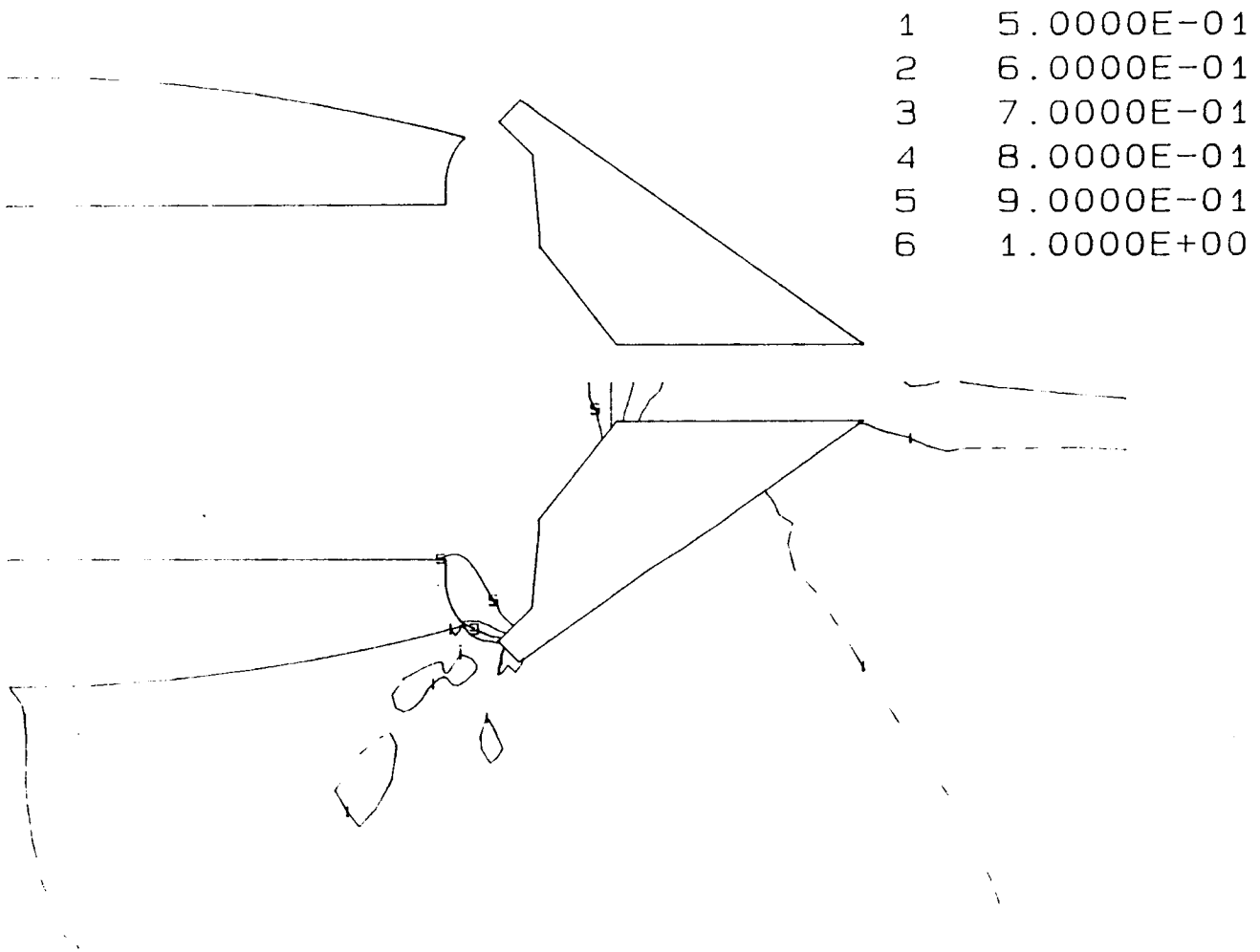

Figure 4.22 Pressure Contours for 50% Deployed Nozzle NPR=2.0 22x20 Internal Mesh and 18x55 External Mesh.

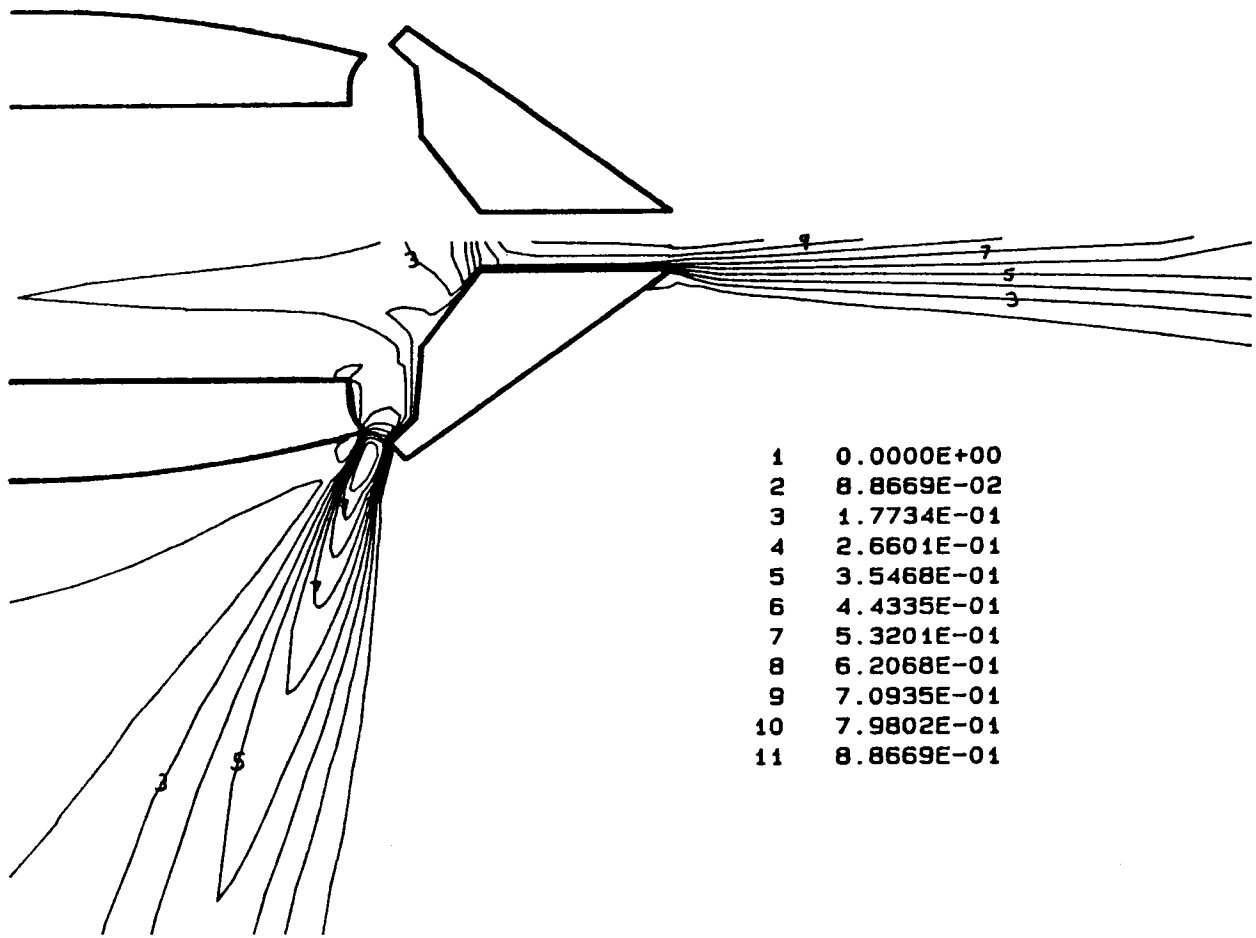

Figure 4.23 Mach Number Contours for Symmetric 50% Deployed Nozzle
22x20 Internal Mesh and 18x55 External Mesh
External Free Stream Mach Number of Zero.

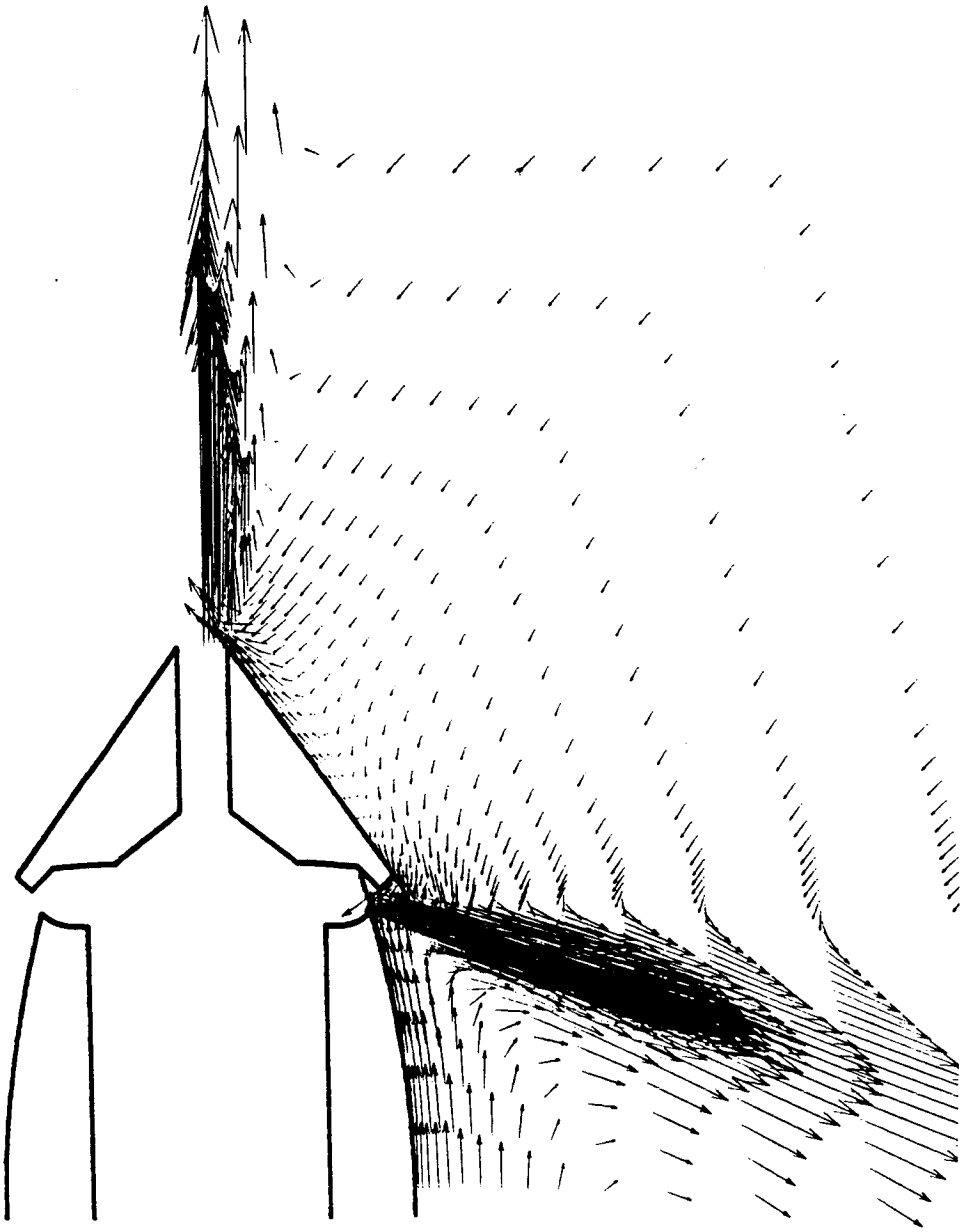

Figure 4.24 Velocity Vectors for Symmetric 50% Deployed Nozzle 22x20 Internal Mesh and 18x55 External Mesh External Mach Number of Zero (Only External Vectors Shown),

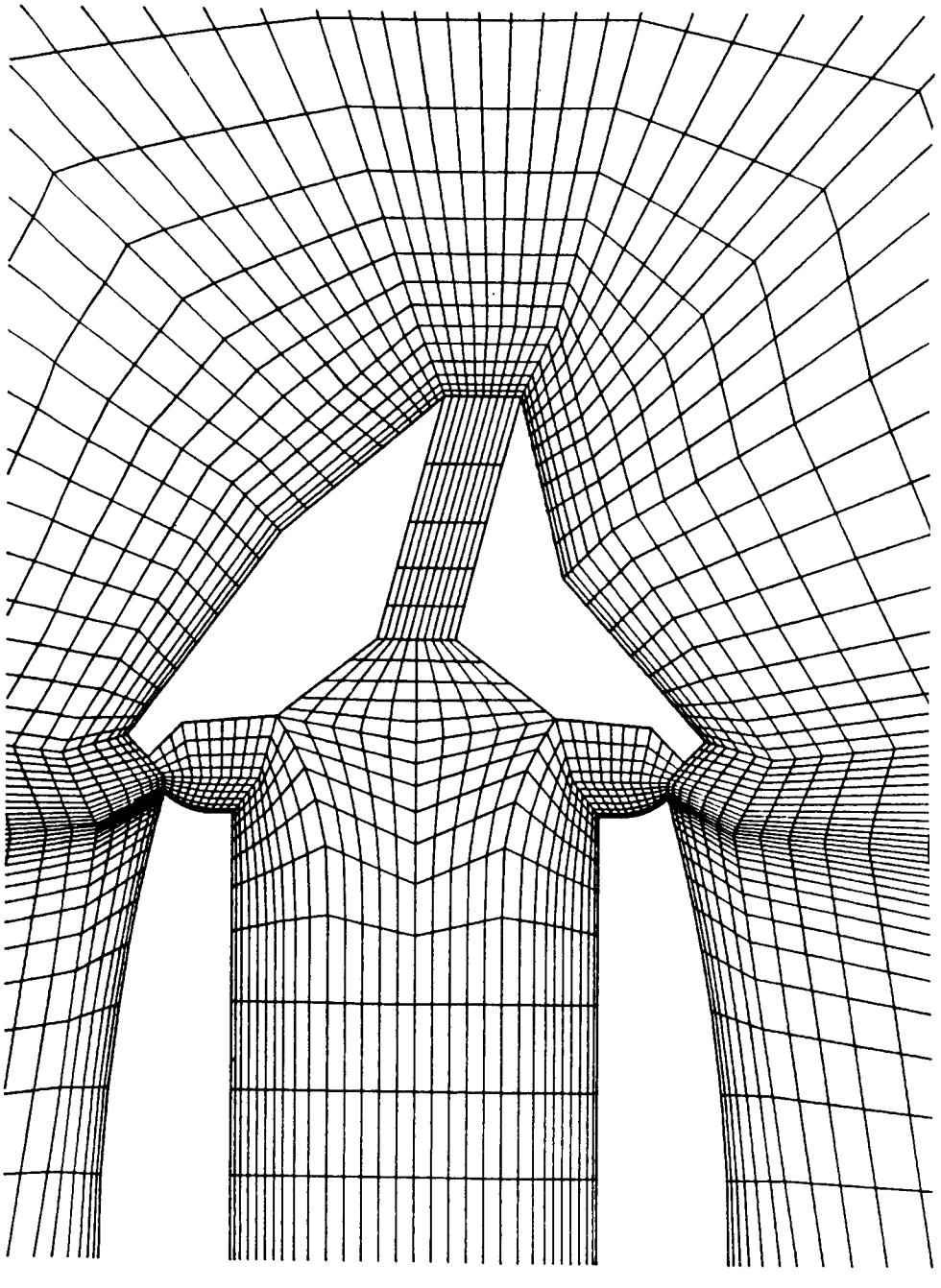

Figure 4.25 Mesh for 50% Deployed Thrust Reversing Nozzle with 15° Downward Thrust Vectoring - 22x38 Internal Mesh and 18x108 External Mesh.

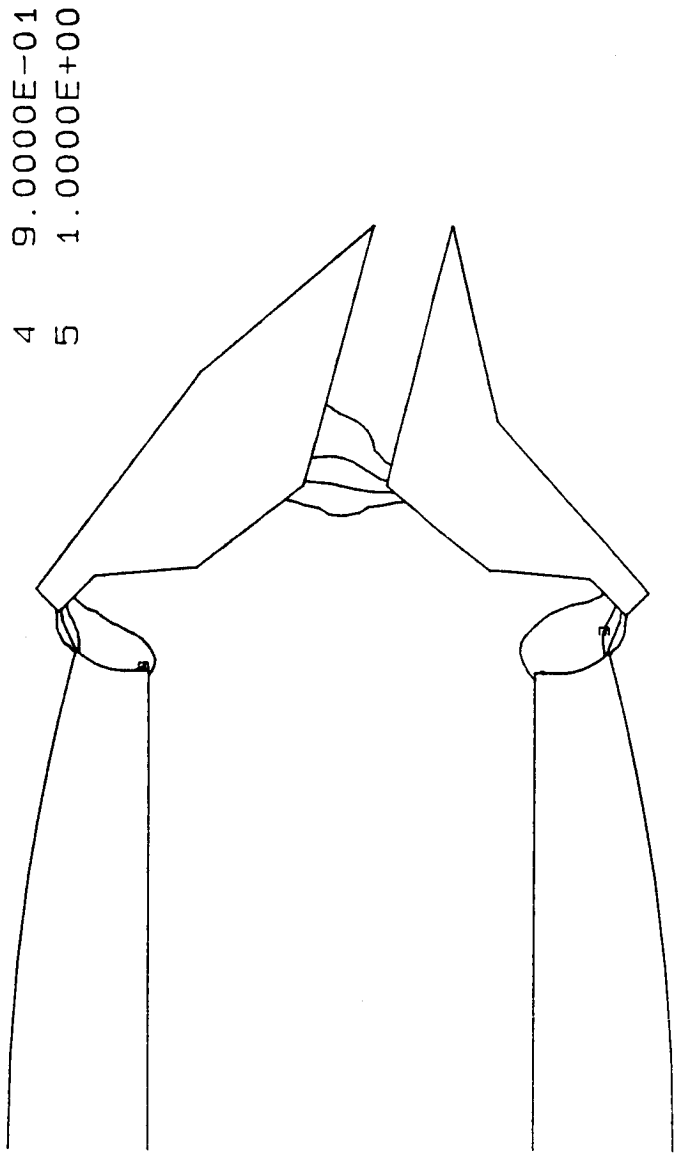

Figure 4.26 Pressure Contours for 50% Deployed Nozzle NPR=2.0
22x38 Internal Mesh - 18x108 External Mesh.

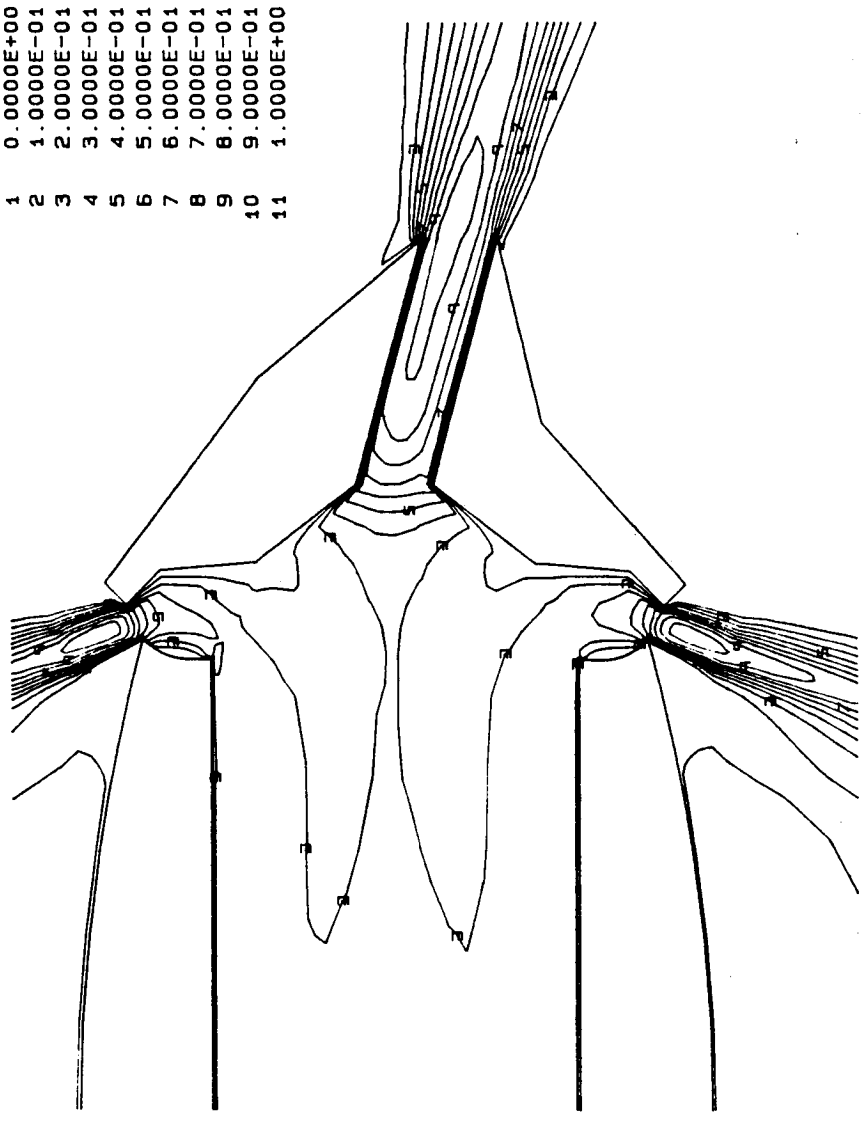

Figure 4.27 Mach Number Contours for 50% Deployed Thrust Reversing Nozzle with 15° Vectoring.

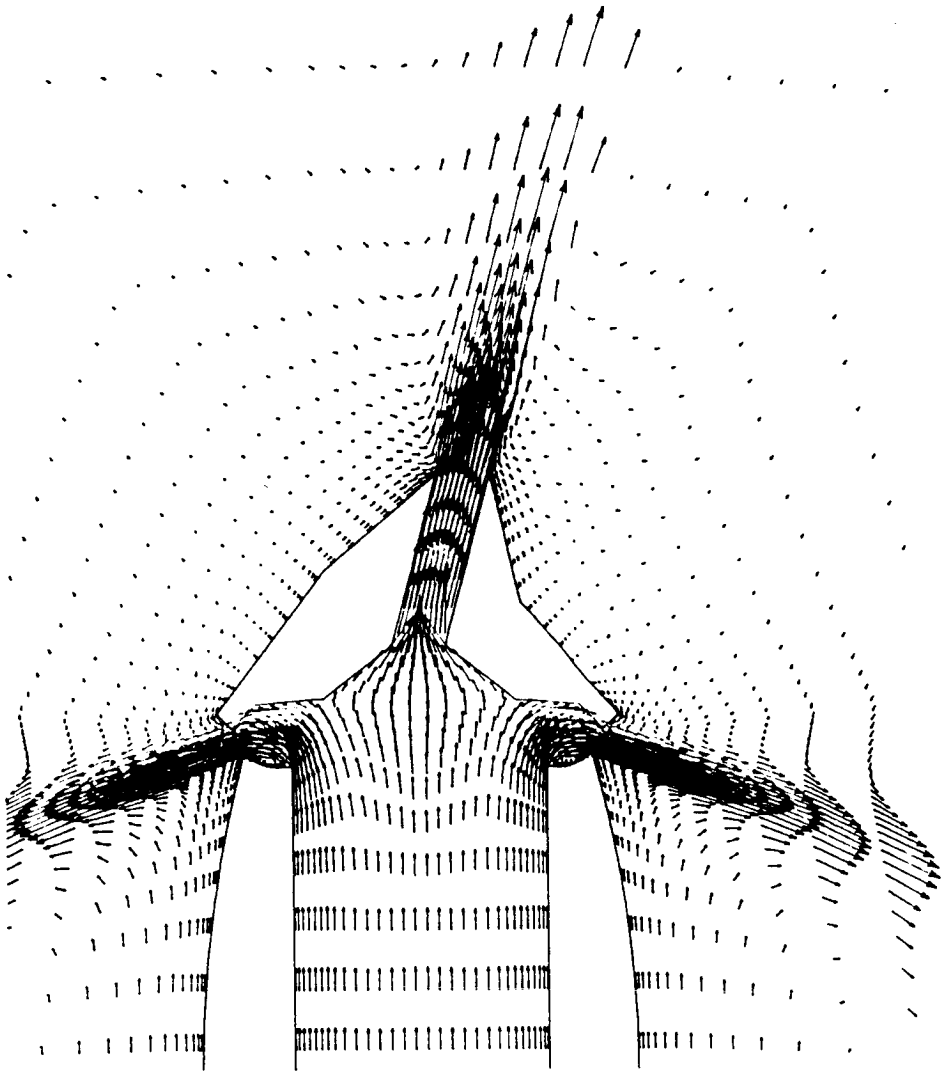

Figure 4.28 Velocity Vectors for 50% Deployed Thrust Reverser with 15 o Vectoring.

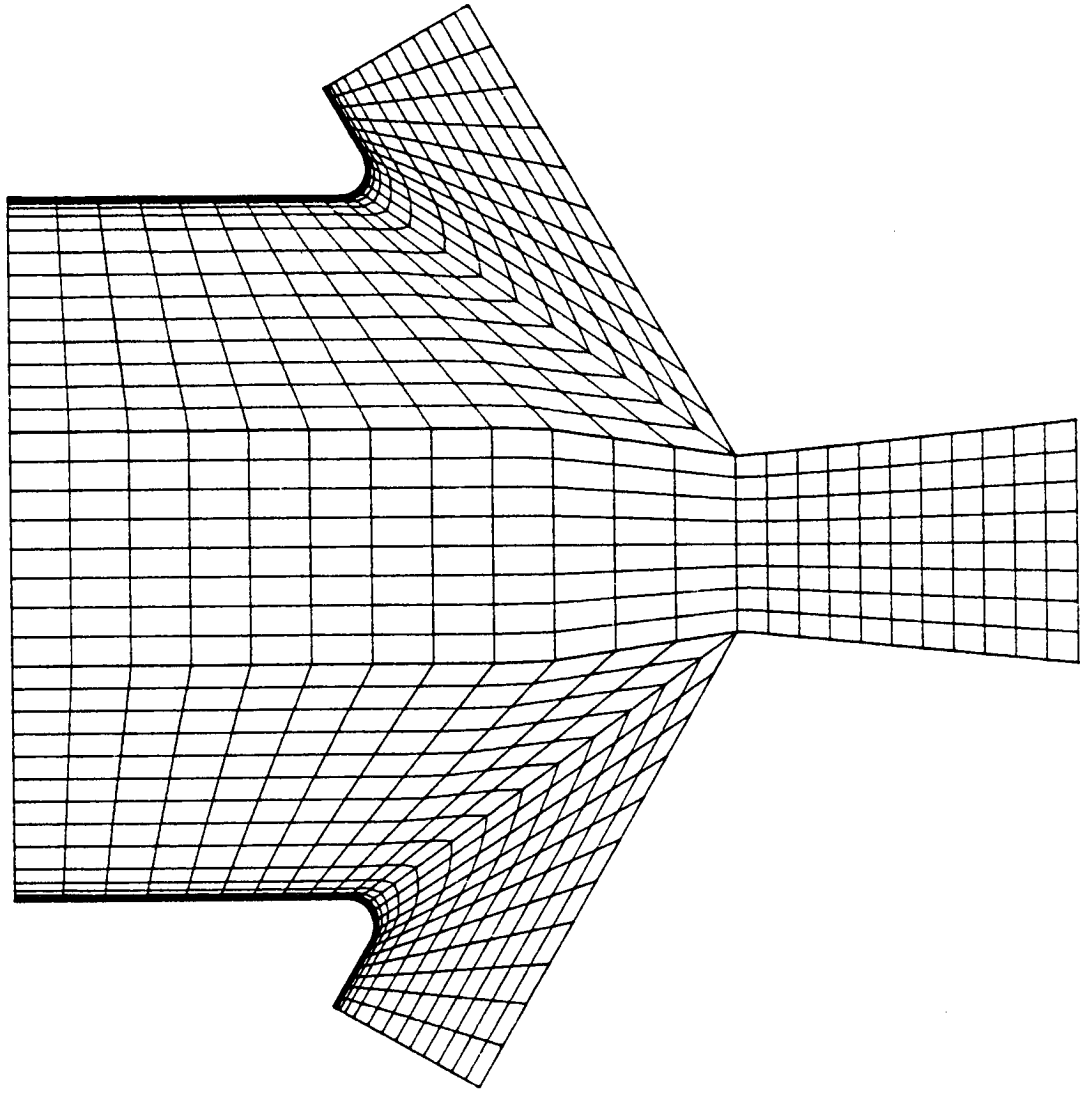

Figure 4.29 Mesh for Steady State Flow Field Calculation Prior to Thrust Vectoring Angle Change.

Time = 1.36 msec.
Thrust Vector Angle = 0.0 deg.

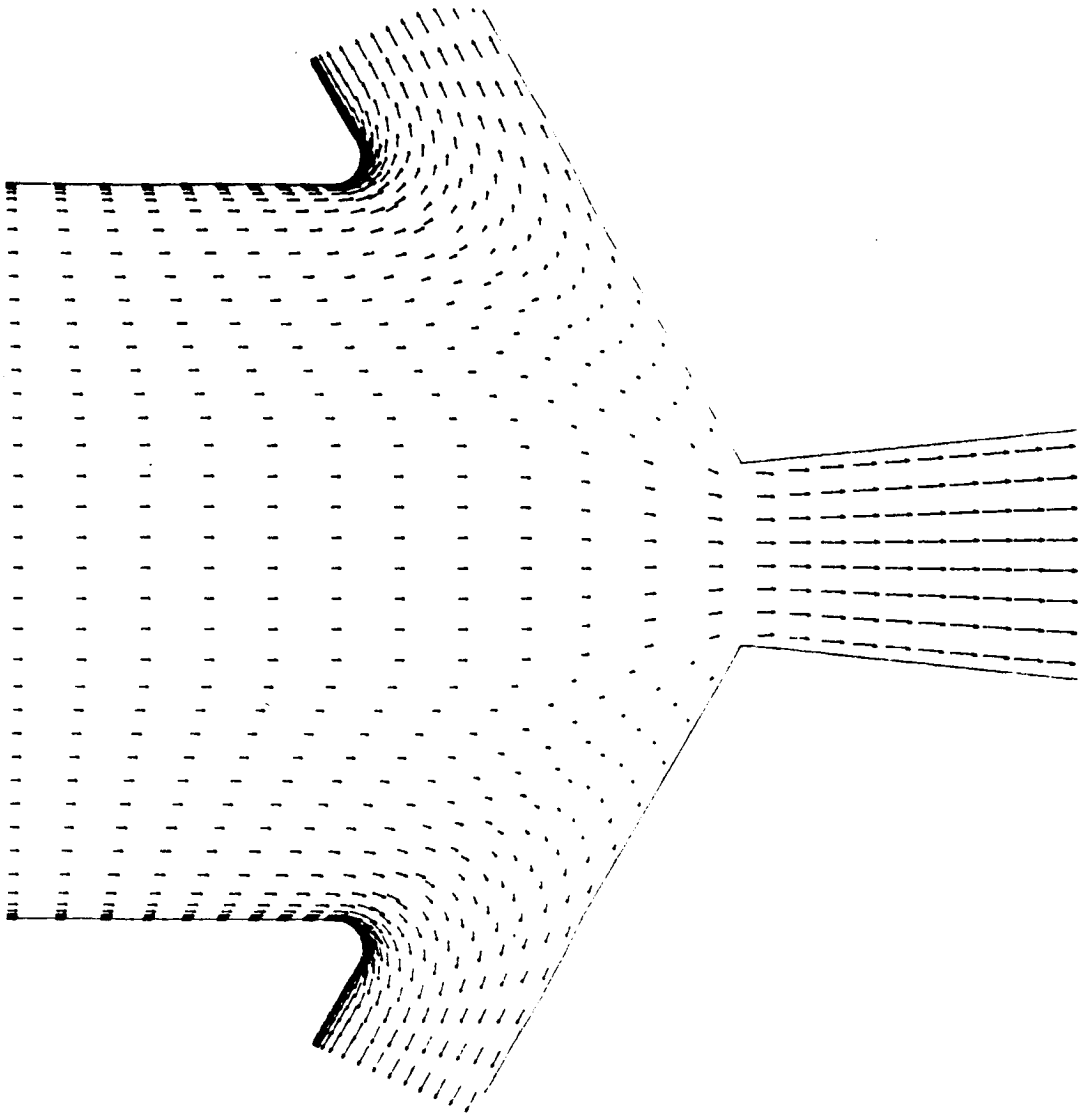

Figure 4.30 Steady State Velocity Vectors Prior to Thrust Vectoring Angle Change.

Time = 1.36 msec.
Thrust Vector Angle = 0.0 deg.

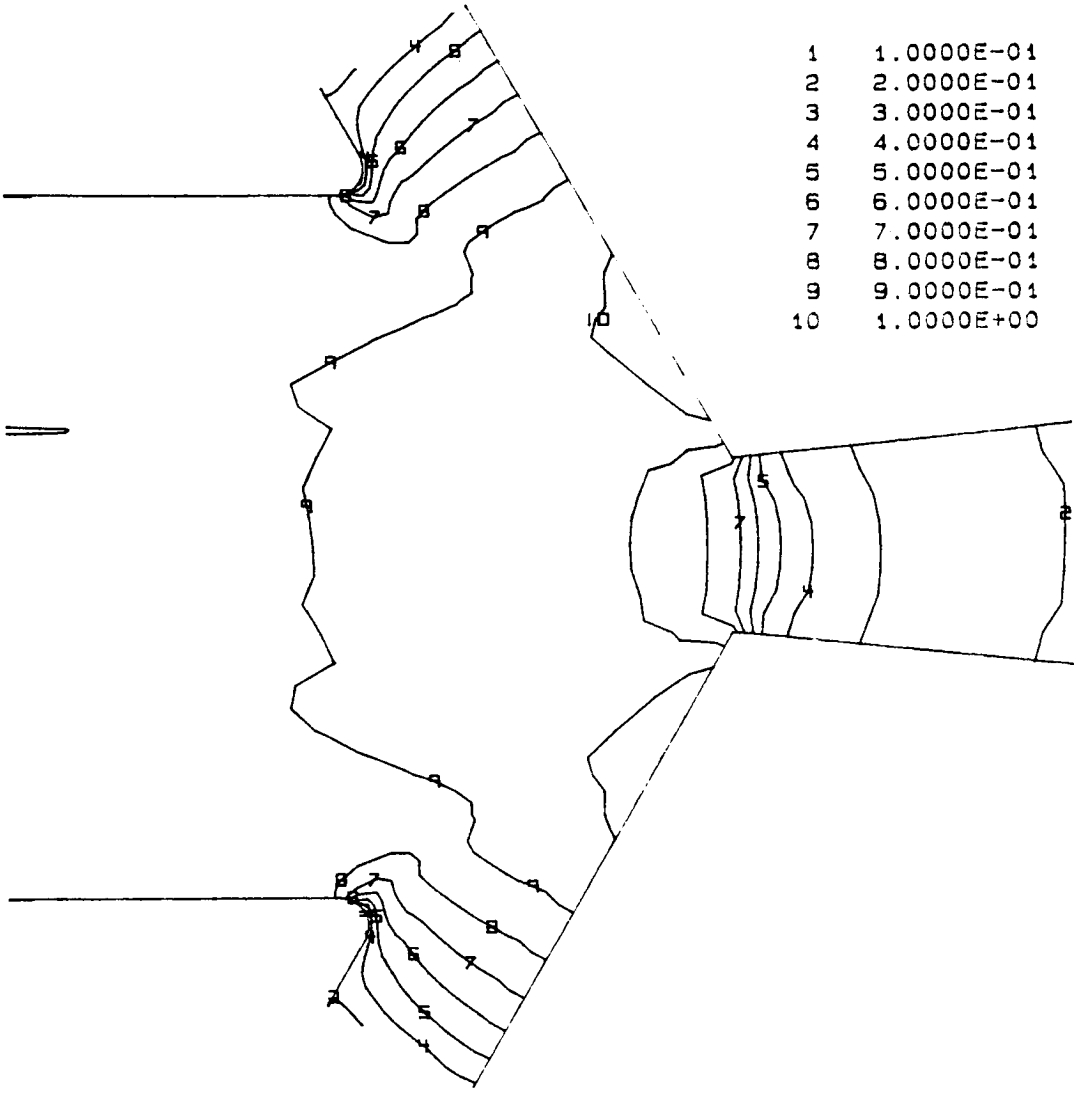

Figure 4.31 Steady State P/P_t Contours Prior to Thrust Vectoring Angle Change.

Time = 1.36 msec.
Thrust Vector Angle = 0.0 deg.

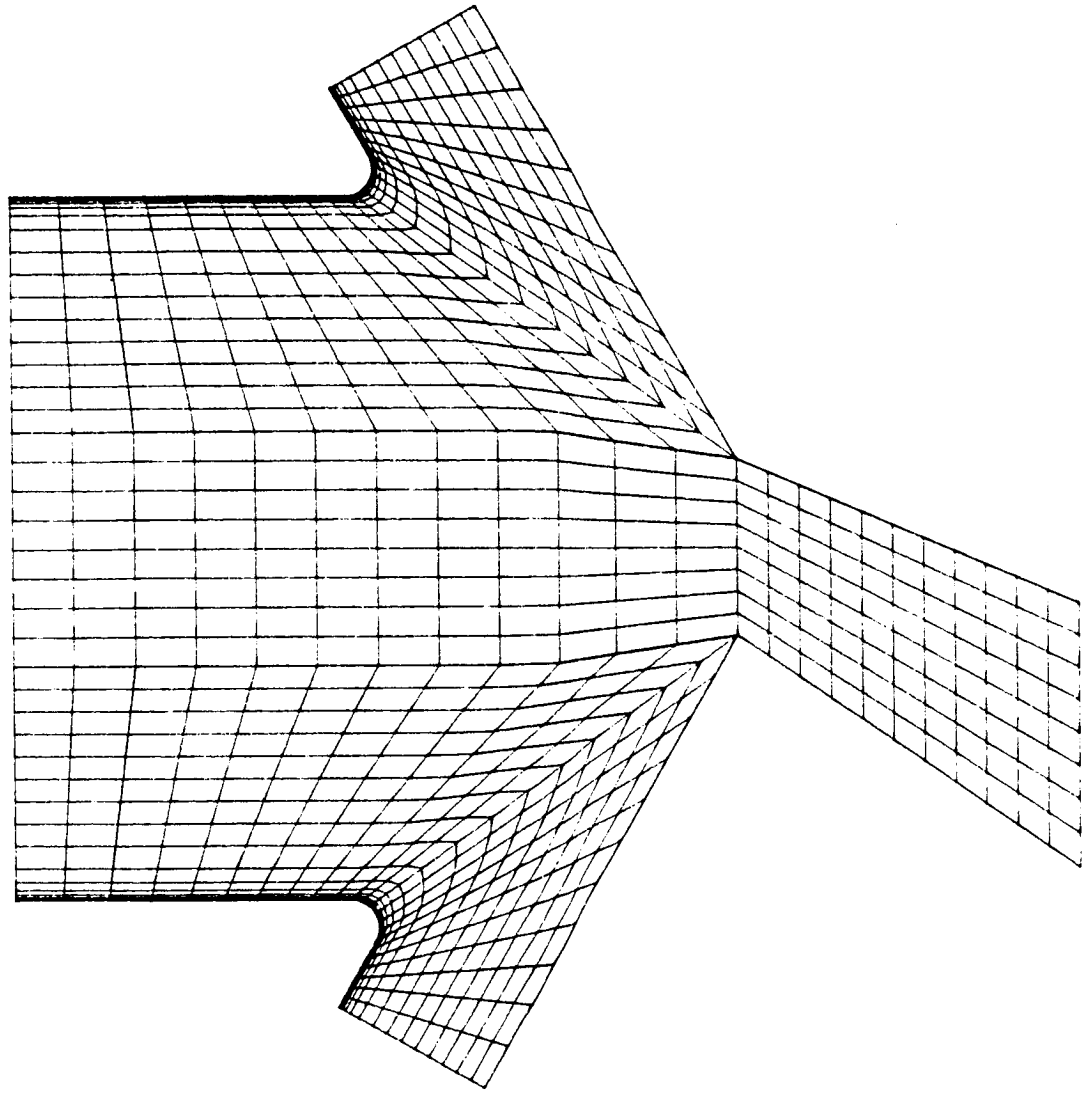

Figure 4.32 Mesh for Transient Flow Field Calculation During Thrust Vectoring Angle Change.

Time = 1.66 msec.
Thrust Vector Angle = 28.90 deg.

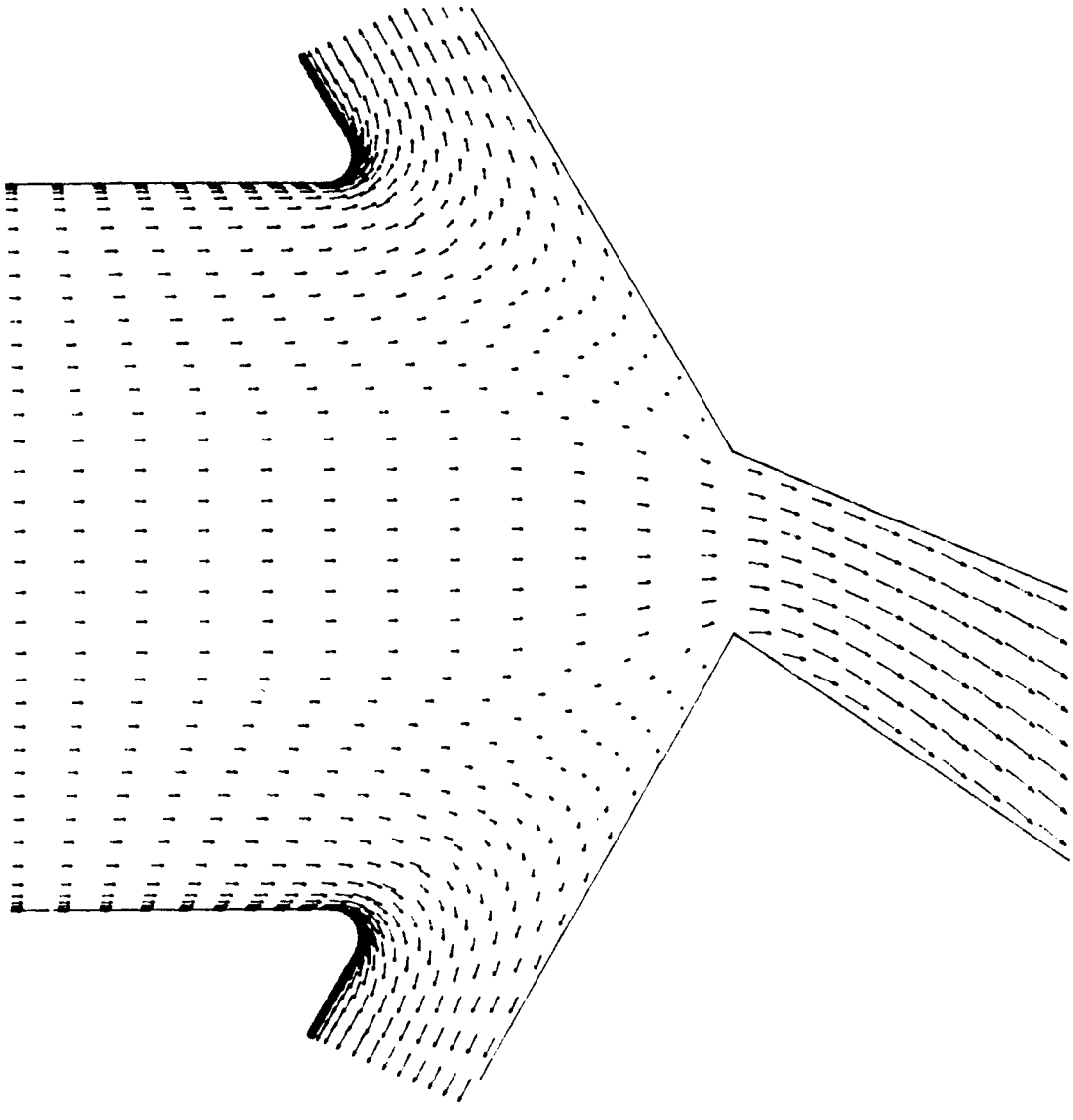

Figure 4.33 Transient Flow Field Velocity Vectors During Thrust Vectoring Angle Change.

Time = 1.66 msec.
Thrust Vector Angle = 28.90 deg.

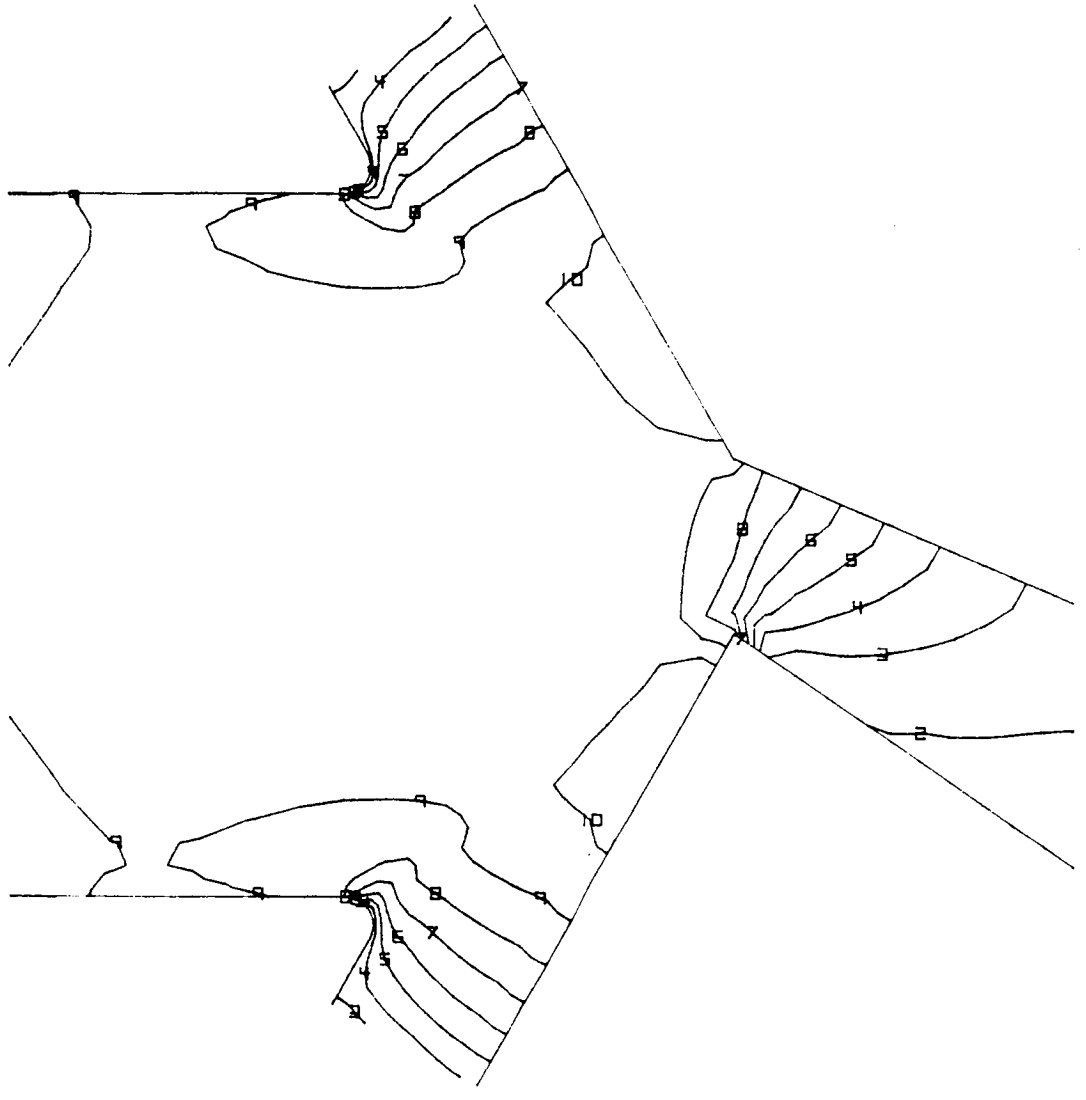

Figure 4.34 Transient Flow Field P/P_t Contours During Thrust Vectoring Angle Change.

Time = 1.66 msec.
Thrust Vector Angle = 28.90 deg.

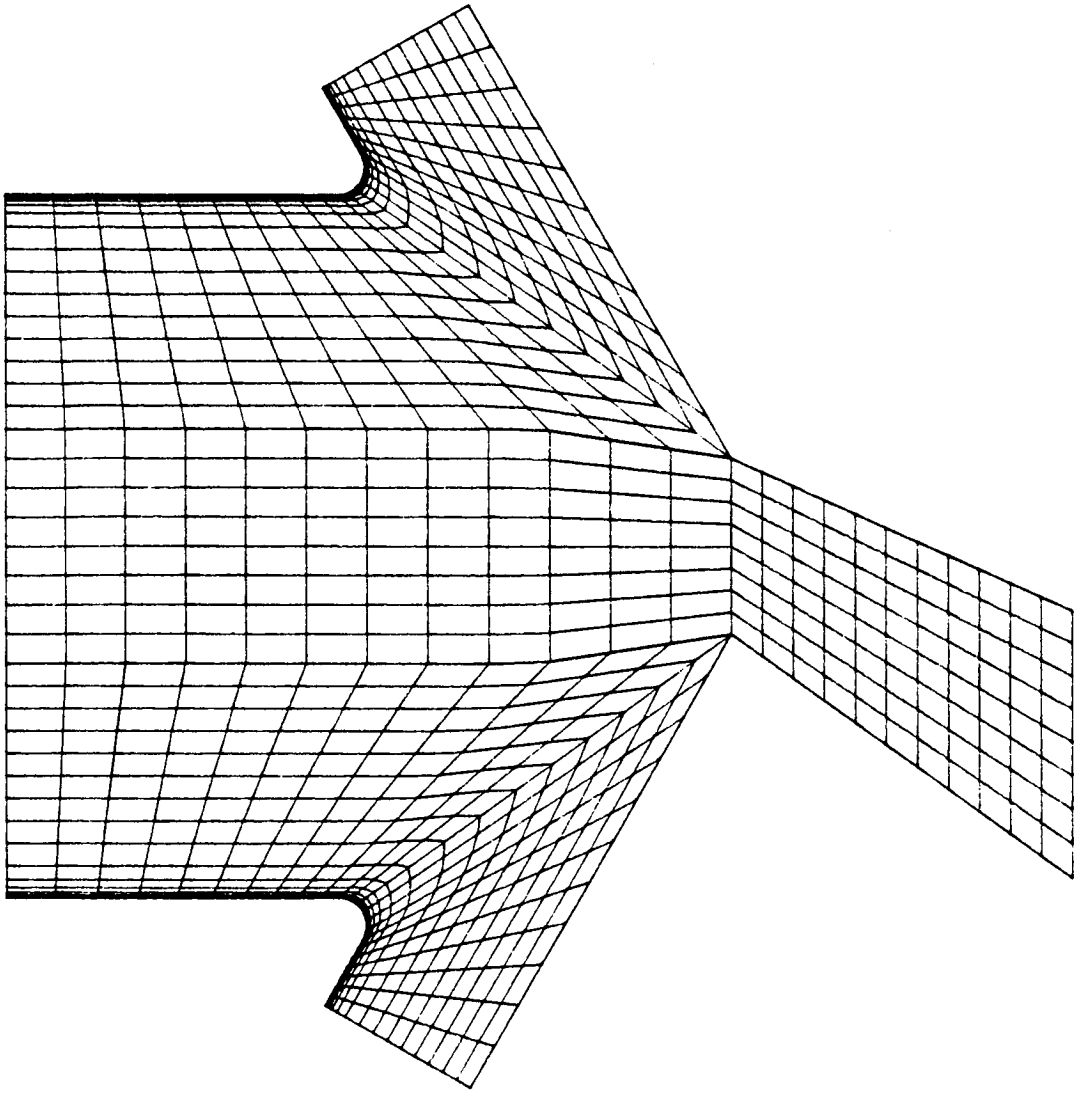

Figure 4.35 Mesh for Transient Flow Field Calculation After Thrust Vectoring Angle Change.

Time = 1.71 msec.
Thrust Vector Angle = 30.00 deg.

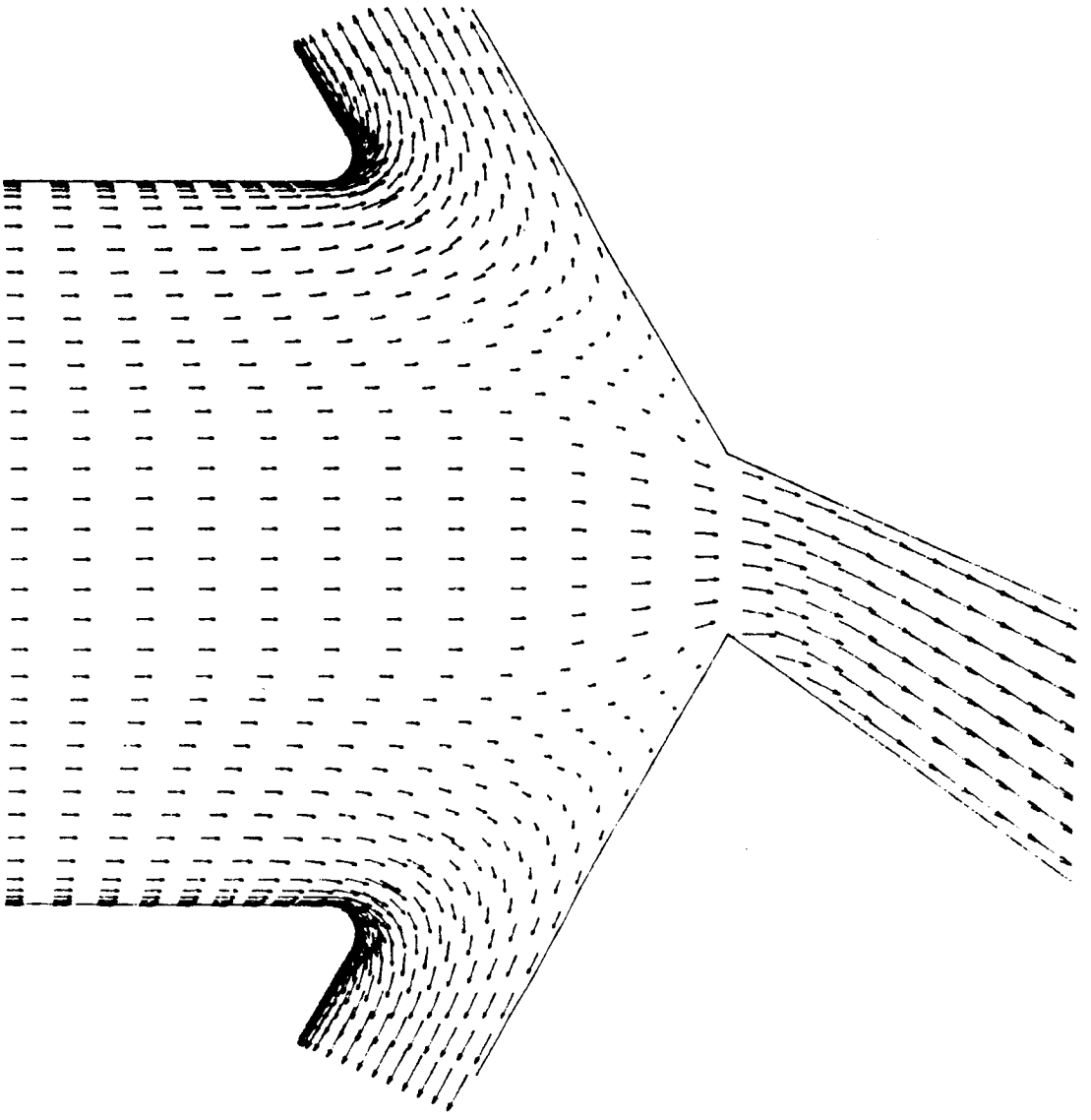

Figure 4.36 Transient Flow Field Velocity Vectors After Thrust Vectoring Angle Change.

Time = 1.71 msec.
Thrust Vector Angle = 30.00 deg.

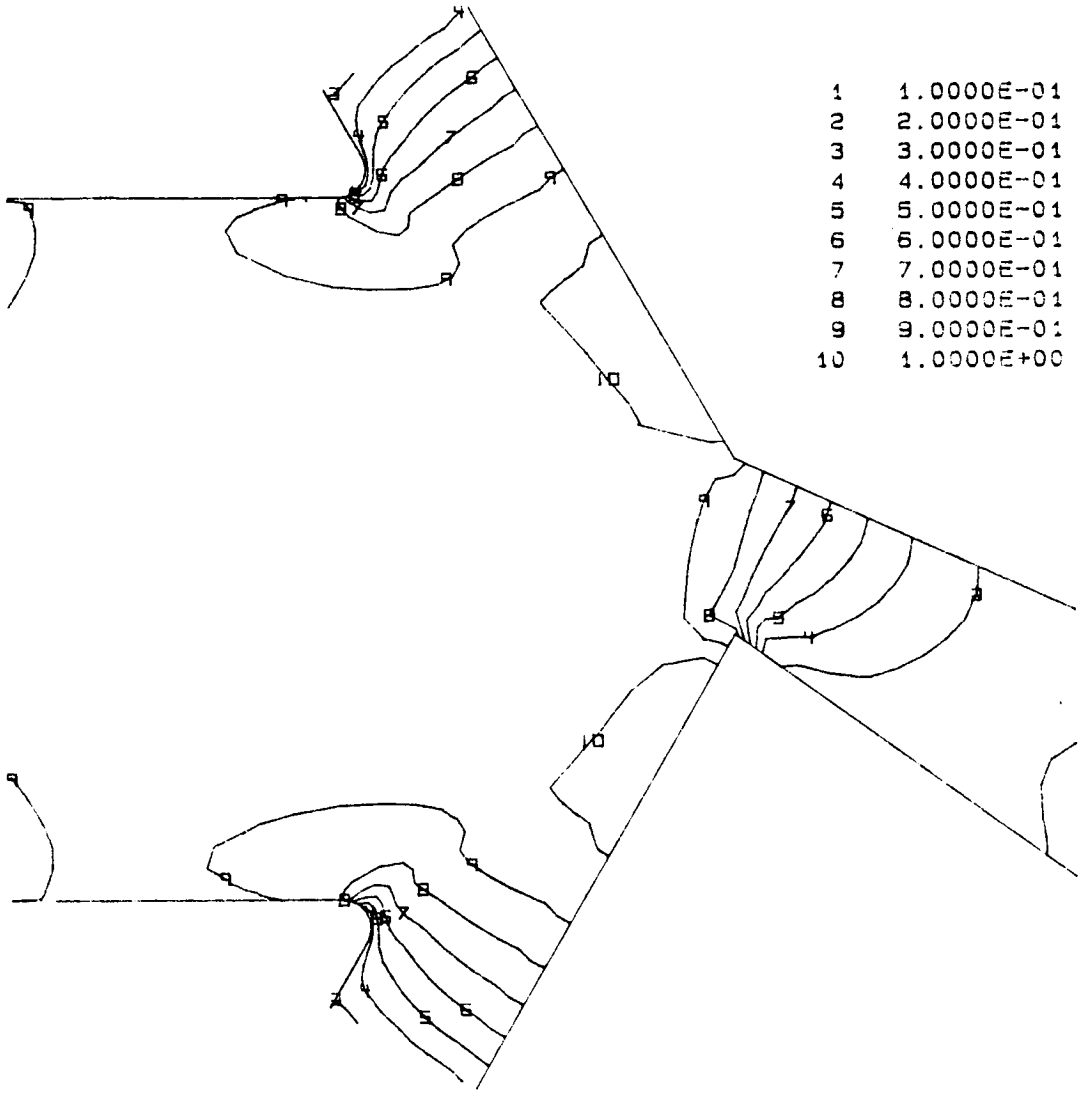

Figure 4.37 Transient Flow Field P/P_t Contours After Thrust Vectoring Angle Change.

Time = 1.71 msec.
Thrust Vectoring Angle = 30.00 deg.

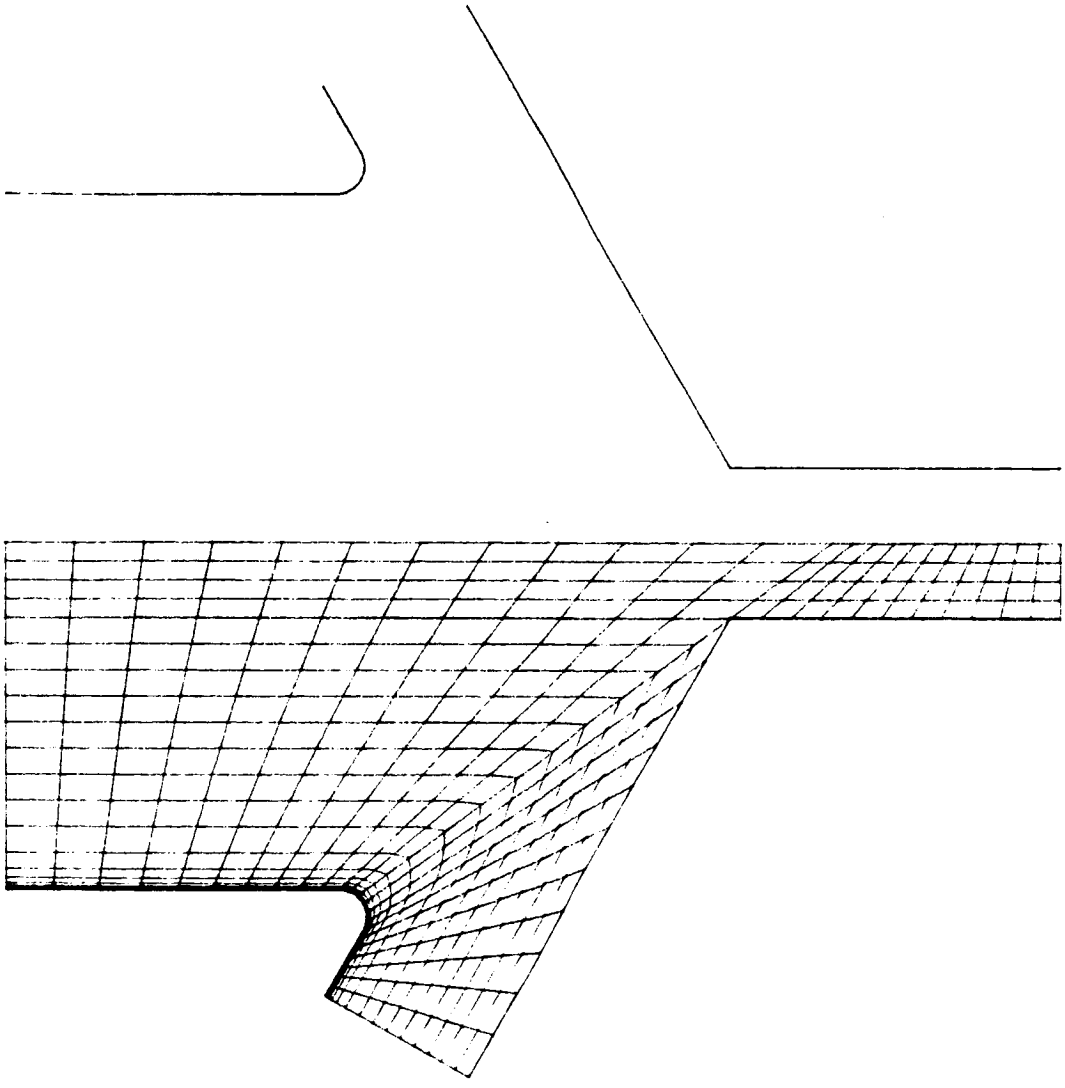

Figure 4.38 Mesh for Steady State Flow Field Calculation Prior to Transition from Partial to Full Thrust Reverser Deployment.

Time = 1.44 msec.
Rear Port Width = 0.0500 ft.

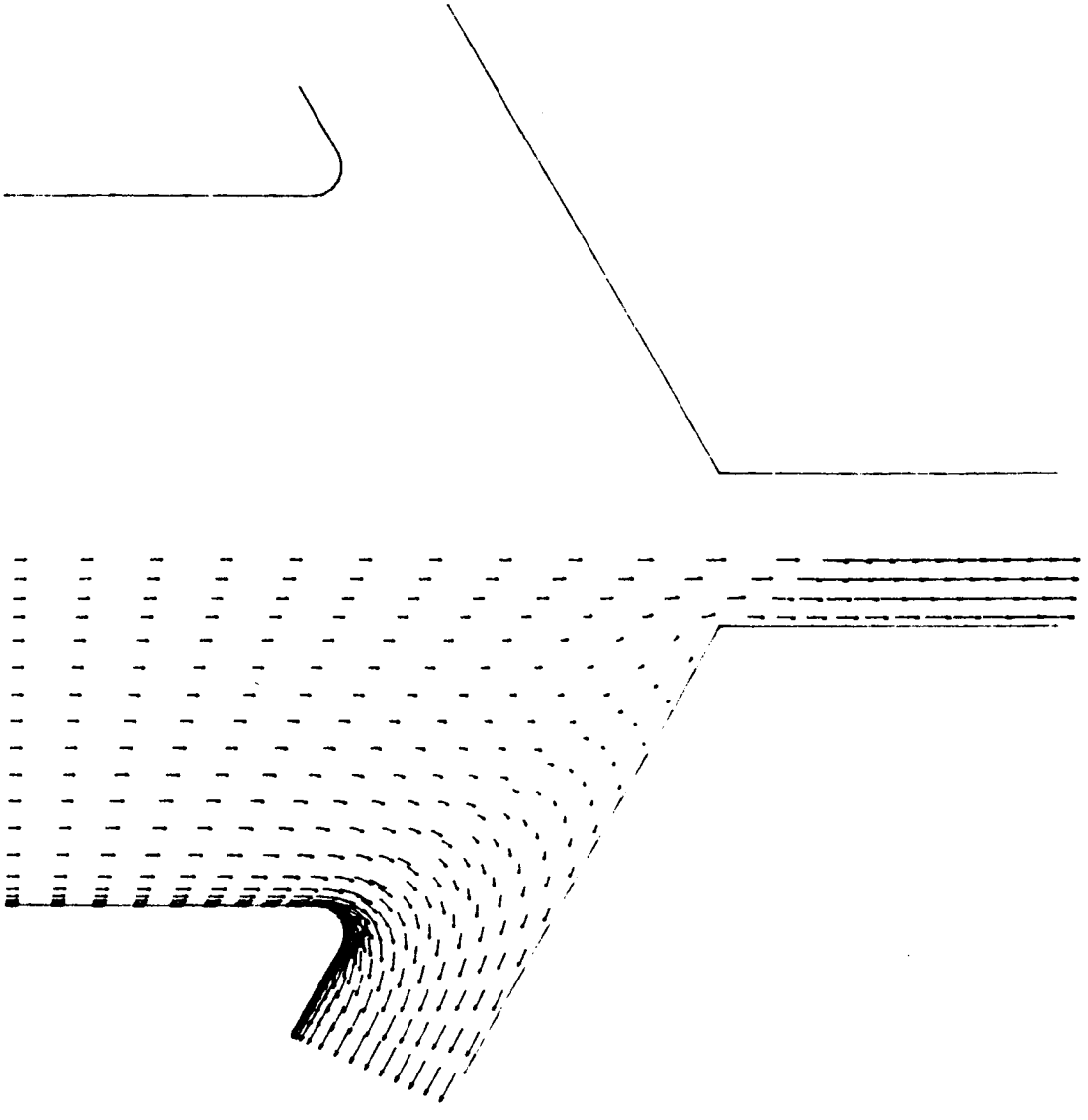

Figure 4.39 Steady State Flow Field Velocity Vectors Prior to Transition from Partial to Full Thrust Reverser Deployment.

Time = 1.44 msec.
Rear Port Width = 0.0500 ft.

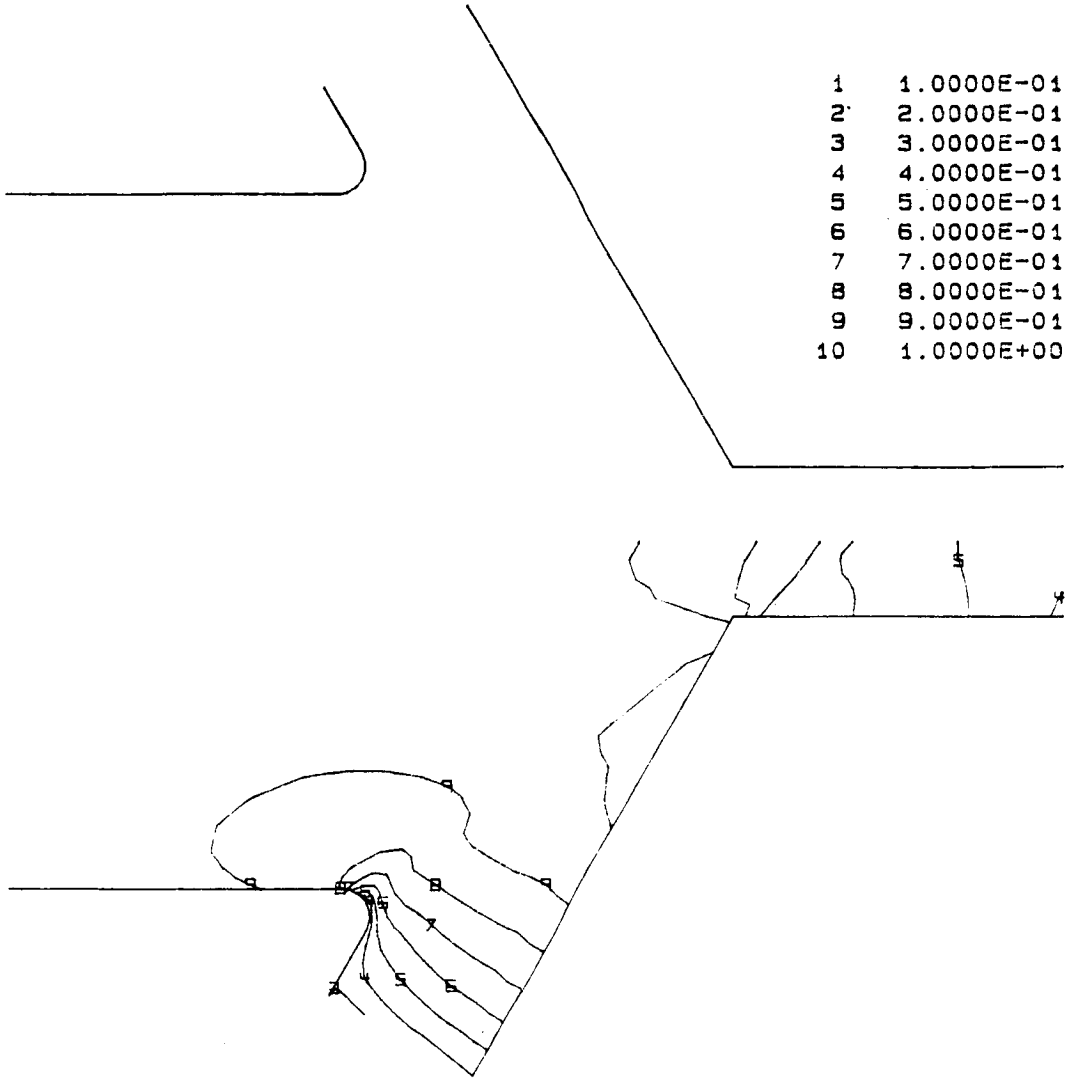

Figure 4.40 Steady State P/P_t Contours Prior to Transition from Partial to Full Thrust Reverser Deployment.

Time = 1.44 msec.
Rear Port Width = 0.0500 ft.

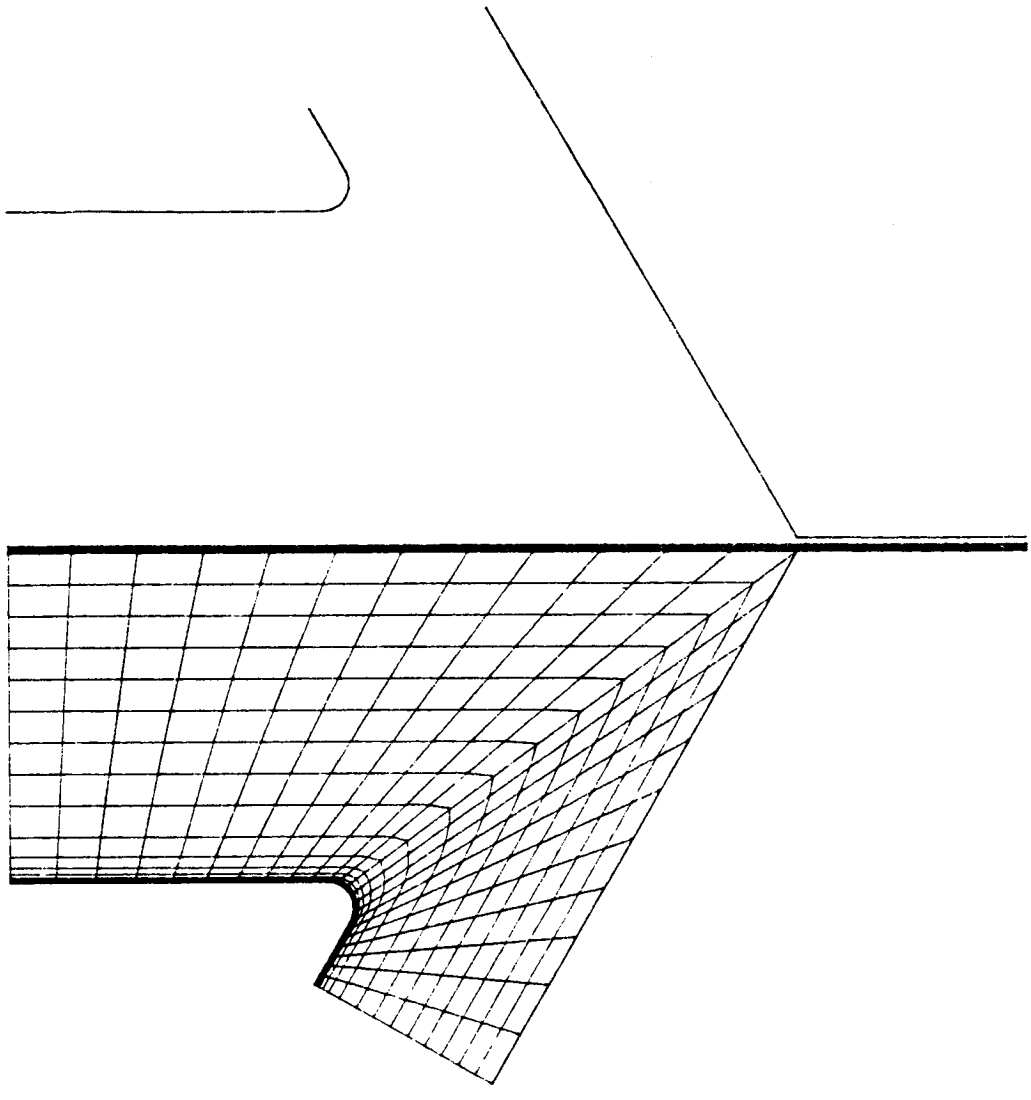

Figure 4.41 Mesh for Transient Flow Field Calculation During Transition from Partial to Full Thrust Reverser Deployment.

Time = 1.70 msec.
Rear Port Width = 0.0048 ft.

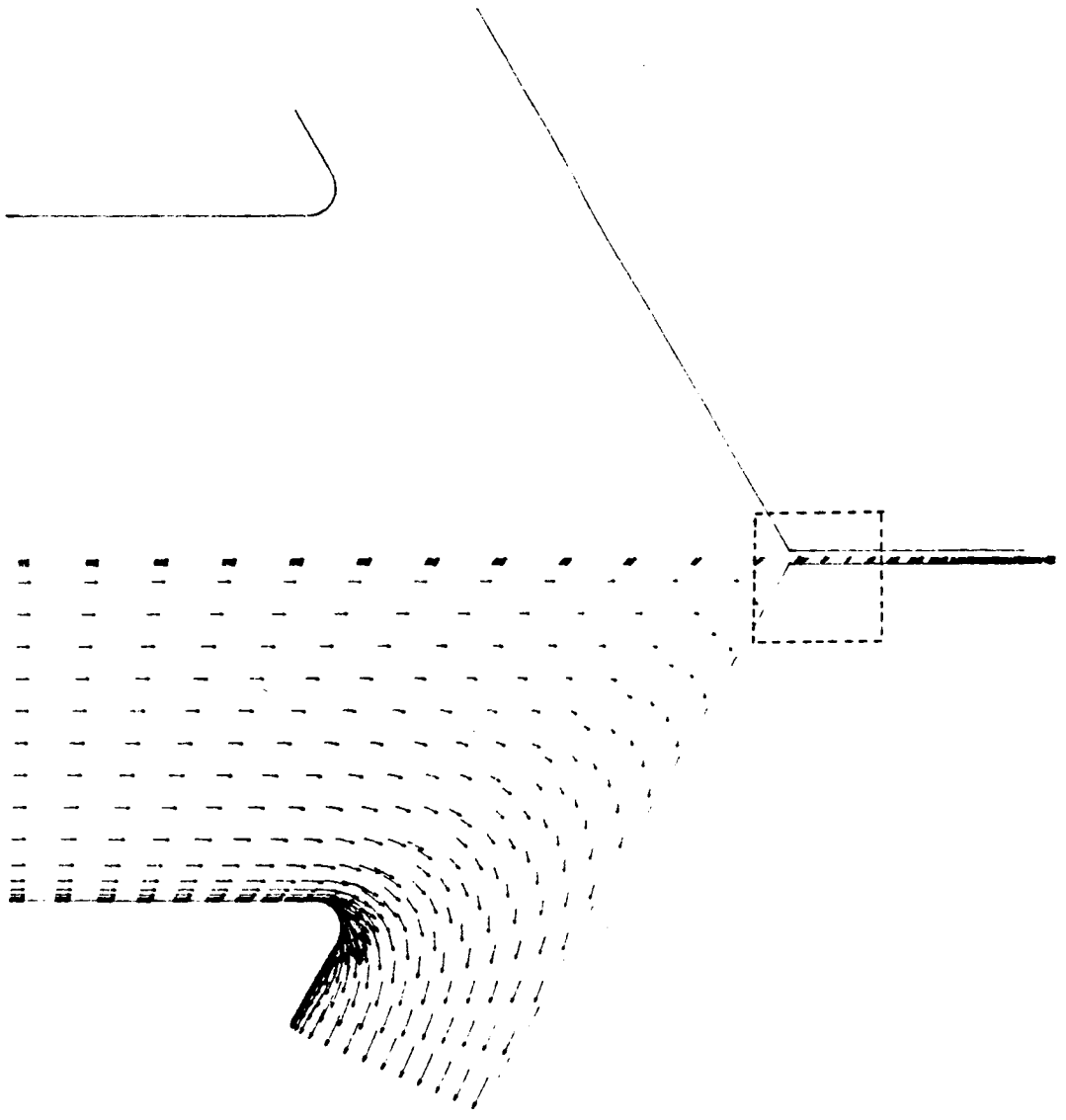

Figure 4.42a Transient Flow Field Velocity Vectors During Transition from Partial to Full Thrust Reverser Deployment

Time = 1.70 msec.
Rear Port Width = 0.0048 ft.

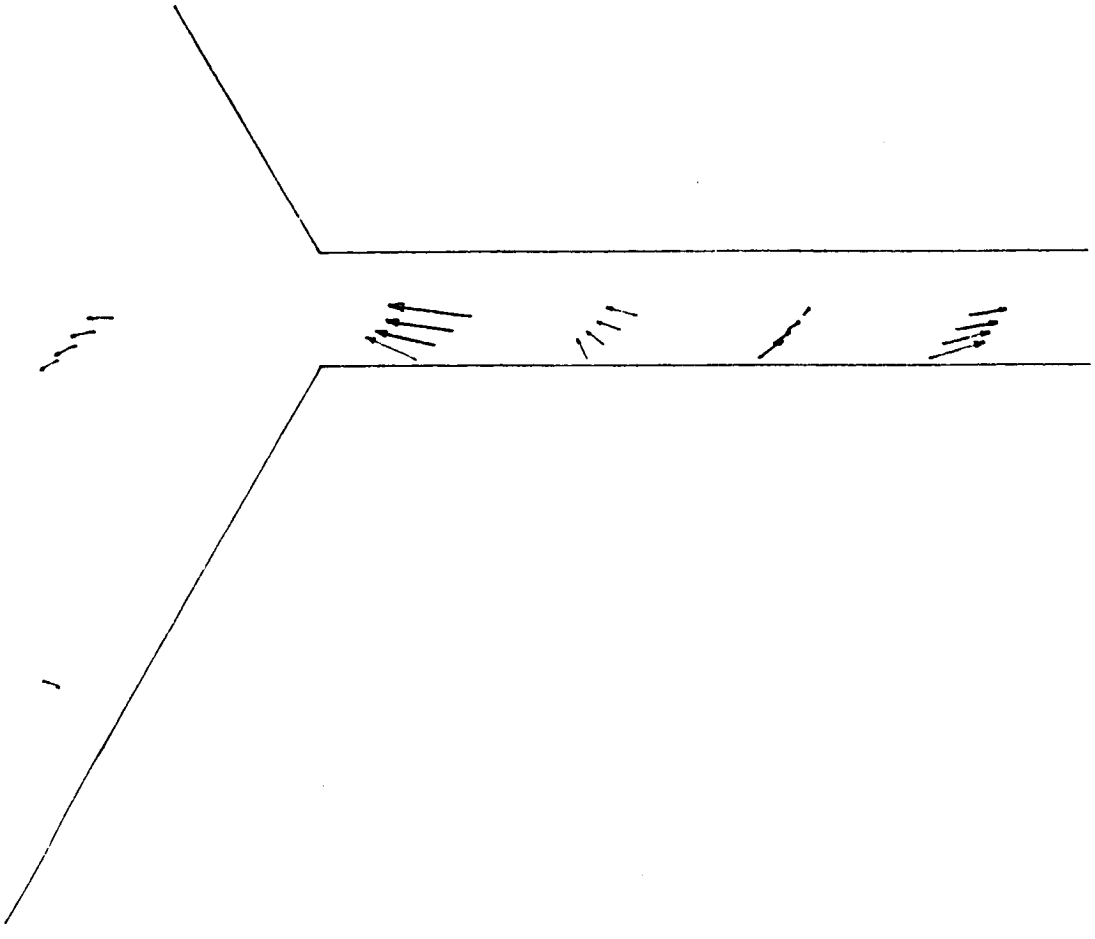

Figure 4.42b Detail of Transient Flow Field Velocity Vectors Near Entrance to Rear Port (Boxed Region on Previous Plot).

Time = 1.70 msec.
Rear Port Width = 0.0048 ft.

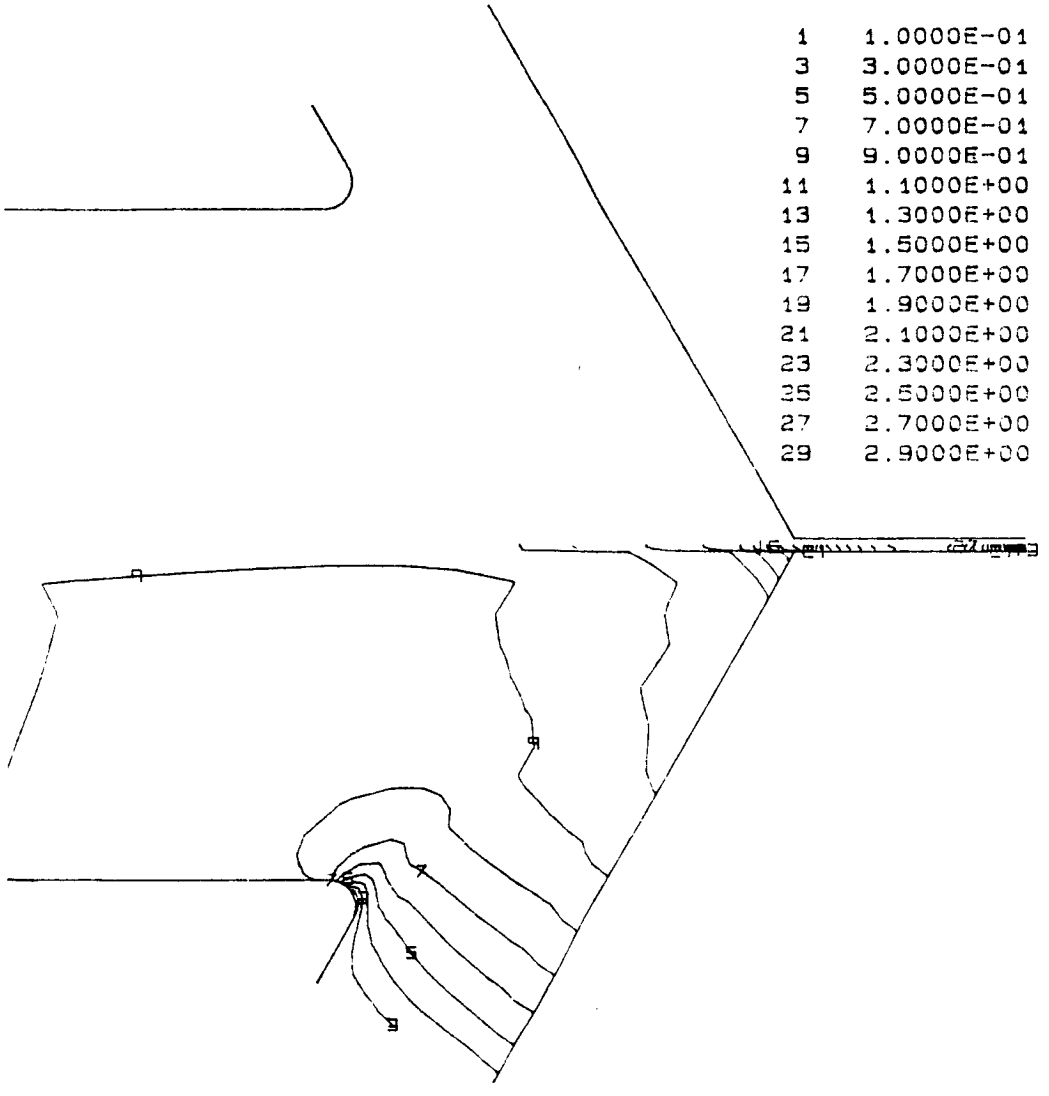

Figure 4.43 Transient Flow Field P/P_t Contours During Transition from Partial to Full Thrust Reverser Deployment.

Time = 1.70 msec.
Rear Port Width = 0.0048 ft.

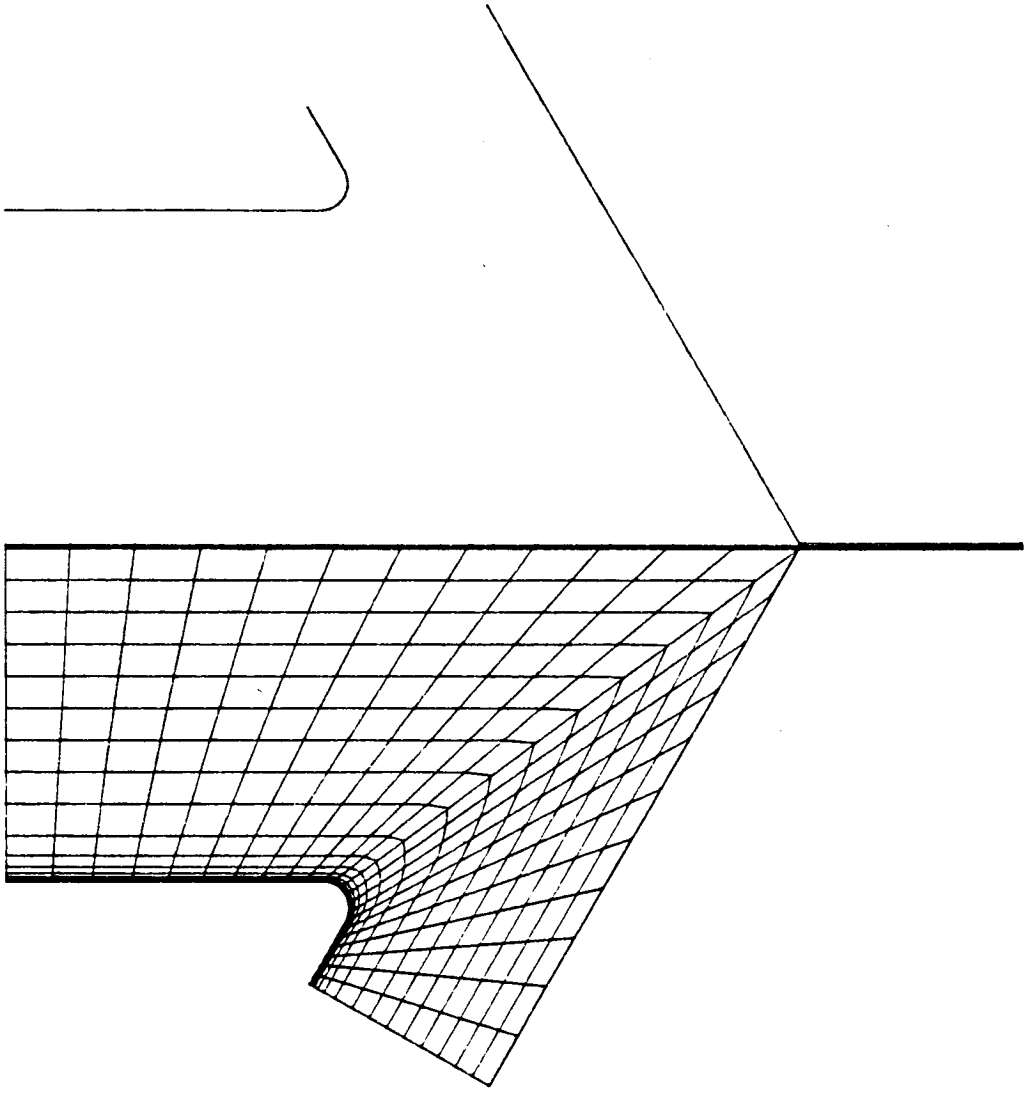

Figure 4.44 Mesh for Transient Flow Field Calculation After Transition from Partial to Full Thrust Reverser Deployment.

Time = 1.79 msec.
Rear Port Width = 0.0020 ft.

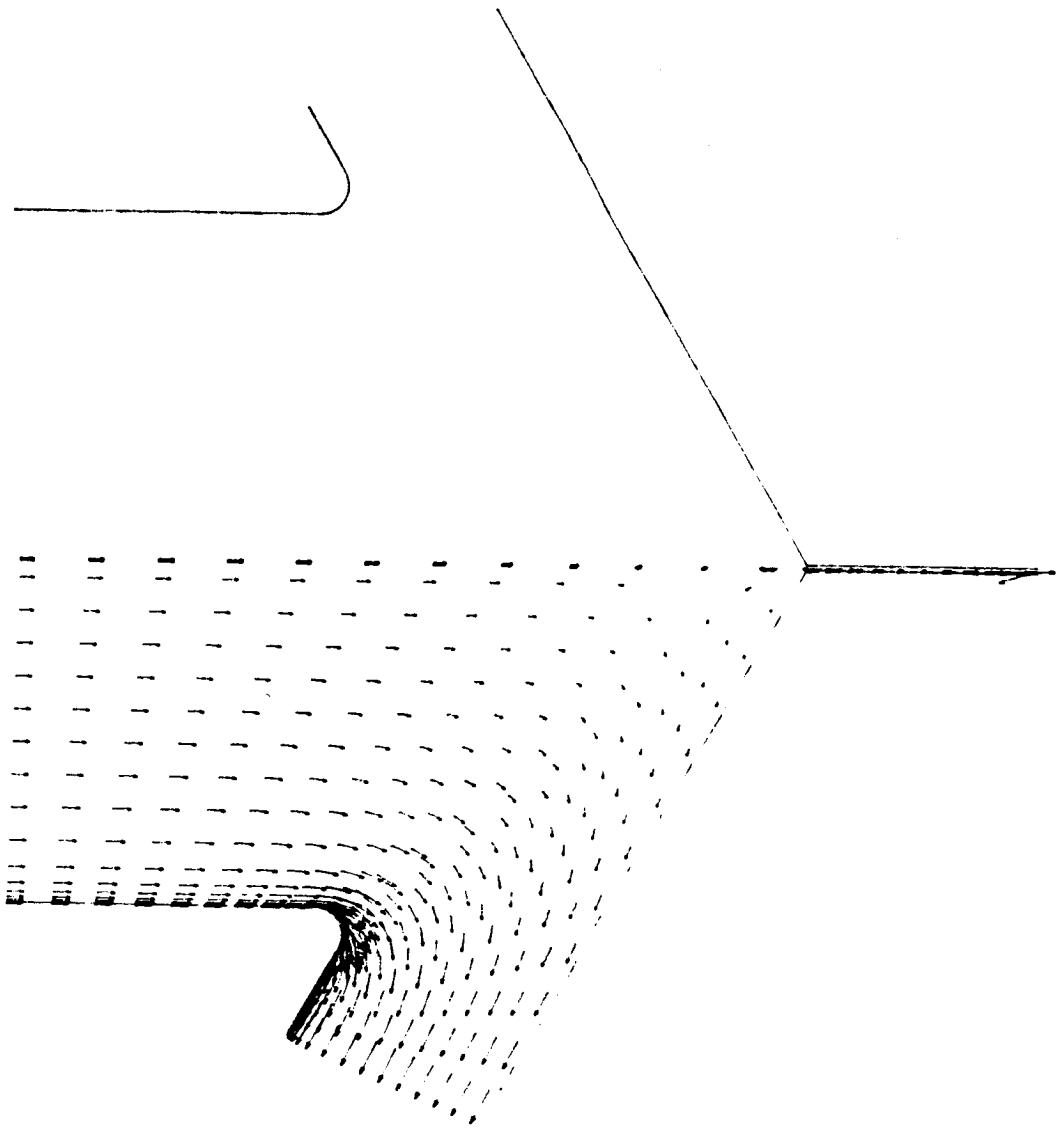

Figure 4.45 Transient Flow Field Velocity Vectors After Transition from Partial to Full Thrust Reverser Deployment.

Time = 1.79 msec.
Rear Port Width = 0.0020 ft.

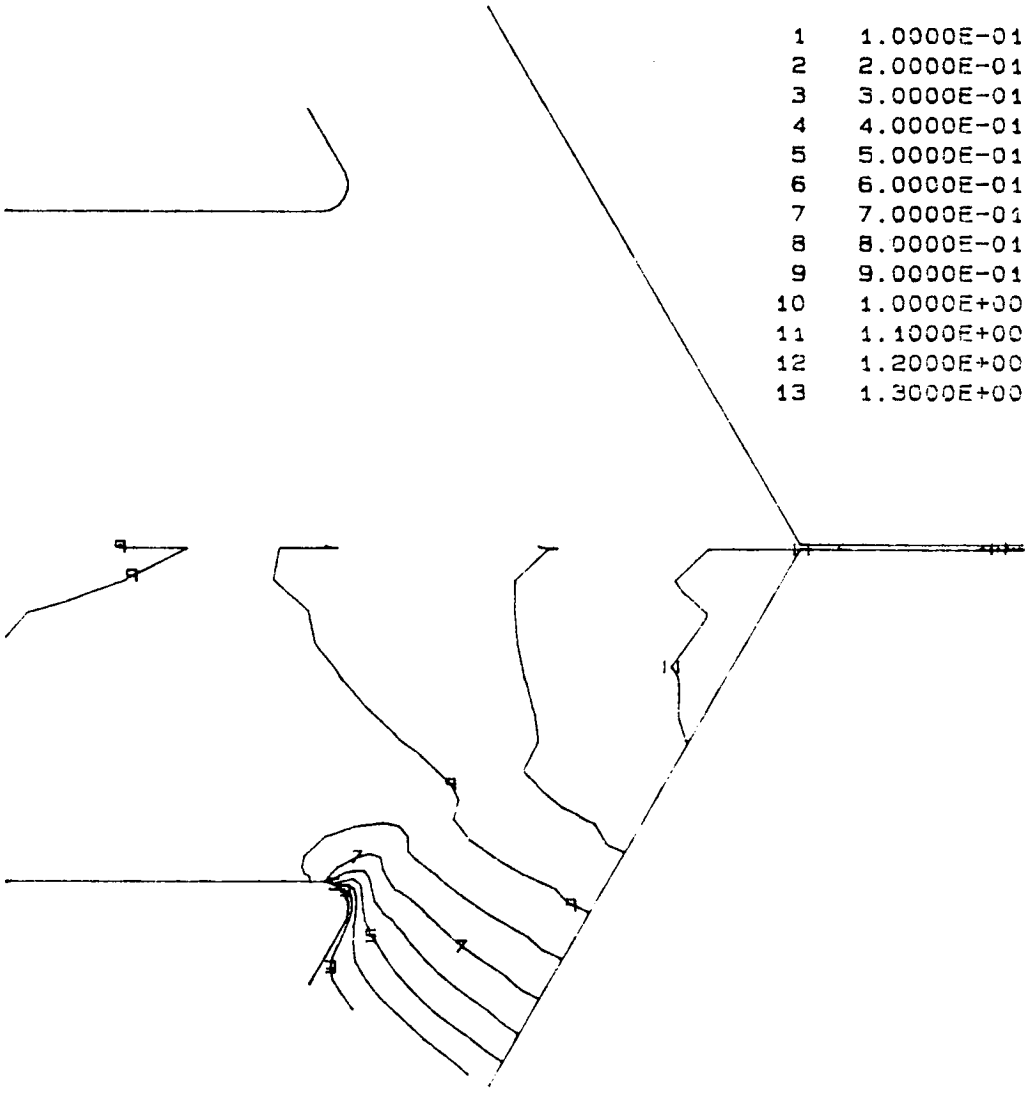

Figure 4.46 Transient Flow Field P/P_t Contours During Transition from Partial to Full Thrust Reverser Deployment.

References

1. Re, R.J. and Leavitt, L.D., "Static Internal Performance Including Thrust Vectoring and Reversing of Two-Dimensional Convergent-Divergent Nozzles," NASA TP-2253, Feb. 1984.

2. Carson, G.T., Capone, F.J. and Mason, M.L., "Aeropropulsive Characteristics of Nonaxisymmetric-Nozzle Thrust Reversers at Mach Numbers From 0 to 1.20," NASA TP-2306, May 1984.

3. Putnam, L.E. and Strong, E.G., "Internal Pressure Distributions for a Two-Dimensional Thrust-Reversing Nozzle Operating at a Free-Stream Mach Number of Zero," NASA TM-85655, Dec. 1983.

4. Cline, M.C., "VNAP2: A Computer Program for Computation of Two-Dimensional, Time-Dependent, Compressible, Turbulent Flow," Los Alamos Nat. Lab., Report LA-8872, Aug. 1981.

5. Goldberg, V.C., Gorski, J.J., and Chakravarthy, S.R., "Transonic Turbulent Flow Computations for Axisymmetric Afterbodies," AIAA-85-1639, July 1985.

6. Anderson, D.A., Tannehill, J.C., and Pletcher, R.H., Computational Fluid Dynamics and Heat Transfer, Hemisphere Publishing Corporation, Washington, 1984.

7. Baldwin, B.S. and Lomax, H., "Thin-Layer Approximation and Algebraic Model for Separated Turbulent Flows," AIAA Paper 78-257, Jan. 1978.

8. MacCormack, R.W., "Current Status of Numerical Solutions of the Navier-Stokes Equations," AIAA-85-0032, Jan. 1985.

9. MacCormack, R.W., "The Effect of Viscosity in Hypervelocity Impact Cratering," AIAA Paper 69-354, Apr.-May 1969.

10. Steger, J.L. and Warming, R.F., "Flux Vector Splitting of the Inviscid Gasdynamic Equations with Application to Finite-Difference Methods," Journal of Computational Physics, Vol. 40, 1981, pp. 263-293.

11. Beam, R.M. and Warming, R.F., "An Implicit Finite-Difference Algorithm for Hyperbolic Systems in

Conservation-Law-Form," Journal of Computational Physics, Vol. 22, Sept. 1976, pp. 87-110.

12. Briley, W.R. and McDonald, H., "Solution of the Multidimensional Compressible Navier-Stokes Equations by a Generalized Implicit Method," Journal of Computational Physics, Vol. 24, pp. 372-396.

13. Stevens, H.L., Thayer, E.B., and Fullerton, J.F., "Development of the Multifunction 2-D/C-D Nozzle," AIAA-81-1491, July 1981.

14. Warming, R.F., Beam, R.M., and Hyett, B.J., "Diagonalization and Simultaneous Symmetrization of the Gas-Dynamic Matrices," Mathematics of Computation, Vol. 29, Oct. 1975, pp. 1037-1045.

15. Burden, R.L., Faires, J.D., and Reynolds, A.C., Numerical Analysis, Prindle, Weber and Schmidt, Boston, Mass., 1978.

16. Peery, K.M. and Forester, C.K., "Numerical Simulation of Multistream Nozzle Flows," AIAA Journal, Vol. 18, No. 9, Sept. 1980, p. 1088.

APPENDIX A

Diagonalization of the Jacobians for the Inviscid Fluxes

The inviscid fluxes through a surface of arbitrary orientation are

$$\bar{P}_I \cdot \bar{S} = \begin{pmatrix} \rho q \\ \rho uq + P\, s_x \\ \rho vq + P\, s_y \\ (e+p)q \end{pmatrix} |\bar{S}| \qquad (a.1)$$

where $q = us_x + vs_y$ and s_x and s_y are the components of a unit vector normal to the surface.

The flux in equation a.1 is a homogeneous function of the conservative variables U. So

$$\bar{P}_I \cdot \bar{S} = AU$$

where A is the Jacobian of $\bar{P}_I \cdot \bar{S}$ with respect to U. Following Warming et.al., (Reference 14) the Jacobian matrix, A, may be diagonalized by a set of three similarity transformations.

$$A = T^{-1}\, R^{-1} S^{-1} \Lambda S\, R\, T\, |\bar{S}|$$

Here T is a matrix which transforms incremental changes in conservative variables to incremental changes in nonconservative variables, R rotates from the global reference frame to a local reference frame with axis normal and tangent to the surface, and S transforms from incremental changes in the nonconservative variables to incremental changes in the characteristic variables. The

diagonal matrix,

$$\Lambda = \text{diag}\,[u',\ u',\ u'+c,\ u'-c]$$

contains the eigenvalues of the Jacobian matrix, A.

The transformation matrices, and their inverses are given below.

$$T = \begin{bmatrix} 1 & 0 & 0 & 0 \\ -u/\rho & 1/\rho & 0 & 0 \\ -v/\rho & 0 & 1/\rho & 0 \\ \alpha(\gamma-1) & -u(\gamma-1) & -v(\gamma-1) & (\gamma-1) \end{bmatrix}$$

$$T^{-1} = \begin{bmatrix} 1 & 0 & 0 & 0 \\ u & \rho & 0 & 0 \\ v & 0 & \rho & 0 \\ \alpha & \rho u & \rho v & \frac{1}{(\gamma-1)} \end{bmatrix}$$

$$R = \begin{bmatrix} 1 & 0 & 0 & 0 \\ 0 & s_y & -s_x & 0 \\ 0 & s_x & s_y & 0 \\ 0 & 0 & 0 & 1 \end{bmatrix}$$

$$R^{-1} = \begin{bmatrix} 1 & 0 & 0 & 0 \\ 0 & s_y & s_x & 0 \\ 0 & -s_x & s_y & 0 \\ 0 & 0 & 0 & 1 \end{bmatrix}$$

$$S = \begin{bmatrix} 1 & 0 & 0 & -1/c^2 \\ 0 & 1 & 0 & 0 \\ 0 & 0 & \rho c & 1 \\ 0 & 0 & -\rho c & 1 \end{bmatrix}$$

$$S^{-1} = \begin{bmatrix} 1 & 0 & 1/2c^2 & 1/2c^2 \\ 0 & 1 & 0 & 0 \\ 0 & 0 & 1/2\rho c & -1/2\rho c \\ 0 & 0 & 1/2 & 1/2 \end{bmatrix}$$

In the above matrices

$$\alpha = 0.5(u^2 + v^2)$$

and c is the speed of sound.

APPENDIX B

Block Pentadiagonal Solver

The block pentadiagonal system of linear algebraic equations, Figure B.1, is solved using a block LU decomposition. The matrix is factored into two matrices, a block lower tridiagonal and a block upper triangular with identity matrices on the diagonal as shown in Figure B.2.

The LU decomposition and inversion of the L matrix is done in one sweep in the direction of reducing the j index.

1) $\hat{A}_{jl} = A_{jl}$, $\Gamma_{jl} = A_{jl}^{-1} C_{jl}$, $\Theta_{jl} = A_{jl}^{-1} E_{jl}$,

$$y_{jl} = A_{jl}^{-1} R_{jl}$$

2) $\hat{B}_{jl-1} = B_{jl-1}$, $\hat{A}_{jl-1} = A_{jl-1} - \hat{B}_{jl-1} \Gamma_{jl}$

$$\Gamma_{jl-1} = \hat{A}_{jl-1}^{-1} [C_{jl-1} - B_{jl-1} \Theta_{jl}]$$

$$\Theta_{jl-1} = \hat{A}_{jl-1}^{-1} E_{jl-1}, \quad y_{jl-1} = \hat{A}_{jl-1}^{-1} [R_{jl-1} - \hat{B}_{jl-1} y_{jl}]$$

3) $\hat{B}_j = B_j - D_j \Gamma_{j+2}$

4) $\hat{A}_j = A_j - \hat{B}_j \Gamma_{j+1} - D_j \Theta_{j+2}$

5) $\Gamma_j = \hat{A}_j^{-1} [C_j - \hat{B}_j \Theta_{j+1}]$, $\Theta_j = \hat{A}_j^{-1} E_j$,

$$y_j = \hat{A}_j^{-1} [R_j - \hat{B}_j y_{j+1} - D_j y_{j+2}]$$

6) repeat steps 3 - 5 for j = jl-3 to 1

In the above equation the vector [y] is equal to $[L]^{-1}[R]$.

All that remains is to solve the equation

$$[U] [\ U] = [y]$$

by sweeping in the direction of increasing j index.

7) $\delta U_1 = y_1$

8) $\delta U_2 = y_2 - \Gamma_2 \delta U_1$

9) $\delta U_j = y_j - \Gamma_j \delta U_{j-1} - \Theta_j \delta U_{j-2}$

10) repeat step 9 for j = 3 to jl

This algorithm requires the inversion of a 4x4 at each j location. This is done using a Crout decomposition (Reference 15).

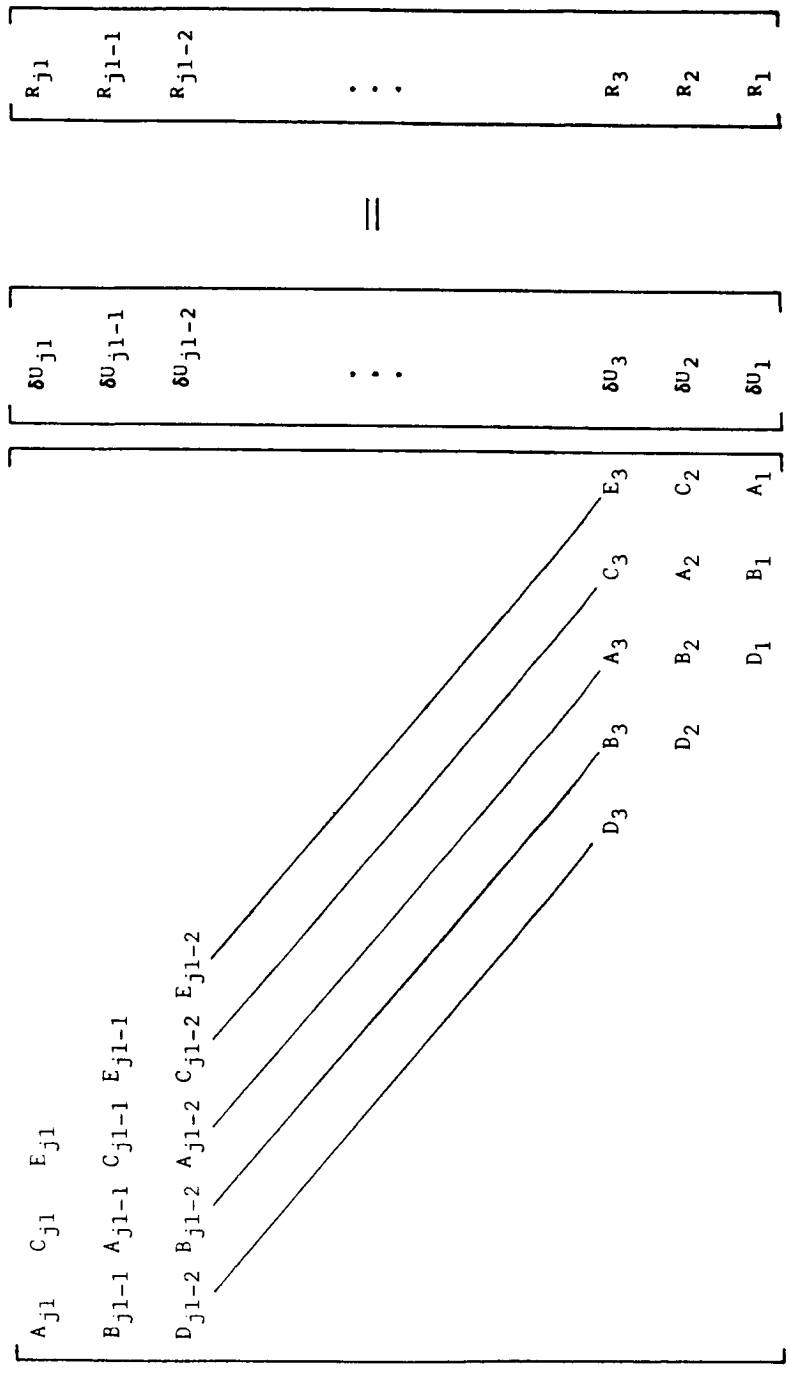

Figure B.1 Block Pentadiagonal System.

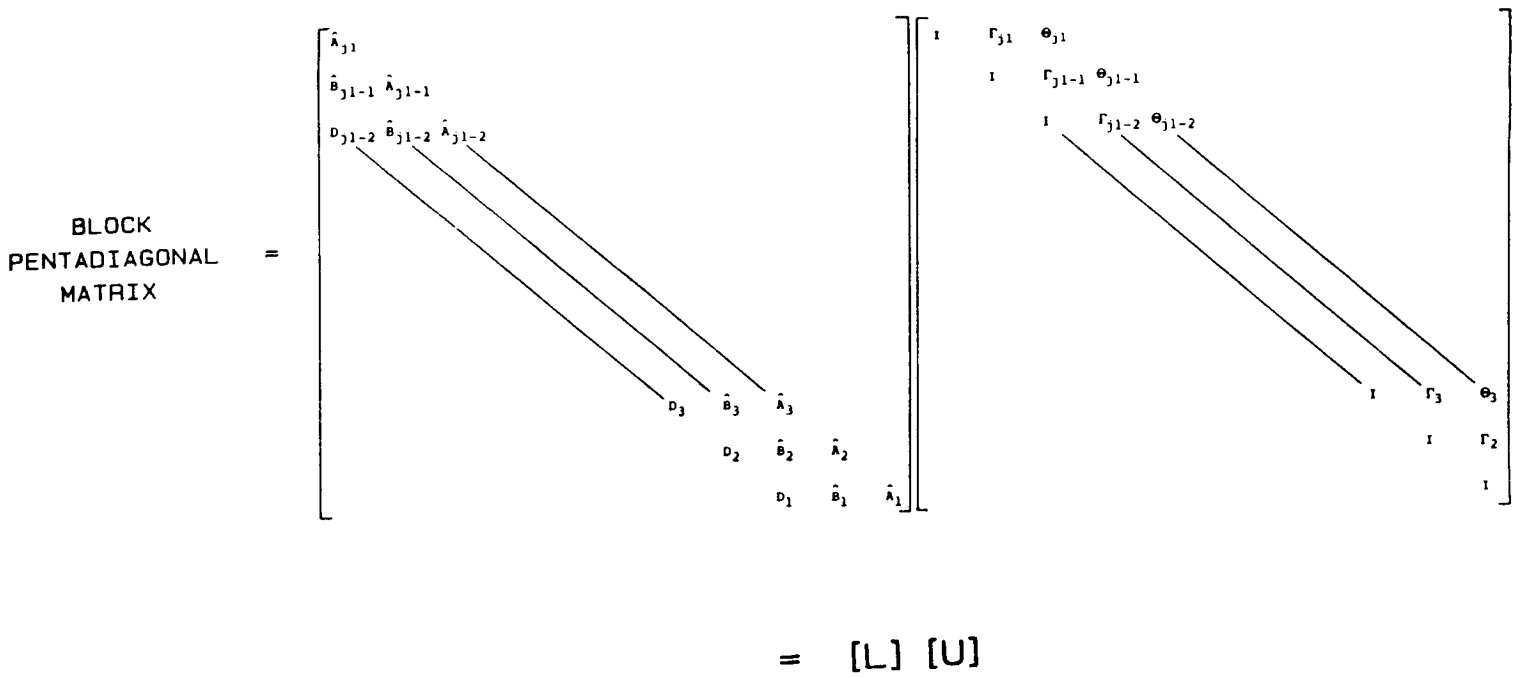

Figure B.2 LU Decomposition of the Block Pentadiagonal Matrix.

APPENDIX C

Ideal Mass Flow and Thrust

The formula for the ideal mass flow is derived from

$$\dot{m} = uA = {}^{*}a^{*}A^{*} \tag{c.1}$$

where the * indicates the value of the quantity at a sonic throat. Using the isentropic relations

$$\frac{T_t}{T} = 1 + \frac{\gamma-1}{2} M^2 \quad \text{and} \tag{c.2}$$

$$\frac{P_t}{P} = [1 + \frac{\gamma-1}{2} M^2]^{\frac{\gamma}{\gamma-1}} \tag{c.3}$$

the definition of the speed of sound

$$a^2 = \gamma RT \quad , \tag{c.4}$$

the equation of state

$$P = \rho RT \quad , \tag{c.5}$$

and the fact that the Mach number is unity at a sonic throat gives

$$\dot{m}_i = \frac{P_t}{RT_t} [\frac{2}{\gamma+1}]^{\frac{1}{\gamma-1}} [\frac{2\gamma}{\gamma+1} RT_t]^{1/2} A^* \tag{c.6}$$

The formula for the ideal thrust is obtained from

$$F = \dot{m}ue \tag{c.7}$$

where ue is the flow at the exit of a ideally expanded nozzle ($p_e = p_\infty$). The formula for u_e is obtained from

$$u_e^2 = a_e^2 M_e^2 \tag{c.8}$$

and equations c.2 - c.5. The result is

$$u_e = \{\frac{2\gamma}{\gamma-1}RT_t[1 - (\frac{p_e}{p_t})^{\frac{\gamma-1}{\gamma}}]\}^{1/2} \qquad (c.9)$$

Before substituting u_e from equation c.9 into equation c.7 it should be decided which mass flow, $\dot{m}$, to use. In the experimental results of Re and leavitt (Reference 1) and Carson, et.al., (Reference 2) the measured mass flow is used in the calculation of the ideal thrust. To be consistent, we will also use the measured mass flow when making comparisons with experiment.

$$F_i = \dot{m} \{\frac{2}{\gamma-1} RT_t [1 - (\frac{p_e}{p_t})^{\frac{\gamma-1}{\gamma}}]\}^{1/2} \qquad (c.10)$$

Standard Bibliographic Page

1. Report No.	2. Government Accession No.	3. Recipient's Catalog No.
NASA CR-4026		

4. Title and Subtitle	5. Report Date
Implicit Time-Marching Solution of the Navier-Stokes Equations for Thrust Reversing and Thrust Vectoring Nozzle Flows	November 1986
	6. Performing Organization Code
7. Author(s)	8. Performing Organization Report No.
Scott T. Imlay	
9. Performing Organization Name and Address	10. Work Unit No.
University of Washington Dept. of Aeronautics and Astronautics Seattle, WA 98195	11. Contract or Grant No. NAS1-17170
12. Sponsoring Agency Name and Address	13. Type of Report and Period Covered
National Aeronautics and Space Administration Washington, DC 20546	Contractor Report
	14. Sponsoring Agency Code 505-62-91-01

15. Supplementary Notes

NASA Langley Technical Monitors: Richard G. Wilmoth and Lawrence E. Putnam

16. Abstract

An implicit finite volume method is investigated for the solution of the compressible Navier-Stokes equations for flows within thrust reversing and thrust vectoring nozzles. Thrust reversing nozzles typically have sharp corners, and the rapid expansion and large turning angles near these corners are shown to cause unacceptable time step restrictions when conventional approximate factorization methods are used. In this investigation these limitations are overcome by using second-order upwind differencing and line Gauss-Siedel relaxation. This method is implemented with a zonal mesh so that flows through complex nozzle geometries may be efficiently calculated.

Results are presented for five nozzle configurations including two with time varying geometries. Three cases are compared with available experimental data and the results are generally acceptable.

17. Key Words (Suggested by Authors(s))	18. Distribution Statement
Nozzle Flows Thrust Reversing Thrust Vectoring Navier-Stokes Solutions Implicit Time-Marching Finite-Volume Methods	Unclassified - Unlimited Subject Category 34

19. Security Classif.(of this report)	20. Security Classif.(of this page)	21. No. of Pages	22. Price
Unclassified	Unclassified	192	A09

For sale by the National Technical Information Service, Springfield, Virginia 22161